Vehicle Lateral Driving Stability Regions: Estimation, Analysis, and Control

by

Yiwen Huang

A Dissertation Presented in Partial Fulfillment
of the Requirements for the Degree
Doctor of Philosophy

Approved April 2021 by the
Graduate Supervisory Committee:

Yan Chen, Chair
Hyunglae Lee
Yi Ren
Sze Zheng Yong
Wenlong Zhang

ARIZONA STATE UNIVERSITY

May 2021

ABSTRACT

In the development of autonomous ground vehicles (AGVs), how to guarantee vehicle lateral stability is one of the most critical aspects. Based on nonlinear vehicle lateral and tire dynamics, new driving requirements of AGVs demand further studies and analyses of vehicle lateral stability control strategies. To achieve comprehensive analyses and stability-guaranteed vehicle lateral driving control, this dissertation presents three main contributions.

First, a new method is proposed to estimate and analyze vehicle lateral driving stability regions, which provide a direct and intuitive demonstration for stability control of AGVs. Based on a four-wheel vehicle model and a nonlinear 2D analytical LuGre tire model, a local linearization method is applied to estimate vehicle lateral driving stability regions by analyzing vehicle local stability at each operation point on a phase plane. The obtained stability regions are conservative because both vehicle and tire stability are simultaneously considered. Such a conservative feature is specifically important for characterizing the stability properties of AGVs.

Second, to analyze vehicle stability, two novel features of the estimated vehicle lateral driving stability regions are studied. First, a shifting vector is formulated to explicitly describe the shifting feature of the lateral stability regions with respect to the vehicle steering angles. Second, dynamic margins of the stability regions are formulated and applied to avoid the penetration of vehicle state trajectory with respect to the region boundaries. With these two features, the shiftable stability regions are feasible for real-time stability analysis.

Third, to keep the vehicle states (lateral velocity and yaw rate) always stay in the shiftable stability regions, different control methods are developed and evaluated. Based on different vehicle control configurations, two dynamic sliding mode controllers (SMC) are designed. To better control vehicle stability without suffering chattering issues in SMC, a non-overshooting model predictive control is proposed and applied. To further save computational burden for real-time implementation, time-varying control-dependent invariant sets and time-varying control-dependent barrier functions are proposed and adopted in a stability-guaranteed vehicle control problem.

Finally, to validate the correctness and effectiveness of the proposed theories, definitions, and control methods, illustrative simulations and experimental results are presented and discussed.

ACKNOWLEDGMENTS

Graduating in 2021 will definitely be an unforgettable experience in my entire life. In this year, we appreciate, we cherish, and we learn how to love. Upon finishing my five-year of doctoral study at Arizona State University, I want to take a moment to express my sincere gratitude for all the supports and encouragement I have received during this amazing journey.

First and foremost, I would like to thank my esteemed supervisor and mentor – Dr. Yan Chen for his invaluable supervision, support, and tutelage during the entire course of my Ph.D. degree. When a younger me first stepped into the research world of vehicle dynamics, Dr. Chen's enthusiasm and profound knowledge greatly encouraged and inspired me to explore and solve interesting and cutting-edge problems. On my way to becoming an independent researcher, Dr. Chen did not always show his full academic support but also taught me the more important things - logical thinking and rigorous research culture. More than just the research itself, Dr. Chen's outstanding working attitude has always been my pursuit and spiritual model. Looking back, I feel so lucky and grateful of joining the Dynamic Systems and Control Laboratory (DSCL) and having Dr. Chen as my doctoral supervisor – thank you!

My gratitude extends to my other committee members, Dr. Hyunglae Lee, Dr. Yi Ren, Dr. Sze Zheng Yong, and Dr. Wenlong Zhang, for their guidance, continuous support, and patience at every stage of my Ph.D. study. Taking their courses, discussing and working with them as a teaching assistant have been the most precious experience I have ever had in ASU. Their inspiration and guidance will always be the treasure in my future career.

I would like to thank all my friends, lab mates in DSCL, colleagues, SEMTE and TPS staff, and other research teams at Arizona State University. Particularly, I would like to thank Dr. Fengchen Wang, Yue Zhao, Hongru Xu, Ao Li, Dr. Yue Shi, Dr. Minghui Ren, and Chuan Chang, for their support and valuable suggestions. It has been a great time working with them to achieve our dreams. I also want to particularly thank my academic advisor, Christine Quintero, for her great support of my plan of graduate studies.

Last but not least, I would also like to thank my family, to whom this dissertation is dedicated. My father, Yunsheng Huang, and my mother, Yuhua Liu have been giving me all their love and care, which greatly helped me to be confident and strong during the hardest times. I also sincerely appreciate their full support and respect for my choices at each important stage in my life.

TABLE OF CONTENTS

Page

CHAPTER Page

CHAPTER Page

CHAPTER Page

LIST OF TABLES

LIST OF FIGURES

Figure Page

Figure Page

Figure Page

LIST OF SYMBOLS / NOMENCLATURE

α	Tire slip angle
β	Vehicle sideslip angle
λ	Tire slip ratio
δ_f	Front wheel steering angle
δ_r	Rear wheel steering angle
δ_{fc}	Front corrective active steering angle
δ_{rc}	Rear corrective active steering angle
μ	Tire-road friction coefficient
F_x	Longitudinal tire friction force
F_y	Lateral tire friction force
F_{yAFS}	Tire lateral forces generated by AFS
F_{yARS}	Tire lateral forces generated by ARS
F_n	Tire vertical load
I_z	Yaw moment of inertia
K_{us}	Understeer coefficient
L	Wheelbase
M_{DYC}	Yaw moment generated by DYC
P_{motor}	Power of in-wheel motor
P_{steer}	Power of steering motor
T_s	Sampling instant

V_x	Vehicle longitudinal velocity
V_y	Vehicle lateral velocity
a_y	Vehicle lateral acceleration
h_{CG}	Height of vehicle center of gravity
l_f	Front wheelbase
l_r	Rear wheelbase
l_s	Wheel track
m_v	Vehicle mass
r	Vehicle yaw rate

CHAPTER 1

INTRODUCTION

1.1. Background

In the past decades, with the development of passive/active safety equipment and advanced driver-assistance systems (ADAS), vehicle transportations become more convenient and safer [1]. To the great extent of improving the driving experience and enhancing driving safety, autonomous vehicles (AVs), as a revolution of the transportation system, were proposed and have obtained rapid development and great achievements in recent years [1]-[6]. However, to further enhance vehicle safety and promote the public adoption of AVs, many critical issues still need to be properly addressed [1][2].

Generally, vehicle safety does not only refer to the safety of drivers and passengers, but also the surrounding vehicles, pedestrians, bicycles, and infrastructures [7]. To enhance the driving safety of AVs, in addition to the advanced sensing, data fusion, and artificial intelligence (AI), the controls of fundamental vehicle dynamics are also critical [7]. In most of the driving scenarios, the advanced AI algorithms embedded in the high-level vehicle control systems may help to safely decide and control the vehicle's motion. However, in some emergent scenarios, the vehicle safety may not be well-controlled due to the imperfection in the recognition and cognition of AI, or the reaction time delay caused by the high computational burden [8]. To tackle such vehicle safety-related challenges, a robust and computation-feasible low-level vehicle dynamics control system would be an effective and promising approach. Cooperating with the high-level autonomous driving

strategies, such a low-level vehicle dynamic control system plays an important role to guarantee the driving safety of the vehicles, especially in emergent situations.

To develop a vehicle safety-guaranteed control system, the essential factors that affect safety should be first clarified. Normally, vehicle safety requires the vehicle dynamic/handling stability, road/lane boundaries, traffic rules, pedestrians, and some other uncertainties all need to be thoughtfully considered and handled. Among all these factors, the vehicle dynamic/handling stability is the most fundamental one because it directly determines the vehicle motion with respect to other on-road objects (e.g., collision avoidance). Moreover, as the level of driving automation (SAE J3016 [5]) increases, the control responsibilities of drivers gradually shift to the autonomous driving systems (ADS) [1]. Thus, from the liability and responsibility point of view, how the ADS can guarantee the vehicle dynamic/handling stability becomes a critical topic. Therefore, a well-developed real-time vehicle stability analysis and control system that guarantees vehicle stability becomes necessary for AGVs and has huge potentials for a variety of automotive applications.

1.2. Literature Review [1]

In the studies of vehicle stability analysis and control, vehicle lateral dynamics, due to its complexity and nonlinear behaviors caused by the nonlinear and coupled tire forces, is one of the most challenging topics. To design a proper vehicle lateral stability control, a

[1] Part of the reviews in this section are with permission of Copyright © 2019, 2021 IEEE and Copyright © 2021 ASME, to be reprinted from [Huang and Chen, *IEEE Transactions on Vehicular Technology*, 2021], [Huang, Liang, and Chen, *ASME Journal of Dynamic System, Measurement, and control*, 2021], [Huang and Chen, in *Proceedings of American Control Conference*, 2019], and [Huang, Yong, and Chen, *IEEE Transactions on Intelligent Vehicles*, 2021].

comprehensive understanding of vehicle lateral stability is essential and should be first conducted. Among a variety of vehicle dynamic stability analysis methods, the estimation of vehicle lateral stability region provides an effective and intuitive illustration of the vehicle lateral dynamic characteristics and can be particularly informative in vehicle stability control designs. The vehicle lateral stability regions are typically defined on a phase plane that may consist of different vehicle state combinations, such as vehicle lateral velocity (or sideslip angle) and yaw rate. In the past decades, a great number of vehicle lateral stability region estimation methods have been proposed. Depending on the adopted methods, the estimated vehicle lateral stability regions can be categorized into the following three groups.

First, the phase portrait method, as the most straightforward approach [9]-[12], was widely applied. Inagaki *et al.* [9] analyzed the vehicle lateral stability and defined a stable region by geometrically checking if the state trajectory returned to the system equilibria. Ono *et al.* [10] studied the bifurcation phenomena of the vehicle lateral dynamics for robust front wheel steering control. Shen *et al.* [11] introduced a novel joint-point locus approach to analyze the bifurcation phenomena for the stability of a four-wheel steering vehicle and discussed the critical impacts of the front and rear wheel steering angles. Based on the phase portrait trajectory reversing technique, Ko *et al.* [12] proposed a topology algorithm to estimate the vehicle lateral stability region. Rossa *et al.* [13] studied the bifurcation of a car with and without a driver model using the phase portrait method. Vehicle stability regions were also estimated by combining the phase portrait method with the handling diagram to generate new stability regions and the corresponding control laws [14]-[17].

Second, Lyapunov theory was also a popular method to explore the nonlinear vehicle lateral stability problem [18]-[21]. Johnson and Huston [18] first used the Lyapunov second method to study the vehicle lateral stability problem and obtained an estimated stability region on $V_y - r$ plane. Samsundar and Huston [19] estimated the vehicle lateral stability regions using three different methods, namely the Lyapunov second method, the tangency points method, and the trajectory reversal. The obtained stability regions showed certain consistency and similarity with each other. Yin *et al.* [20] estimated vehicle lateral stability regions by applying the same Lyapunov second method with discussions on the influence of steering angle, tire-road friction coefficient, and vehicle longitudinal velocity. Sadri and Wu [21] proposed a novel lateral stability region estimation method based on the calculation of Lyapunov exponents.

Third, other methods, except the phase portrait and Lyapunov theory, can be generally grouped as one category [22]. Hashemi *et al.* [23] proposed a general lateral dynamic model to investigate vehicle lateral stability, which considered linear and nonlinear tire behaviors by applying pure and combined-slip assumptions. Yi *et al.* [24] used the rear tire slip angle, instead of vehicle sideslip angle, with vehicle yaw rate to study the stability and agility of the vehicle and obtained the estimated vehicle stability region. Hoffman *et al.* [25] applied the Milliken Moment Method (MMM) and dynamic simulation to evaluate vehicle stability and controllability. Inspired by the "g-g" diagram [26], Daher *et al.* [27] defined a vehicle stability region on the "g-g" plane and designed the corresponding stability control algorithm.

From the theoretical perspective, the aforementioned studies provided insights into the vehicle lateral dynamic stability analysis. However, the theoretical vehicle lateral stability analysis does not always effectively reflect the actual factors related to vehicle stability due to the lack of analysis from practical perspectives, such as the handling characteristic. Therefore, to get a more accurate description of vehicle safety with a particular focus on vehicle dynamic/handling stability analysis, a novel estimation method is needed.

Based on the estimated vehicle lateral stability regions, the corresponding vehicle lateral dynamics controls were also designed and presented in the literature. Inagaki *et al.* [9] proposed a method to control the vehicle lateral motion based on the stability region defined on the phase plane of vehicle sideslip angle and its derivative ($\beta - \dot{\beta}$). Bobier and Gerdes [17] introduced an envelope control strategy using a sliding mode stability controller to assist a driver to keep vehicle states within a safe region in planar state space. Based on the same stability region in [9], Mousavinejad *et al.* [30] developed a terminal sliding mode control algorithm, which integrated both active front steering (AFS) and direct yaw moment control (DYC) to improve vehicle handling and stability under critical lateral motions. He *et al.* [31] proposed an integrated control for vehicle active steering, driveline, and braking. Jin *et al.* [32] proposed a gain-scheduled vehicle handling stability control via an integration of AFS and active suspension systems.

In addition to the control method using AFS and DYC, the advances of steer-by-wire and distributed driving technologies also make the application of active rear wheel steering (ARS) technology more feasible and affordable [37]. The main research topics about ARS include decreasing phase lag in vehicle lateral and yaw motion responses, developing

robust or adaptive control structure, achieving better vehicle maneuverability and lateral stability, and improving reference tracking performance on vehicle states [38]-[47]. Among all these topics in the past few decades, the most two compelling research objectives are to pursue better vehicle tracking performance and improve vehicle stability. To achieve better tracking performance, Horiuchi *et al.* [40] proposed an active front and rear wheel steering control system, which achieved accurate tracking performance of desired lateral acceleration and yaw rate. Hiraoka *et al*. [41] proposed an automatic path-tracking controller, which allowed front and rear wheel steering angle to be decoupled. Yoon *et al.* [42] presented a model predictive approach of unmanned ground vehicles using ARS to solve an optimal tracking problem while avoiding collision with obstacles. To improve vehicle stability using ARS, many studies have also been presented. Mammar and Koenig [43] discussed the vehicle lateral stability problem through the phase portrait method and designed an active steering method based on the combination of feedforward and feedback controllers to enhance the overall vehicle stability. Yu and Moskwa [44] introduced both 4WS and independent wheel torque control to enhance vehicle stability. Abe [45] pointed out that when nonlinear tire and vehicle system dynamics were involved, DYC would inevitably improve the handling and stability performance compared with ARS control. Aiming at the same objective, Nagai *et al*. [46] presented an integrated control of ARS and DYC using braking force to compensate for the lack of capability when the tire was working in the saturated region. Instead of applying a constant or continuous control signal, Zhang *et al.* [47] applied a pulsed active steering system to improve the effectiveness of vehicle yaw stability control.

Although various stability region-based control methods were studied and evaluated, many issues remain and need to be properly addressed. One critical issue is that the vehicle stability controllers were activated only when vehicle states were out of the defined stability boundaries [9][10][14][17][27]-[36]. Thus, even the designed control could successfully take vehicle states back to the defined regions, the vehicle has already experienced an unstable or undesired period before reentering the stability regions. Therefore, to ensure that a vehicle always operates stably, a control method that guarantees the vehicle states are always within the stability region is needed. To achieve guaranteed vehicle stability control, various methods were applied, where, two of them, namely the non-overshooting control designs and the control barrier function (CBF), are reviewed in the following two paragraphs respectively.

Theoretically, non-overshooting control designs can be categorized into two groups depending on the linearity of the system. For linear systems, Phillips and Seborg [48] presented a necessary and sufficient condition in state-space form, which guaranteed no overshoot of states or outputs. If the system matrix A was essentially positive, no system overshoot for a specified input was also proved. Moore and Bhattacharyya [49] presented an approach to select the best possible zero locations to minimize overshoot. Considering both real and complex poles, Lin and Fang [50] described the necessary and sufficient conditions of the non-overshooting step response for a third-order single-input and single-output (SISO) linear system. Bement and Jayasuriya [51] proposed two methods to obtain continuous time, non-overshooting tracking controllers for linear SISO systems. Schmid and Ntogramatzidis [52] proposed a method to design a linear time-invariant state feedback

controller, which could achieve non-overshooting and arbitrarily small rise time for a step response. For nonlinear systems, Krstic and Bement [53] presented a non-overshooting control design for SISO strict-feedback nonlinear systems using a modified backstepping method. The overshooting amount could be made arbitrarily small by appropriately selecting control gains. Zhu and Zhao [54] proposed a controller design using the feedback linearization and global coordinate transformation to achieve non-overshooting output tracking of feedback linearizable SISO systems. This method complemented the work in [53] since the strict feedback form of the system was not required. Gonzalez *et al.* [55] proposed a chattering free sliding mode control combined with high accuracy and fast non-overshooting response at a steady state.

In addition to the non-overshooting method, the guaranteed vehicle stability problem can also be described by the concept of controlled invariant sets [58] and CBF [62][63]. For vehicle dynamics with only feedforward or driver control, the vehicle states may not always stay in the stability region. Therefore, to make the stability region an invariant set, a proper control design is needed. Inspired by control Lyapunov functions (CLF) in [59], the control barrier functions (CBF) based on controlled invariant sets were proposed to define the admissible initial conditions and derive feedback control laws that ensure system safety [62][63]. CBFs can be categorized into two groups, the reciprocal control barrier function (RCBF) and the zeroing control barrier function (ZCBF) [63]. For RCBF [64]-[68], a commonly used function is in a logarithm form. One noteworthy feature of RCBF is that the function value goes to infinity as the states approach the set boundary. Such unboundedness may introduce two issues: 1) the unbounded function value may lead to

unbounded control efforts, which are not desired or feasible; 2) the infinity function value at the boundary results in the discontinuity of the function, which makes boundary-crossing not possible and thus the initial condition cannot be selected from outside of the set. However, for ZCBF [63][69]-[75], since the function value becomes zero (bounded) as the states approach the set boundary, the issues of RCBF do not exist. Generally, system safety can be guaranteed when the designed control satisfies the derived conditions from either RCBF or ZCBF. CBFs were also applied with CLFs to achieve the system output tracking requirements with guaranteed safety [63][69]. For a safety control problem with multiple constraints, multiple CBFs could be combined or shared by a control Lyapunov-barrier function (CLBF) [69] or a quadratic programming (QP) method [74]. Moreover, other aspects of CBF have also been studied, such as the robustness of CBFs [75] and time-varying CBFs for time-varying invariant sets [76].

However, it is notable that the aforementioned control methods are not applicable to solve the region-based guaranteed vehicle stability control problem. First, the non-overshooting control methods are only designed for linear or feedback linearizable systems, thus do not apply to the nonlinear vehicle dynamics. Second, the CBF methods in the literature are also not applicable since the estimated vehicle stability regions are control-dependent.

1.3. Contributions and Outlines

While many studies and achievements have been made in the field of vehicle stability analysis and control, the aforementioned concerns and issues remain and need to be further investigated. Focusing on the estimation of vehicle lateral stability regions and the vehicle

dynamic/handling stability-guaranteed control, this dissertation presents three main contributions.

First, a local linearization method is applied to evaluate the stability of every operational point on the $V_y - r$ phase plane, where the derived stability conditions fundamentally imply the vehicle's handling stability. By depicting the outline of all the stable operation points, the estimated vehicle lateral stability region guarantees both vehicle stability (locally in the sense of Lyapunov) and tire stability (based on the nonlinear LuGre tire models). Besides, the stability region is analyzed with respect to various impacts, such as the vehicle lateral load transfer, longitudinal velocity, tire-road friction coefficient, and steering angle, providing the potential of the estimated stability region for vehicle stability controls.

Second, based on the estimated stability region, an effective and robust region-based stability analysis method is proposed with the adoption of a projection method, where an explicit shifting vector and the dynamic margin of the stability region are integrated. Based on the stability analysis results, two dynamic sliding mode controllers and a non-overshooting model predictive controller are proposed to guarantee that the vehicle trajectories are always controlled in the estimated stability regions, demonstrated by different simulation and experiment cases.

Third, to fill the theoretical blank when the estimated stability regions are considered as time-varying and control-dependent invariant sets, a novel definition of time-varying control-dependent barrier function (CDBF) is proposed. In the application to the guaranteed vehicle stability control problem, a novel integral control strategy is proposed

and a corresponding new framework of time-varying CDBF is presented with rigorous proofs. Moreover, to address the discontinuity and differentiability of CBF when safety sets are switching, the switched CBF is proposed. Both simulations and experiments are conducted to verify the correctness and effectiveness of the proposed theories and control methods.

The remainder of the dissertation is organized as follows. In Chapter 2, this dissertation first introduces the vehicle model, tire model, and an over-actuated vehicle testbed used for experimental validations. In Chapter 3, targeted at addressing the issues revealed in the existing stability region estimation methods, the details of the proposed local linearization method, together with the corresponding analyses and simulation verifications are introduced. In Chapter 4, important features of the stability regions are first formulated as preliminaries to the controller designs. Then, based on the estimated vehicle lateral stability regions, multiple control methods, including two sliding mode controllers and a non-overshooting model predictive controller, are presented. All controller designs are verified by high-fidelity Carsim-Simulink co-simulations. With the same control objective, in Chapter 5, the novel stability-guaranteed vehicle control methods are introduced. Particularly, new concepts, time-varying control-dependent barrier functions (CDBF) and switched CBF are proposed to address the region-based stability-guaranteed vehicle control problems with high efficiency. The corresponding co-simulations and experimental verifications are presented. Finally, in Chapter 6, the conclusions of the overall dissertation are summarized, and some targeted future works are suggested.

CHAPTER 2

VEHICLE MODEL AND EXPERIMENTAL PLATFORM

In this chapter, as the preliminaries of the overall study, a double-track four-wheel steering vehicle model and a LuGre tire model are first presented. Then, the experimental platform, an over-actuated autonomous ground vehicle (OA-AGV) prototype (designed and manufactured by DSCL), is introduced. The main contents in sections 2.1 and 2.2 follow the same configurations in [94]. The introduction of OA-AGV is part of the author's previous published paper [95] [2].

2.1. Vehicle Model

A two degree of freedom (DOF) four-wheel steering (4WS) vehicle model considering the lateral load transfer is adopted in this dissertation. In Fig. 1, the V_x, V_y, and r are the vehicle longitudinal velocity, lateral velocity, and yaw rate about the center of gravity (CG), respectively.

[2] All the cited contents in sections 2.1 and 2.2 are with permission of Copyright © 2021 ASME, to be reprinted from [Huang, Liang, and Chen, *ASME Journal of Dynamic System, Measurement, and control*, 2021]. The cited contents in section 2.3 are with permission of Copyright © 2021 IEEE, to be reprinted from [Huang, Wang, Li, Shi, and Chen, *IEEE Transactions on Mechatronics*, 2021].

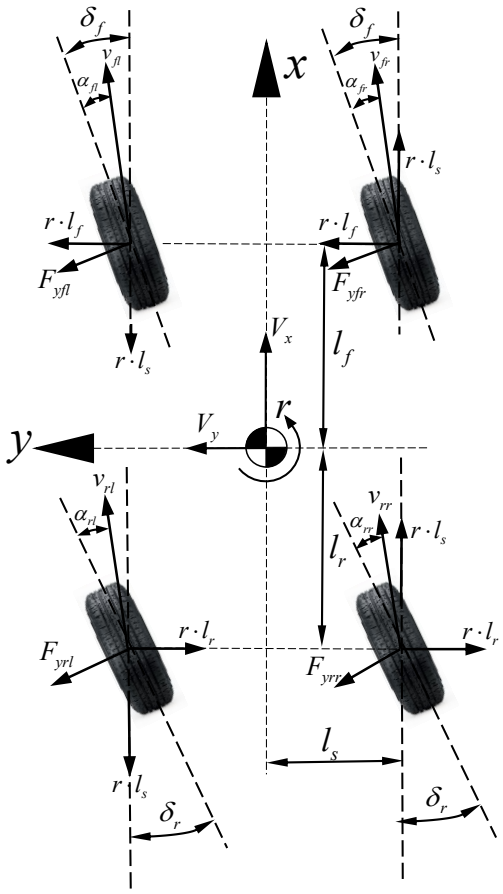

Fig. 1. Diagram of a Four-wheel Vehicle Lateral Dynamic Model.

The vehicle lateral dynamics, with the state variables V_y and r are modelled in (1) and (2),

$$m_v\left(\dot{V}_y + V_x r\right) = \left(F_{yfl} + F_{yflr}\right)\cos\delta_f + F_{yAFS} + \left(F_{yrl} + F_{yrr}\right)\cos\delta_r + F_{yARS} \tag{1}$$

$$\begin{aligned} I_z\dot{r} = {} & l_f\left[\left(F_{yfl} + F_{yflr}\right)\cos\delta_f + F_{yAFS}\right] - l_r\left[\left(F_{yrl} + F_{yrr}\right)\cos\delta_r + F_{yARS}\right] \\ & + l_s\left[\left(F_{yfl} - F_{yfr}\right)\sin\delta_f - \left(F_{yrl} - F_{yrr}\right)\sin\delta_r\right] + M_{DYC} \end{aligned} \tag{2}$$

where m_v, I_z, δ_f, and δ_r are vehicle mass, yaw moment inertia, front steering angle, and rear steering angle, respectively. l_s, l_f, and l_r are wheel track, front wheelbase, and rear

wheelbase, respectively. F_{yj} with the subscript $\{j = fl, fr, rl, rr\}$ denote the tire lateral friction force on the front left, front right, rear left, and rear right tires, respectively. F_{yAFS} and F_{yARS} are the lateral forces generated by the active front and rear wheel steering angles respectively. M_{DYC} is the yaw moment generated by the direct yaw moment controller. Under small angle assumptions, tire slip angles were typically represented in an approximately linear relationship with respect to vehicle states to reduce model complexities in literature [9]-[20]. However, when the vehicle lateral stability in extreme conditions is explored, especially when the tire lateral forces are saturated at large slip angles, the linear approximations may not be accurate. Thus, in this paper, the tire slip angles are calculated without small angle approximations, as shown in (3)-(6). Note that although the left and right wheels are steered differently in a four-wheel vehicle model based on the Ackerman steering geometry, such a difference is not found to have significant impacts on the estimation results of stability regions. Therefore, the steering angles of the front two wheels are kept the same in (3) and (4).

$$\alpha_{fl} = \delta_f - \tan^{-1}\left(\frac{V_y + l_f r}{V_x - rl_s}\right), \tag{3}$$

$$\alpha_{fr} = \delta_f - \tan^{-1}\left(\frac{V_y + l_f r}{V_x + rl_s}\right), \tag{4}$$

$$\alpha_{rl} = \delta_r - \tan^{-1}\left(\frac{V_y - l_r r}{V_x - rl_s}\right), \tag{5}$$

$$\alpha_{rr} = \delta_r - \tan^{-1}\left(\frac{V_y - l_r r}{V_x + rl_s}\right). \tag{6}$$

2.2. Tire Model

A tire model plays a critical role in vehicle stability analysis. Various tire models were developed and discussed in the past few decades, see [79] and references therein. Based on different criteria, tire models have various classifications, such as linear and nonlinear models, physical and empirical models, and static and dynamic models. As an example, the well-known Magic Formula tire model [80] is a nonlinear, empirical, and static tire model, which provides a good fit with the steady-state experimental data. However, the heavy model parameter calibrations for various conditions are challenging for real applications. Compared with the Magic Formula tire model, a modified 2D LuGre tire model [79], which is a nonlinear, physical, and dynamic tire model, does not only describe tire force characteristics well but also provides a relatively easy procedure for model calibrations. Therefore, a 2D LuGre tire model, as expressed in (7), is adopted in this paper.

$$\begin{aligned} F_{iss} &= f\left(\lambda,\alpha,F_n,\mu\right) \\ &= F_n\left\{\frac{g_i^2 v_{ri}}{\gamma\left(v_r,\mu\right)}\left[1-\frac{\beta_i}{a_i^2}\left(\frac{e^{-a_i L_i}-e^{-a_i\left(L_i-\zeta_{Li}\right)}}{\zeta_{Li}}-\right.\right.\right. \\ &\qquad \left.\left.\left.\frac{e^{-a_i\left(L_i-\zeta_{Ri}\right)}-1}{L_i-\zeta_{Ri}}\right)\right]+\sigma_{2i}v_{ri}\right\}, i=x,y \end{aligned} \tag{7}$$

In (7), the tire friction force F_{iss} is a function of four main parameters $\left(\lambda,\alpha,F_n,\mu\right)$, where λ is the tire slip ratio, α is the tire slip angle, F_n is the tire vertical load, and μ is the tire-road friction coefficient. Three terms in the brace of (7), namely $\frac{g_i^2 v_{ri}}{\gamma\left(v_r,\mu\right)}$, expression in the square bracket, and $\sigma_{2i}v_{ri}$, describe the Stribeck effect, the trapezoidal load distribution,

and the viscous damping property of tire materials, respectively. More details of parameters (such as the formulation of g_i, a_i, and $\gamma(v_r,\mu)$) and features of the adopted 2D LuGre model are referred to [79] and references therein. Note that one main feature of the adopted LuGre tire model is that the effect of vertical loads is embedded into the bristle dynamics. Thus, the bristle deflection distribution predicted by the derived model matches better with the experimental data [79].

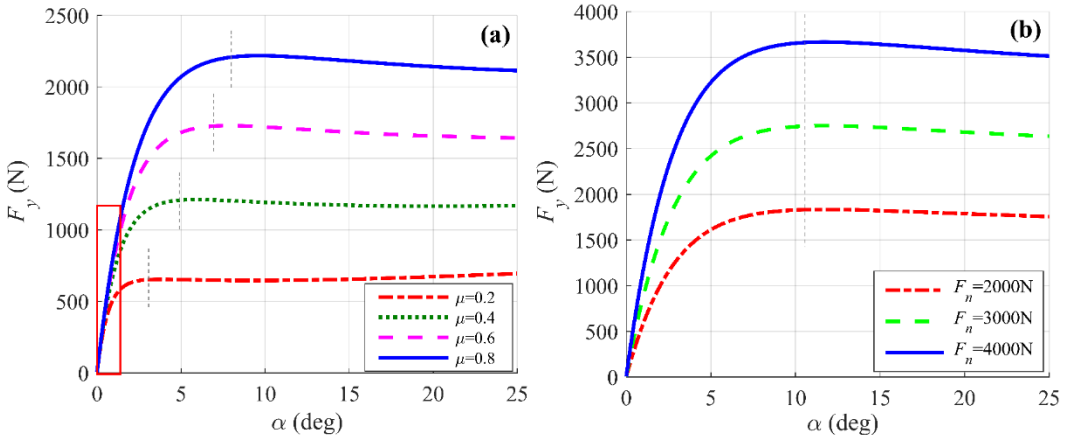

Fig. 2. (a) Tire Lateral Friction Forces with Different μ for a Fixed $F_n = 3000N$; (b) Tire Lateral Friction Forces with Different F_n for a Fixed $\mu = 1$.

Based on the 2D LuGre tire model in (7), the lateral friction forces for different μ and F_n are plotted in Fig. 2. As shown in Fig. 2 (a), the slopes of different curves with different μ are approximately the same when the slip angles are small (mainly in the red box area), which displays a linear similarity relationship between F_y and α [82]. Fig. 2 (b) shows the lateral force curves with different vertical loads, which are mainly determined by both static load distributions and dynamic load transfers. Particularly, the dynamic load transfer

has significant impacts on vehicle stability, which is thoroughly discussed in section 3.2.4, Chapter 3. The tire vertical forces considering both static load distributions and dynamic load transfers (with respect to a_y) are calculated in (8)-(11) [80][85].

$$F_{nfl} = \frac{m_v}{2L}\left(gl_r - \frac{h_{CG} a_y l_r}{l_s} \right), \tag{8}$$

$$F_{nfr} = \frac{m_v}{2L}\left(gl_r + \frac{h_{CG} a_y l_r}{l_s} \right), \tag{9}$$

$$F_{nrl} = \frac{m_v}{2L}\left(gl_f - \frac{h_{CG} a_y l_f}{l_s} \right), \tag{10}$$

$$F_{nrr} = \frac{m_v}{2L}\left(gl_f + \frac{h_{CG} a_y l_f}{l_s} \right), \tag{11}$$

where h_{CG} is the height of the vehicle CG and a_y is the vehicle lateral acceleration.

Moreover, when the slip angles exceed certain values (marked by grey dash lines), it is observed from Fig. 2 that the lateral friction forces start to saturate and even decrease. For different μ in Fig. 2 (a), the saturated tire slip angles are different. While for different F_n in Fig. 2 (b), the saturated tire slip angles are almost the same. These observations show that the friction force saturation (peak points) is more sensitive to μ than F_n. In fact, the tires start to operate in an unstable manner when the friction forces start to saturate or decrease with the increase of tire slip angles. Consequently, the vehicle will likely lose stability when tire lateral forces become unstable.

Remark 1. The analytical and physical LuGre model is applied in this paper to represent a complex and realistic tire model. Since the local linearization method introduced in the

next section, which can be numerically implemented, does not require an *explicit* integration of a tire model with a vehicle model, any other high-fidelity tire models could be also applied for the stability region estimation through the same proposed method. On the other hand, if other methods, like Lyapunov-based methods, were applied, a complex tire model may have to be avoided since an explicit integration of the tire model with vehicle dynamics may be difficult to construct suitable Lyapunov functions.

2.3. Over-Actuated Electric Vehicle Platform

AGVs are currently seen to have significant improvement in the areas of perceptional and artificial intelligence technology, yet their actuation and control capabilities, critical for improving system safety, are still lagging behind. Current AGVs still operate on the basis of the traditional centralized powertrain used in human-driven cars, which is considered a major limitation for further improving vehicle safety, energy efficiency, and riding comfort. The recent explosion of vehicle electrification technologies, such as in-wheel motor (IWM) actuation and steering-by-wire (SbW) technology, has fostered an increased pace towards a distributed electric powertrain architecture for vehicle systems. Despite some limitations (e.g., increased un-sprung mass by IWMs), such an over-actuated (OA) feature, enabled by the number of actuators more than the control degrees of freedom, provides great potentials to further enhance AGV safety, efficiency, and riding comfort. As part of this dissertation, an OA-GV prototype was developed as the testbed for the vehicle lateral stability controller verifications. The configuration and hardware development of the OA-AGV are presented in Fig. 3. Some major vehicle parameters of the developed OA-AGV are listed in Table 1.

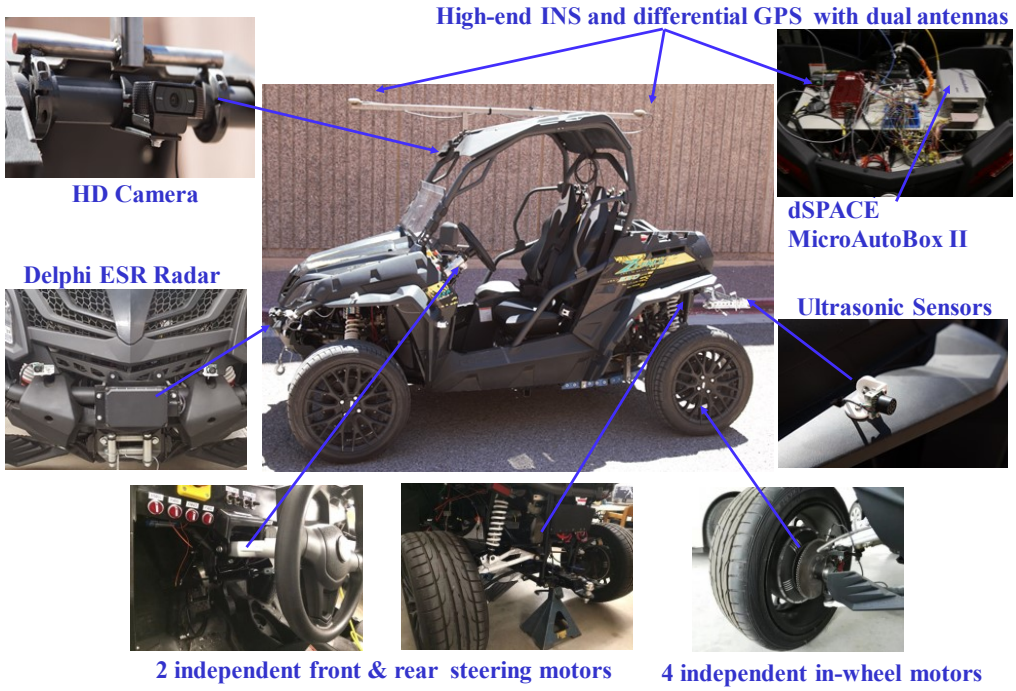

Fig. 3. The Developed Over-actuated AGV Prototype.

Table 1. Parameters of the Over-actuated Vehicle Testbed

Symbol	Parameter	Value
m	vehicle mass	732.5 kg
L	wheelbase	2.08 m
l_f	front wheelbase	1.12 m
l_r	rear wheelbase	0.96 m
l_s	wheel track	1.26 m
I_z	yaw moment of inertia	352 kgm^2
h_{CG}	CG height	0.65 m
P_{motor}	power of IWM	8 kW
P_{steer}	power of steering motor	400 W

2.3.1. Power System Configuration

The power supply of the OA-AGV is a package of the 72V, 125Ah $LiFePO_4$ battery equipped with a battery management system (BMS). The actuators of the OA-AGV include

four in-wheel motors (IWMs) and two servo steering motors. The IWM, which is the permanent-magnet brushless DC (BLDC) motor, is directly powered and controlled by the Mobipus® 72300 motor controller. Similarly, the steering motors also have two servo motor controllers, which require 220V AC power. To invert the DC power from the battery to the AC power, two inverters are equipped. All other on-board devices (e.g. dSPACE® MicroAutoBox and RT3003 GPS) and sensors are powered by a 12V DC, which is obtained using a DC-DC voltage regulator.

2.3.2. Control System Configuration

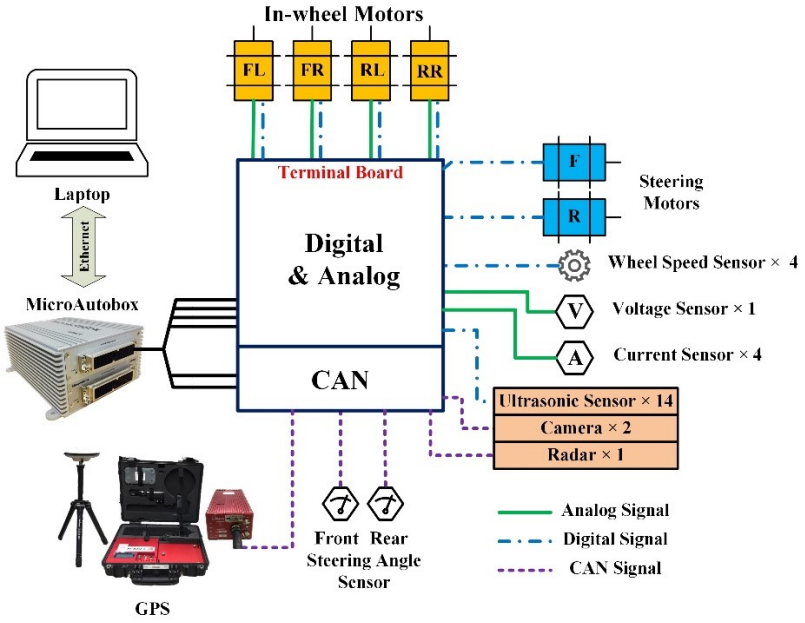

Fig. 4. Control Configuration of the Over-actuated AGV.

The control system configuration of the developed OA-AGV is constructed in a hierarchical architecture, namely a high-level vehicle control and low-level actuator controls. As shown in Fig. 4, the dSPACE® MicroAutoBox II (MAB-II) is the main high-level control module. A high-end laptop, which is connected with the MAB-II via Ethernet,

is used for real-time state monitoring and data acquisition. All the signals (analog, digital, and CAN signals) can directly communicate with the MAB-II through a central terminal board.

At the low level, each IWM is individually controlled by a Mobipus® 72300 series controller. Analog signals from the MAB-II are given to the motor controller as the throttle and regenerative braking signals. Digital signals are also provided for the motor mode selections. At each wheel, a wheel speed sensor and a current sensor are equipped for wheel speed and current measurement, respectively. Each steering motor is controlled by a Delta® ASDA-A2 series high-resolution AC servo drive, where the required steering angles from the high level are transferred to PWM signals in servo drives. Using the steering angle measured by the steering angle encoder, a calibrated PID control is designed to achieve the desired steering actuation.

2.3.3. Redundant Actuation Systems

The over-actuation of the developed OA-AGV is realized by multiple electric motors. Compared with the centralized engine or motor powertrain, four independently actuated IWMs are equipped in a distributed manner, which introduces two main advantages. First, from the energy consumption point of view, the IWM normally has higher energy operational efficiency than that of the engine. Second, the four IWMs without the transmissions and differentials can provide faster torque responses and more control degrees of freedom. Moreover, two steering motors for the front and rear wheel independent steering or four-wheel steering (4WS) of the OA-AGV are also applied. The additional active rear wheel steering system (ARS) can help to improve the stability and

energy efficiency of the OA-AGV, which will be discussed in detail in the following sections.

2.3.4. Sensing Systems

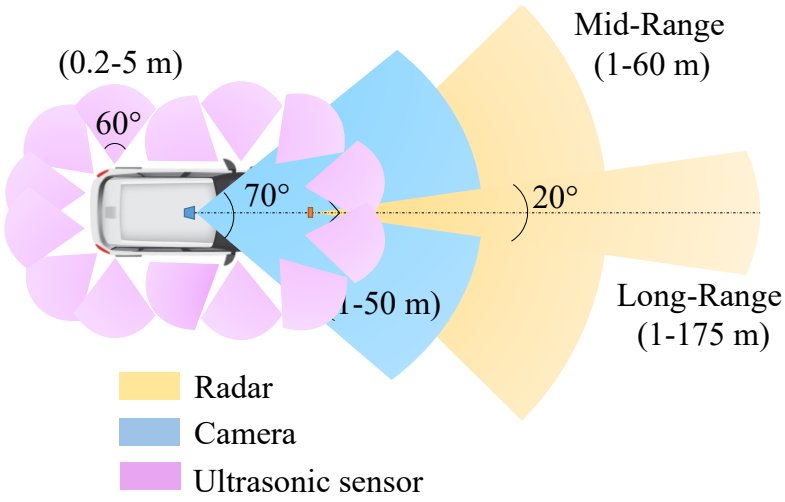

Fig. 5. Sensing Systems of the OA-AGV.

As shown in Fig. 5, three different sensing systems, namely, a camera-based vision system, a radar-based perception system, and an ultrasonic sensor-based detection system, are equipped on the developed OA-AGV. The usage and application of the sensors are briefly described as follows.

In the camera-based vision system, a 1080p HD camera with a 78° diagonal field of view (FOV) is mounted at the top of the front windshield, see Fig. 3. Every 30 ms, the camera collects the image information to identify desired environmental objects, such as the lane boundaries, through the lane detection algorithm in Python. Based on the detected lane information, the vehicle lateral offset with respect to the lane centerline can be determined and utilized for the lane-keeping control.

In the radar-based perception system, a Delphi® ESR 2.5 radar is mounted in the front of the vehicle, see Fig. 3. The radar detects up to 64 objects in the mid-range (1-60 m) or the long-range (1-175 m) within ±45° FOV or ±10° FOV, respectively. The detected object information, such as radial distances, azimuth angles, and relative speeds with respect to the radar, can be obtained and sent to the MAB-II through a CAN bus with a Kvaser® CAN adapter.

In the ultrasonic sensor-based detection system, as shown in Fig. 5, fourteen I2CXL-MaxSonar ultrasonic sensors are arranged to cover 360 degrees FOV around the vehicle. The effective detection range of the ultrasonic sensor is 0.2-5 m. The reading of the sensors refreshes every 20 ms, which allows a fast response for applications, like automatic parking. In addition, the vehicle kinematic and dynamic states are measured by the RT 3003 differential GPS and INS system, which are fed to the MAB-II for real-time control purposes.

CHAPTER 3

VEHICLE LATERAL DRIVING STABILITY REGION

As discussed in Chapter 1, the estimation of vehicle lateral driving stability regions is fundamental to the stability analysis and controller designs. Based on the vehicle model and tire model introduced in Chapter 2, a novel vehicle lateral driving stability estimation method was proposed. As a summary of the author's previously published paper [94], the details of the proposed estimation method are presented in this chapter [3].

3.1. Overview

Among various vehicle lateral stability analyses, the vehicle lateral stability regions are regarded as the most intuitive and efficient ones by depicting a region on a phase plane that can consist of different vehicle state combinations (e.g. vehicle lateral velocity (or sideslip angle) and yaw rate). Although the existing studies have estimated and revealed different features of vehicle lateral stability regions, some issues still need to be further investigated, especially in the context of AGVs. For instance, some unstable (even temporarily) driving maneuvers that are predictable or acceptable for human-driven vehicles (through human commands), such as understeering or oversteering, may cause serious safety issues for AGVs. Therefore, it is necessary to develop a more comprehensive and safer vehicle lateral driving stability region. However, the existing vehicle lateral stability regions do not always effectively reflect the actual factors related to vehicle stability due to the lack of analysis from practical perspectives, such as the handling characteristic. To get a more

[3] The main contents in this chapter are with permission of Copyright © 2021 ASME, to be reprinted from [Huang, Liang, and Chen, *ASME Journal of Dynamic System, Measurement, and control*, 2021].

accurate description of vehicle safety with a particular focus on vehicle dynamic/handling stability analysis, a novel estimation method is proposed and introduced in this chapter.

3.2. Stability Region Estimation

3.2.1. Local Linearization Method

The process of the local linearization method is described as follows. First, the vehicle model in (1) and (2) is symbolized into (12).

$$\begin{bmatrix} \dot{V}_y \\ \dot{r} \end{bmatrix} \triangleq f\left(\left(V_y, r\right)^T, \delta_f\right). \tag{12}$$

Defining an operation point with a subscript o, and applying the Taylor expansion to the general dynamic function f in (12) with respect to the system variables (V_y and r) and the system input (δ_f), (12) is approximately rewritten as

$$\begin{aligned} \begin{bmatrix} \dot{V}_y \\ \dot{r} \end{bmatrix} \triangleq \begin{bmatrix} \dot{V}_{yo} \\ \dot{r}_o \end{bmatrix} + \begin{bmatrix} \Delta\dot{V}_y \\ \Delta\dot{r} \end{bmatrix} \approx f\left(\left(V_{yo}, r_o\right)^T, \delta_{fo}\right) + \left.\frac{\partial f}{\partial V_y}\right|_{\left(V_{yo}, r_o\right)} \Delta V_y \\ + \left.\frac{\partial f}{\partial r}\right|_{\left(V_{yo}, r_o\right)} \Delta r + \left.\frac{\partial f}{\partial \delta_f}\right|_{\left(V_{yo}, r_o\right)} \Delta\delta_f \end{aligned}. \tag{13}$$

On the right side of (13), the high-order terms of the Taylor expansion are ignored for linearization. Note that $\begin{bmatrix} \dot{V}_{yo} \\ \dot{r}_o \end{bmatrix} = f\left(\left(V_{yo}, r_o\right)^T, \delta_{fo}\right)$ is generally obtained on the trajectory of dynamic systems. In a specific situation that the operation point is an equilibrium, we will have $\begin{bmatrix} \dot{V}_{yo} \\ \dot{r}_o \end{bmatrix} = f\left(\left(V_{yo}, r_o\right)^T, \delta_{fo}\right) = \begin{bmatrix} 0 \\ 0 \end{bmatrix}$. Thus, by canceling the equalized items on both sides of (13), the linearized system at the operation point for a given input δ_{fo} is obtained as,

$$\begin{bmatrix} \Delta \dot{V}_y \\ \Delta \dot{r} \end{bmatrix} = A_o \begin{bmatrix} \Delta V_y \\ \Delta r \end{bmatrix} + B_o \Delta \delta_f \,, \tag{14}$$

where $A_o = \begin{bmatrix} \left.\dfrac{\partial f}{\partial V_y}\right|_{(V_{yo}, r_o)} & \left.\dfrac{\partial f}{\partial r}\right|_{(V_{yo}, r_o)} \end{bmatrix}$ and $B_o = \left.\dfrac{\partial f}{\partial \delta_f}\right|_{(V_{yo}, r_o)}$.

To further derive the expressions of matrices A_o and B_o, the partial derivatives of lateral friction forces are derived as (15)-(17).

$$\frac{\partial F_y}{\partial V_y} = \frac{\partial F_y}{\partial \alpha} \frac{\partial \alpha}{\partial V_y}, \tag{15}$$

$$\frac{\partial F_y}{\partial r} = \frac{\partial F_y}{\partial \alpha} \frac{\partial \alpha}{\partial r}, \tag{16}$$

$$\frac{\partial F_y}{\partial \delta_f} = \frac{\partial F_y}{\partial \alpha} \frac{\partial \alpha}{\partial \delta_f}, \tag{17}$$

where $\dfrac{\partial F_y}{\partial \alpha} = C_\alpha(\alpha)$ is the linearized lateral friction force function (not a constant but a slope function of the lateral force curve) at a slip angle α. As shown in Fig. 2, the stable lateral friction forces (before reaching the saturation points) always have positive slopes $C_\alpha(\alpha) > 0$. Based on (3)-(6), the partial derivatives of tire slip angles with respect to V_y, r, and δ_f are expressed as follows.

$$\begin{cases} \dfrac{\partial \alpha_{fl}}{\partial V_y} = \dfrac{\partial \alpha_{rl}}{\partial V_y} = -\dfrac{1}{V_x - r_o l_s} \\ \dfrac{\partial \alpha_{fr}}{\partial V_y} = \dfrac{\partial \alpha_{rr}}{\partial V_y} = -\dfrac{1}{V_x + r_o l_s} \end{cases}, \tag{18}$$

$$\begin{cases} \dfrac{\partial \alpha_{fl}}{\partial r} = -\dfrac{l_f V_x + V_{yo} l_s}{\left(V_x - r_o l_s\right)^2} \\ \dfrac{\partial \alpha_{fr}}{\partial r} = -\dfrac{l_f V_x - V_{yo} l_s}{\left(V_x + r_o l_s\right)^2} \\ \dfrac{\partial \alpha_{rl}}{\partial r} = -\dfrac{-l_r V_x + V_{yo} l_s}{\left(V_x - r_o l_s\right)^2} \\ \dfrac{\partial \alpha_{rr}}{\partial r} = -\dfrac{-l_r V_x - V_{yo} l_s}{\left(V_x + r_o l_s\right)^2} \end{cases}, \tag{19}$$

$$\frac{\partial \alpha_{fl}}{\partial \delta_f} = \frac{\partial \alpha_{fr}}{\partial \delta_f} = 1,\ \frac{\partial \alpha_{rl}}{\partial \delta_f} = \frac{\partial \alpha_{rr}}{\partial \delta_f} = 0. \tag{20}$$

Note that the high-order items in the derivation of (18)-(20) are small enough to be negligible. Thus, by substituting (1), (2) and (15)-(20) into (14), A_o and B_o with respect to the operation point $\left(V_{yo}, r_o\right)$ can be obtained and expressed as follows,

$$A_o = \begin{bmatrix} A_{o11} & A_{o12} \\ A_{o21} & A_{o22} \end{bmatrix}, \tag{21}$$

$$B_o = \begin{bmatrix} \dfrac{C_{\alpha fl} + C_{\alpha fr}}{m} \\ \dfrac{\left(C_{\alpha fl} + C_{\alpha fr}\right) l_f + \left(F_{yfl} - F_{yfr}\right) l_s}{I_z} \end{bmatrix}. \tag{22}$$

where,

$$A_{o11} = -\left(\frac{C_{\alpha fl} + C_{\alpha rl}}{m\left(V_x - r_o l_s\right)} + \frac{C_{\alpha fr} + C_{\alpha rr}}{m\left(V_x + r_o l_s\right)} \right), \tag{23}$$

$$A_{o12} = -V_x - \frac{1}{m_v}\left(\frac{\left(l_f V_x + V_{yo} l_s\right) C_{\alpha fl} + \left(-l_r V_x + V_{yo} l_s\right) C_{\alpha rl}}{\left(V_x - r_o l_s\right)^2} + \frac{\left(l_f V_x - V_{yo} l_s\right) C_{\alpha fr} + \left(-l_r V_x - V_{yo} l_s\right) C_{\alpha rr}}{\left(V_x + r_o l_s\right)^2} \right),$$

$$A_{o21} = \frac{1}{I_z}\left(\frac{-l_f C_{\alpha fl} + C_{\alpha rl} l_r}{V_x - r_o l_s} + \frac{-l_f C_{\alpha fr} + C_{\alpha rr} l_r}{V_x + r_o l_s} \right),$$

$$A_{o22} = \frac{1}{I_z}\left(\frac{-\left(l_f V_x + V_{yo} l_s\right) l_f C_{\alpha fl} + \left(-l_r V_x + V_{yo} l_s\right) l_r C_{\alpha rl}}{\left(V_x - r_o l_s\right)^2} + \frac{-\left(l_f V_x - V_{yo} l_s\right) l_f C_{\alpha fr} + \left(-l_r V_x - V_{yo} l_s\right) l_r C_{\alpha rr}}{\left(V_x + r_o l_s\right)^2} \right).$$

Proposition 1. The linearized system in (14) is asymptotic stable with respect to the operation point $\left(V_{yo}, r_o\right)$ if and only if the inequality in (24) holds.

$$L - \frac{m_v \left(V_x^{\,2} - l_s^{\,2} r_o^{\,2}\right)\left[\left(C_{\alpha fl} + C_{\alpha fr}\right) l_f - \left(C_{\alpha rl} + C_{\alpha rr}\right) l_r\right]}{L\left(C_{\alpha fl} + C_{\alpha fr}\right)\left(C_{\alpha rl} + C_{\alpha rr}\right)} > 0, \tag{24}$$

where $L = l_f + l_r$ is the vehicle wheelbase.

Proof. The characteristics of eigenvalues of A_o is utilized to prove the system stability. Let

$$\left|\lambda I - A_o\right| = \begin{bmatrix} \lambda - A_{o11} & -A_{o12} \\ -A_{o21} & \lambda - A_{o22} \end{bmatrix} = \lambda^2 + p_1 \lambda + p_0 = 0, \tag{25}$$

where

$$p_1 = -A_{o11} - A_{o22}, \tag{26}$$

$$p_0 = A_{o11} A_{o22} - A_{o12} A_{o21}. \tag{27}$$

Instead of directly calculating the two eigenvalues of A_o, the coefficients of the characteristic equation (25) are utilized to prove Hurwitz stability. Based on the *Routh–Hurwitz criterion* [83] for second-order polynomials, if and only if p_1 and p_0 are both positive, the eigenvalues of (25) have negative real parts. Therefore, as long as inequality (24) is equal to positive p_1 and p_0, the stability of the linearized system is proved. First, for p_1, substituting A_{o11} and A_{o22} from (23) into (26), p_1 is given as,

$$p_1 = \left[\frac{C_{\alpha fl} + C_{\alpha rl}}{m_v\left(V_x - r_o l_s\right)} + \frac{C_{\alpha fr} + C_{\alpha rr}}{m_v\left(V_x + r_o l_s\right)} \right] + \frac{1}{I_z}\left[\frac{\left(l_f V_x + V_{yo} l_s\right) l_f C_{\alpha fl}}{\left(V_x - r_o l_s\right)^2} + \frac{\left(l_r V_x + V_{yo} l_s\right) l_r C_{\alpha rr}}{\left(V_x + r_o l_s\right)^2} + \frac{\left(l_r V_x - V_{yo} l_s\right) l_r C_{\alpha rl}}{\left(V_x - r_o l_s\right)^2} + \frac{\left(l_f V_x - V_{yo} l_s\right) l_f C_{\alpha fr}}{\left(V_x + r_o l_s\right)^2} \right]. \tag{28}$$

Since the linearized cornering stiffness $C_{\alpha j}\left(j = fl, fr, rl, rr\right)$ are always positive if the friction forces are stable (not reach and beyond the saturation points) and $\left(V_x - r_o l_s\right)$ is positive for general vehicle driving conditions, the sum in the first square bracket of (28) is positive. Moreover, the first two terms in the second square bracket of (28) are always positive and the sign of the last two terms are determined by the numerators. Since V_y is much smaller than V_x for general driving conditions and l_s, l_f, and l_r are comparable vehicle dimensions, the $\left(l_r V_x - V_{yo} l_s\right)$ and $\left(l_f V_x - V_{yo} l_s\right)$ in the two numerators are also positive. Thus, p_1 is positive based on the analyses of vehicle driving conditions.

Second, by substituting (23) into (27), it is proved that the inequality in (24) is equivalent to a positive p_0. The positive condition of p_0 can be written in (29) as

$$p_0 = A_{o11}A_{o22} - A_{o12}A_{o21} > 0\,. \tag{29}$$

Substituting the elements of A_o matrix from (23) to (29),

$$\begin{aligned} p_0 = & \left(\frac{C_{\alpha fl} + C_{\alpha rl}}{m_v\left(V_x - r_o l_s\right)} + \frac{C_{\alpha fr} + C_{\alpha rr}}{m_v\left(V_x + r_o l_s\right)} \right) \\ & \frac{1}{I_z}\left(\begin{array}{c} \frac{\left(l_f V_x + V_{yo} l_s\right) l_f C_{\alpha fl} - \left(-l_r V_x + V_{yo} l_s\right) l_r C_{\alpha rl}}{\left(V_x - r_o l_s\right)^2} + \\ \frac{\left(l_f V_x - V_{yo} l_s\right) l_f C_{\alpha fr} - \left(-l_r V_x - V_{yo} l_s\right) l_r C_{\alpha rr}}{\left(V_x + r_o l_s\right)^2} \end{array} \right) \\ & + \left[V_x + \frac{1}{m_v}\left(\begin{array}{c} \frac{\left(l_f V_x + V_{yo} l_s\right) C_{\alpha fl} + \left(-l_r V_x + V_{yo} l_s\right) C_{\alpha rl}}{\left(V_x - r_o l_s\right)^2} + \\ \frac{\left(l_f V_x - V_{yo} l_s\right) C_{\alpha fr} + \left(-l_r V_x - V_{yo} l_s\right) C_{\alpha rr}}{\left(V_x + r_o l_s\right)^2} \end{array} \right) \right]. \\ & \frac{1}{I_z}\left(\frac{-l_f C_{\alpha fl} + C_{\alpha rl} l_r}{V_x - r_o l_s} + \frac{-l_f C_{\alpha fr} + C_{\alpha rr} l_r}{V_x + r_o l_s} \right) > 0 \end{aligned} \tag{30}$$

Since $\left(\frac{1}{I_z} \frac{1}{m_v} \right)$ is always positive, which can be eliminated from both sides of (30), the items in the brackets are expanded and rearranged as,

$$
\begin{aligned}
&\frac{\left(l_f V_x + V_{yo} l_s\right) l_f C_{\alpha fl}\left(C_{\alpha fl} + C_{\alpha rl}\right)}{\left(V_x - r_o l_s\right)^3} - \frac{\left(-l_r V_x + V_{yo} l_s\right) l_r C_{\alpha rl}\left(C_{\alpha fl} + C_{\alpha rl}\right)}{\left(V_x - r_o l_s\right)^3} \\
&+ \frac{\left(l_f V_x - V_{yo} l_s\right) l_f C_{\alpha fr}\left(C_{\alpha fr} + C_{\alpha rr}\right)}{\left(V_x + r_o l_s\right)^3} - \frac{\left(-l_r V_x - V_{yo} l_s\right) l_r C_{\alpha rr}\left(C_{\alpha fr} + C_{\alpha rr}\right)}{\left(V_x + r_o l_s\right)^3} \\
&+ \frac{1}{\left(V_x - r_o l_s\right)\left(V_x + r_o l_s\right)}\left[\frac{\left(l_f V_x + V_{yo} l_s\right) l_f C_{\alpha fl}\left(C_{\alpha fl} + C_{\alpha rl}\right)}{\left(V_x - r_o l_s\right)}\right. \\
&- \frac{\left(-l_r V_x + V_{yo} l_s\right) l_r C_{\alpha rl}\left(C_{\alpha fl} + C_{\alpha rl}\right)}{\left(V_x - r_o l_s\right)} + \frac{\left(l_f V_x - V_{yo} l_s\right) l_f C_{\alpha fr}\left(C_{\alpha fr} + C_{\alpha rr}\right)}{\left(V_x + r_o l_s\right)} \\
&\left. - \frac{\left(-l_r V_x - V_{yo} l_s\right) l_r C_{\alpha rr}\left(C_{\alpha fr} + C_{\alpha rr}\right)}{\left(V_x + r_o l_s\right)}\right] \\
&> -\left[m_v V_x\left(\frac{-l_f C_{\alpha fl} + C_{\alpha rl} l_r}{V_x - r_o l_s} + \frac{-l_f C_{\alpha fr} + C_{\alpha rr} l_r}{V_x + r_o l_s}\right)\right. \\
&+ \frac{\left(l_f V_x + V_{yo} l_s\right) l_f C_{\alpha fl}\left(-l_f C_{\alpha fl} + C_{\alpha rl} l_r\right)}{\left(V_x - r_o l_s\right)^3} \\
&- \frac{\left(-l_r V_x + V_{yo} l_s\right) l_r C_{\alpha rl}\left(-l_f C_{\alpha fl} + C_{\alpha rl} l_r\right)}{\left(V_x - r_o l_s\right)^3} \\
&+ \frac{\left(l_f V_x - V_{yo} l_s\right) l_f C_{\alpha fr}\left(-l_f C_{\alpha fr} + C_{\alpha rr} l_r\right)}{\left(V_x + r_o l_s\right)^3} \\
&- \frac{\left(-l_r V_x - V_{yo} l_s\right) l_r C_{\alpha rr}\left(-l_f C_{\alpha fr} + C_{\alpha rr} l_r\right)}{\left(V_x + r_o l_s\right)^3} \\
&+ \frac{1}{\left(V_x - r_o l_s\right)\left(V_x + r_o l_s\right)}\left(\frac{\left(l_f V_x + V_{yo} l_s\right) l_f C_{\alpha fl}\left(-l_f C_{\alpha fl} + C_{\alpha rl} l_r\right)}{\left(V_x - r_o l_s\right)}\right. \\
&- \frac{\left(-l_r V_x + V_{yo} l_s\right) l_r C_{\alpha rl}\left(-l_f C_{\alpha fl} + C_{\alpha rl} l_r\right)}{\left(V_x - r_o l_s\right)} \\
&+ \frac{\left(l_f V_x - V_{yo} l_s\right) l_f C_{\alpha fr}\left(-l_f C_{\alpha fr} + C_{\alpha rr} l_r\right)}{\left(V_x + r_o l_s\right)} \\
&\left.\left. - \frac{\left(-l_r V_x - V_{yo} l_s\right) l_r C_{\alpha rr}\left(-l_f C_{\alpha fr} + C_{\alpha rr} l_r\right)}{\left(V_x + r_o l_s\right)}\right)\right]
\end{aligned}
\tag{31}
$$

.

Combine and eliminate the same items on both sides of (31),

$$\begin{aligned}
&V_x\left[\frac{\left(C_{\alpha fl}+C_{\alpha fr}\right)^2 l_f^2+\left(C_{\alpha fl}+C_{\alpha fr}\right)\left(C_{\alpha rl}+C_{\alpha rr}\right)l_r^2}{\left(V_x{}^2-l_s{}^2r_o{}^2\right)}\right.\\
&\left.+\frac{\left(C_{\alpha fl}+C_{\alpha fr}\right)\left(C_{\alpha rl}+C_{\alpha rr}\right)l_f^2+\left(C_{\alpha rl}+C_{\alpha rr}\right)^2 l_r^2}{\left(V_x{}^2-l_s{}^2r_o{}^2\right)}\right]\\
&>m_vV_x\left(\left(C_{\alpha fl}+C_{\alpha fr}\right)l_f-\left(C_{\alpha rl}+C_{\alpha rr}\right)l_r\right)\\
&+V_x\left[\frac{\left(C_{\alpha fl}+C_{\alpha fr}\right)^2 l_f^2-2\left(C_{\alpha fl}+C_{\alpha fr}\right)\left(C_{\alpha rl}+C_{\alpha rr}\right)l_fl_r}{\left(V_x{}^2-l_s{}^2r_o{}^2\right)}+\frac{\left(C_{\alpha rl}+C_{\alpha rr}\right)^2 l_r^2}{\left(V_x{}^2-l_s{}^2r_o{}^2\right)}\right]
\end{aligned} \quad . \tag{32}$$

In (32), move the second item on the right side of the inequality to the left,

$$\begin{aligned}
&V_x\left[\frac{\left(C_{\alpha fl}+C_{\alpha fr}\right)^2 l_f^2+\left(C_{\alpha fl}+C_{\alpha fr}\right)\left(C_{\alpha rl}+C_{\alpha rr}\right)l_r^2}{\left(V_x{}^2-l_s{}^2r_o{}^2\right)}\right.\\
&+\frac{\left(C_{\alpha fl}+C_{\alpha fr}\right)\left(C_{\alpha rl}+C_{\alpha rr}\right)l_f^2+\left(C_{\alpha rl}+C_{\alpha rr}\right)^2 l_r^2}{\left(V_x{}^2-l_s{}^2r_o{}^2\right)}\\
&-\frac{\left(C_{\alpha fl}+C_{\alpha fr}\right)^2 l_f^2-2\left(C_{\alpha fl}+C_{\alpha fr}\right)\left(C_{\alpha rl}+C_{\alpha rr}\right)l_fl_r}{\left(V_x{}^2-l_s{}^2r_o{}^2\right)}\\
&\left.-\frac{\left(C_{\alpha rl}+C_{\alpha rr}\right)^2 l_r^2}{\left(V_x{}^2-l_s{}^2r_o{}^2\right)}\right]>m_vV_x\left(\left(C_{\alpha fl}+C_{\alpha fr}\right)l_f-\left(C_{\alpha rl}+C_{\alpha rr}\right)l_r\right)
\end{aligned} \quad . \tag{33}$$

The same items on the left of (33) can be combined and eliminated. Thus, (33) is simplified as,

$$\begin{aligned}
&\frac{V_x}{\left(V_x{}^2-l_s{}^2r_o{}^2\right)}\left(C_{\alpha fl}+C_{\alpha fr}\right)\left(C_{\alpha rl}+C_{\alpha rr}\right)(l_f+l_r)^2\\
&>m_vV_x\left(\left(C_{\alpha fl}+C_{\alpha fr}\right)l_f-\left(C_{\alpha rl}+C_{\alpha rr}\right)l_r\right)
\end{aligned} \quad . \tag{34}$$

Finally, (34) is organized as,

$$(l_f + l_r) - \frac{m_v\left(V_x^{\,2} - l_s^{\,2} r_o^{\,2}\right)\left[\left(C_{\alpha fl} + C_{\alpha fr}\right) l_f - \left(C_{\alpha rl} + C_{\alpha rr}\right) l_r\right]}{(l_f + l_r)\left(C_{\alpha fl} + C_{\alpha fr}\right)\left(C_{\alpha rl} + C_{\alpha rr}\right)} > 0 . \tag{35}$$

Therefore, the stability condition in (29) is proved to be the same as the condition in (35), which finally gives the condition in (24). ■

Remark 2. The inequality in (24) illustrates the relationship between the front and rear tire stabilities. Note that the $C_{\alpha j}\left(\alpha_j\right)$, which denotes the varying slopes of lateral friction forces at the slip angle α_j, describes the tire stability information at the operation point.

In addition to the stability analysis, the controllability of the linearized system (14) is determined by checking the rank of the controllability matrix $P = \begin{bmatrix} B_o & A_o B_o \end{bmatrix}$. Since A_o is full rank, as long as $B_o \neq \begin{bmatrix} 0 \\ 0 \end{bmatrix}$, the controllability matrix P is full rank. Thus, from (22), the controllability conditions are,

$$C_{\alpha fl} + C_{\alpha fr} \neq 0, \tag{36}$$

$$\left(C_{\alpha fl} + C_{\alpha fr}\right) l_f + \left(F_{yfl} - F_{yfr}\right) l_s \neq 0 . \tag{37}$$

Since $C_{\alpha j}\left(j = fl, fr, rl, rr\right)$ are required to be positive to ensure tire stability, the inequality (36) holds. Moreover, since the lateral force difference between the front two wheels is typically small, if (36) holds, then (37) also holds. Namely, if the front tires are stable, the controllability of the linearized system is guaranteed.

To summarize, only when the linearized system at the operation point $\left(V_{yo}, r_o\right)$ satisfies both the stability and controllability criteria, the vehicle state at the operation point on the

V_y - r phase plane is defined as (directional) stable. By checking the stability of the linearized system at each (discrete) point in the phase plane, the final estimated vehicle lateral stability region consists of all of the stable operation points, which include but are not limited to the stable equilibrium points [10]. For the linearized system, the local stability describes the system's capability of returning to the operation point under disturbances. Such a concept applied to vehicle stability analysis refers to certain physical and driving properties, which are discussed in the following subsection.

3.2.2. Analyses and Discussions of Stability Criteria

The vehicle lateral stability examined at each operation point physically corresponds to the vehicle handling stability at the same operation point. In the concept of vehicle handling stability, three vehicle status, namely neutral steering, understeering, and oversteering [13][14][81][84] are typically classified by the vehicle yaw rate gain in (38), which is defined as the response of the vehicle yaw rate with respect to the steering input [81].

$$\left.\frac{r}{\delta_f}\right|_{ss} = \frac{V_x}{L + \dfrac{K_{us}\left(V_x^{\,2} - l_s^{\,2} r^2\right)}{g}} = \frac{V_x}{L - \dfrac{m_v\left(V_x^{\,2} - l_s^{\,2} r^2\right)\left[\left(C_{\alpha fl}^0 + C_{\alpha fr}^0\right) l_f - \left(C_{\alpha rl}^0 + C_{\alpha rr}^0\right) l_r\right]}{gL\left(C_{\alpha fl}^0 + C_{\alpha fr}^0\right)\left(C_{\alpha rl}^0 + C_{\alpha rr}^0\right)}}, \tag{38}$$

where $K_{us} = -\dfrac{m_v\left[\left(C_{\alpha fl}^0 + C_{\alpha fr}^0\right)l_f - \left(C_{\alpha rl}^0 + C_{\alpha rr}^0\right)l_r\right]}{L\left(C_{\alpha fl}^0 + C_{\alpha fr}^0\right)\left(C_{\alpha rl}^0 + C_{\alpha rr}^0\right)}$ is the understeer coefficient. Based on the definition in [81], when the cornering stiffness $C_{\alpha j}^0\left(j = fl, fr, rl, rr\right)$ (the superscript '0' refers to the slope of the tire lateral force curve at 0 slip angle) in (38) are constant, a negative K_{us} denotes the vehicle oversteer condition and a positive K_{us} denotes the vehicle understeer condition [81]. In this paper, instead of using a constant slope to represent the lateral force characteristics, the cornering stiffness $C_{\alpha j}^0$ is redefined and replaced by a function of a varying tire slip angle $C_{\alpha j}\left(\alpha_j\right)$ during the linearization process. Thus, the coefficient K_{us} is extended as a function of tire slip angles $K_{us}^{\alpha}\left(\alpha\right)$, which denotes the vehicle handling stability with respect to different operation points. Note that in [84], similar concepts of local stability and varying stiffness were introduced where the gain response of a steering angle rate with a path curvature was required to be positive. However, the stability criterion in [84] was based on a bicycle model and used to present a handling diagram for one steady state. Compared with the handling diagram, the stability region in this paper contains all the stable vehicle states by analyzing every operation point on the phase plane. Such a stability region representation makes the stability analysis of any given vehicle states a straightforward and intuitive process. Specifically, by directly checking whether the vehicle states are in the defined stability region, the real-time vehicle stability can be determined and applied for control design [85]. Moreover, the stability condition in (36) and (37) are sufficient conditions of (28) in [84].

By replacing the constant $C_{\alpha j}^{0}$ with the varying $C_{\alpha j}\left(\alpha_j\right)\left(j=fl,fr,rl,rr\right)$ in (38), the denominator of (38) is the same as the left side of (24). If (24) is equivalently written as $L+\frac{K_{us}^{\alpha}\left(V_x^{\,2}-l_s^{\,2}r^2\right)}{g}>0$, the unstable vehicle lateral dynamics can be defined as $L+\frac{K_{us}^{\alpha}\left(V_x^{\,2}-l_s^{\,2}r^2\right)}{g}<0$. This inequality condition gives $K_{us}^{\alpha}\left(\alpha\right)<-\frac{gL}{\left(V_x^{\,2}-l_s^{\,2}r^2\right)}<0$, ($V_x>l_s r$ as claimed before), which shows that the derived (unstable) condition is a sufficient condition of a common oversteering definition $K_{us}^{\alpha}<0$ [81]. Therefore, once the vehicle is identified as unstable through (24), the vehicle is already oversteered.

Although a vehicle is typically designed to be a little understeered since oversteering is typically riskier than understeering, a severe understeering will still cause vehicle stability and safety issues [81]. Therefore, inspired by the relationship between the derived stability condition (24) and the oversteering condition (38), an additional understeering condition is proposed to completely describe the vehicle lateral stability region proposed in this paper. One practical criterion applies when

$$\left.\frac{r_o}{\delta_f}\right|_{ss}>\frac{1}{a}\frac{r_{(0,0)}}{\delta_f}, \tag{39}$$

the vehicle is understeered but still considered stable, where a is a constant gain. $\left.\frac{r_o}{\delta_f}\right|_{ss}$ denotes the steady-state yaw rate gain at one operation point (V_{yo}, r_o), and $\frac{r_{(0,0)}}{\delta_f}$ denotes the steady-state yaw rate gain at the origin (0,0), which corresponds to the yaw rate gain at

neutral steering. In other words, for an understeering vehicle, to achieve the same yaw rate response as the neutral steering and still be considered as stable, the steering angle is required to be no larger than a times of that in the neutral steering condition. Otherwise, the vehicle is considered to be operated in a relatively severe understeering condition, which is also defined as unstable in this paper.

Although the vehicle handling stability was also studied in some research for lateral stability region estimation [16][17], it was normally applied as complementary criteria to further limit and reshape the stability regions estimated by the existing methods (e.g. the phase portrait method). However, the local linearization method applied in this paper, by fully considering the vehicle and tire stability and the (stability) relationship between front and rear tires, presents more comprehensive analyses and descriptions of the vehicle stability in terms of the handling properties.

3.2.3. Comparisons with the Phase Portrait Method

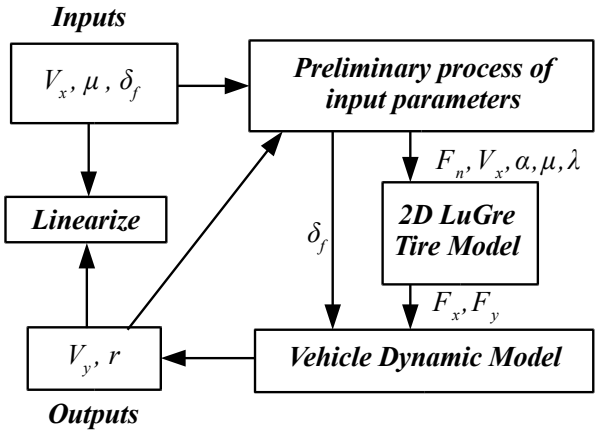

Fig. 6. Diagram of the Stability Region Estimation Process in Matlab-Simulink.

The diagram of the stability region estimation process in Matlab/Simulink is shown in Fig. 6. The system inputs include the vehicle speed, tire-road friction coefficient, and steering angle. First, the system inputs are preliminarily processed based on the basic vehicle parameters and vehicle states to calculate the necessary variables as the inputs of the LuGre tire model and vehicle dynamic model. Specifically, the slip angle α (based on (3)-(6)) and the vertical load F_n (based on (8)-(11)) of each tire are calculated. Tire slip ratios (λ) are set to small numbers (0.001) to describe the pure lateral tire model. Then, based on the tire forces calculated by the tire model, the vehicle states are simulated through the vehicle dynamic model in (1) and (2). In the simulation process, the linearization is executed by implementing the Matlab function "linearize" between the input (δ_f) and the outputs (V_y and r) of the vehicle dynamic system. The linearization process computes the linearized model by numerically perturbing the input and outputs at the selected and discretized operating points. The linearized model is then transferred into a state-space realization, which can be analyzed by the proposed stability criteria in (24). For every discretized operation point on the $V_y - r$ phase plane, the stability of the linearized systems is analyzed. Thus, based on the analysis results, a complete stability region that consists of all the stable operation points can be finally obtained. The following five steps summarize a complete estimation process.

Step 1. A phase plane is discretized (with an interval of 0.1 for both V_y and r), which generates a matrix of evenly distributed operation points.

Step 2. For each operation point, the stability condition (24) is applied, and the stability of this point can be determined.

Step 3. After the stability statuses of all the points on the phase plane are checked, an area that contains all the stable operation points can be depicted. By connecting the outer points of this stable area, the stability region boundaries (blue dot lines in Fig. 8) can be created.

Step 4. Repeat steps 2 and 3 but simply replacing the stability condition (24) with the understeering condition (39) in Section 3.3, the stability region boundaries (black lines in Fig. 8) can be created.

Step 5. Overlay all the boundaries created in steps 3 and 4, a closed stability region is estimated.

Note that the discrete interval can be smaller depending on the required estimation accuracy.

The vehicle parameters specified in Table 2 are taken from a C-Class hatchback model in CarSim database, which is a front wheel drive car with four independent suspensions. Some main parameters of the adopted LuGre tire model ($i = y$ in (7)) are also listed in Table 2.

Table 2. Vehicle and Tire Parameters for Simulations

Symbols	Parameters	Values
m_v	Vehicle mass	1270 kg
g	Gravity constant	9.8 m/s^2
I_z	Yaw moment of inertia	1536.7 $kg{\cdot}m^2$
L	Wheelbase	2.91 m
l_f	Front wheelbase	1.02 m
l_r	Rear wheelbase	1.89 m
l_s	Half of the vehicle track	0.96 m
h_{CG}	Center of gravity height	0.54 m
L_y	Tire model parameter	0.182
ζ_{Ly}	Tire model parameter	0.064
ζ_{Ry}	Tire model parameter	0.091
σ_{2y}	Tire model parameter	0.0069

The phase portrait is a fundamental and direct method to analyze the stability of dynamic systems. In this paper, the vehicle lateral stability region estimated by the phase portrait method is compared with the region estimated by the proposed local linearization method.

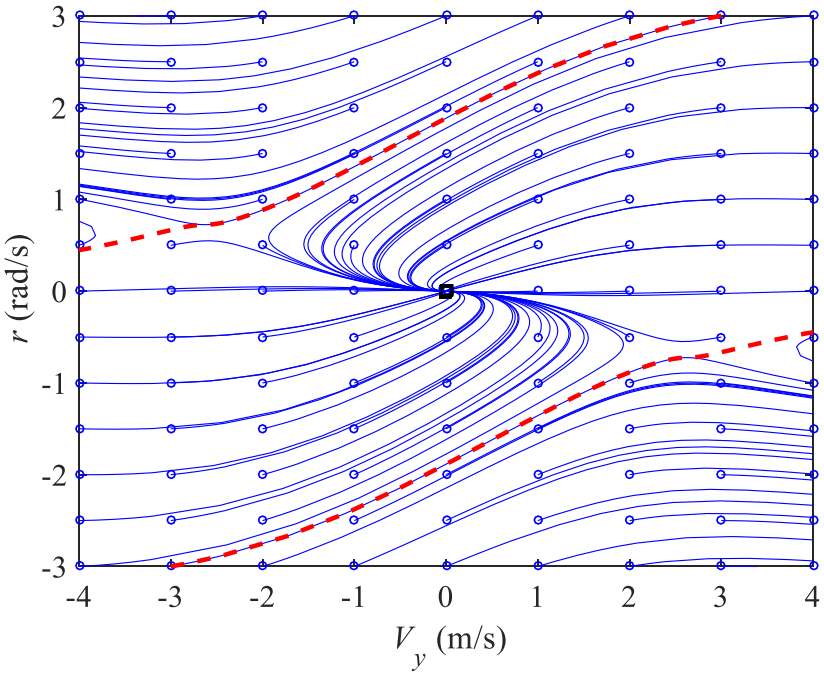

Fig. 7. Vehicle Lateral Stability Region Estimated by the Phase Portrait Method.

The stability region estimated by the phase portrait on the $V_y - r$ phase plane is shown in Fig. 7, where the origin is one equilibrium point and also a stable focus. The estimation condition is set as: the input steering angle is 0 degree, the longitudinal velocity is 25 m/s, and the tire-road friction coefficient μ is 1. Other trajectories, which are not converging to the focus, compose the unstable areas. Thus, the two dash red curves in Fig. 7 define the lower and upper stability boundaries of the vehicle lateral stability region. Note that the phase portrait cannot define the system controllable boundaries since no control effort is applied. The vehicle lateral stability region shown in Fig. 7 is consistent with the results in [9][10].

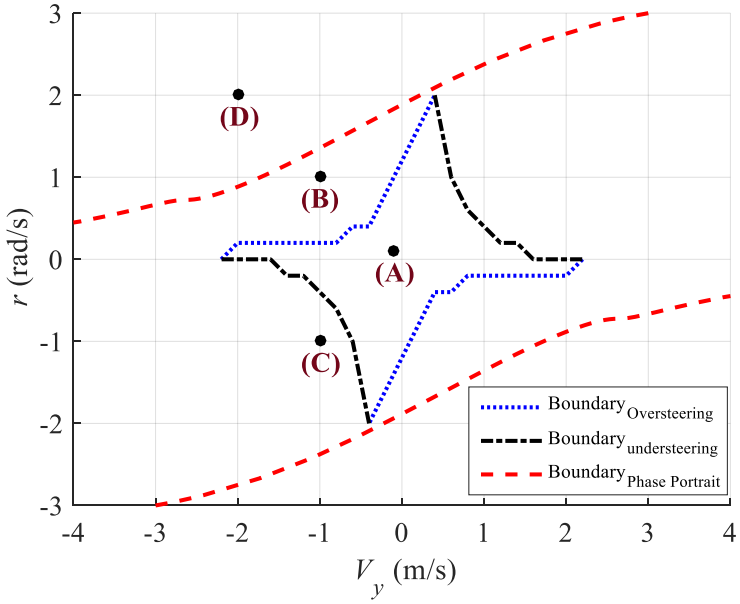

Fig. 8. Comparison of Stability Regions Estimated by the Phase Portrait and the Local Linearization Method.

In Fig. 8, under the same condition, the vehicle lateral stability region estimated by the proposed local linearization method is plotted together with the region estimated by the phase portrait method. As shown in Fig. 8, the red dash lines depict the upper and lower boundaries defined by the phase portrait method. The upper-left and lower-right blue dot curves are the stability boundaries by connecting stable points defined by the criterion (24). The upper-right and lower-left black dash-dot curves are obtained by connecting stable points defined by the understeering criterion discussed in Section 3.3. These four boundaries define the stability region as a closed area. The physical meaning of the obtained stability region is: within the defined stable region, no matter where the vehicle states (operation point) are located, given a disturbance, the vehicle states will return to the operation point that is locally stable. Such a characteristic with respect to the operation

point also describes the vehicle handling stability, which gives the practical meaning of the estimated stability region as, within the stability region, the vehicle trajectories/responses with respect to an input (steering angle) are neither oversteering nor severe understeering.

As observed in Fig. 8, the estimated stability region is much smaller than that obtained from the phase portrait method. Some insights are explained as follows based on the analyses of vehicle state trajectories initiated at four selected conditions: point (A) ($V_y = -0.1m/s, r = 0.1rad/s$) is within the estimated stability region; point (B) ($V_y = -1m/s, r = 1rad/s$) is out of the oversteering boundary but inside the stability region defined by the phase portrait method; point (C) ($V_y = -1m/s, r = -1rad/s$) is out of the understeering boundary but inside the stability region defined by the phase portrait method; point (D) ($V_y = -2m/s, r = 2rad/s$) is out of the stability region defined by both methods.

Initiated at the four different points on the phase plane, the variations of the vehicle lateral velocity, yaw rate, and slip angle on four tires are shown in Fig. 9. The two subplots for point (A) in the first row of Fig. 9 show that both the vehicle states and tire slip angles quickly converge to zero. Since the tire slip angles are small, both the vehicle and tires are stable during the converging process, which shows that both the phase portrait and the local linearization method characterize the consistent stability properties. However, for points (B) and (C), although the vehicle states eventually converge to zero (stable defined by the phase portrait method), the status of some tires (rear tires for (B) and front tires for (C)) are not always stable, especially at the beginning of the converging process. As shown in the second row of Fig. 9 for point (B), in the beginning, the slip angles of rear tires are larger than those of front tires and are also beyond the saturated slip angle (around 10 degrees in

Fig. 2), which indicates that the rear tires are unstable and the vehicle is oversteering. Similarly, as shown in the third row of Fig. 9 for point (C), the slip angles of front tires are larger than those of rear tires and are also beyond the saturated slip angle (around 10 degrees in Fig. 2), which indicates that the front tires are unstable and the vehicle is severely understeering. For point (D), as shown in the last row of Fig. 9, starting in an unstable condition defined by both the phase portrait and the local linearization method, both the vehicle states and tire slip angles become diverging, indicating that the vehicle is unstable.

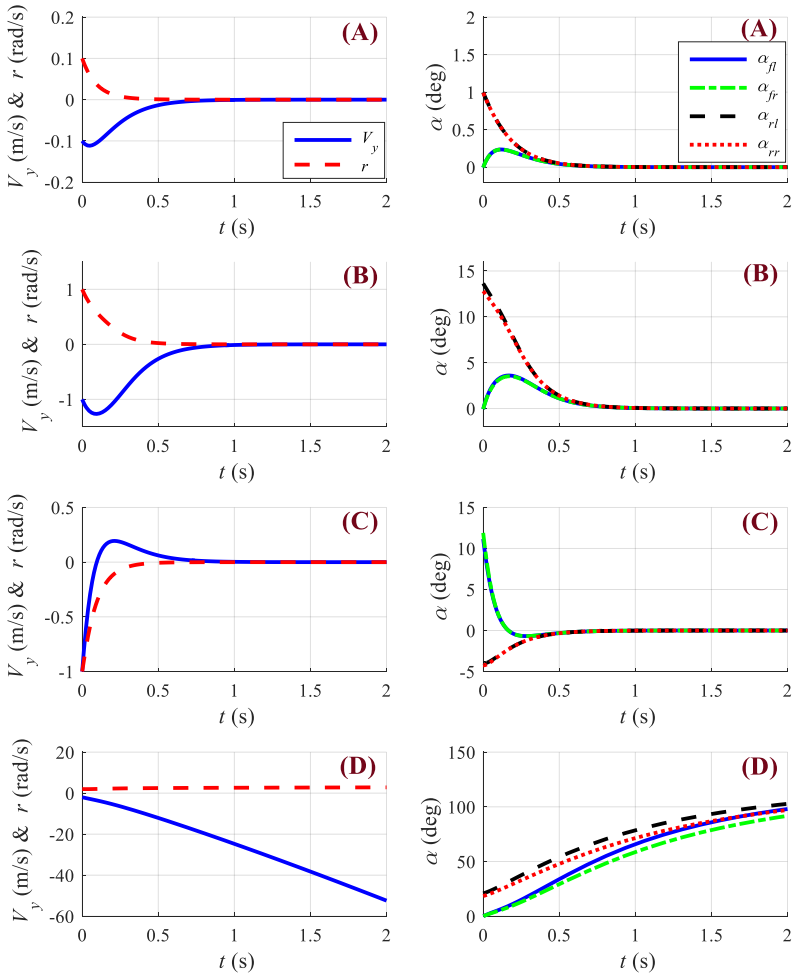

Fig. 9. Variations of Vehicle States and Tire Slip Angles Initiated in Different Conditions.

In summary, the comparisons illustrate that the vehicle lateral stability region estimated by the local linearization method considers both stricter vehicle and tire stability and gives a more conservative estimation, which could be applicable for the control design of AGVs to avoid motion sickness [28][29].

3.2.4. Impact of the Lateral Load Transfer

Different from the applied bicycle model in the literature [14][18][19][83], a four-wheel vehicle model with independently calculated tire slip angles can evaluate the impact of the vehicle lateral load transfer. The tire vertical loads (e.g. (8)-(11)) influence the tire friction forces through the 2D LuGre tire model in (7), and then consequently influence the accuracy of the estimated stability regions. Fig. 10 for the first time quantitatively demonstrates the necessity and improvement to use a four-wheel vehicle model for the lateral stability region estimation, compared with the bicycle model widely used in the literature [14][18][19]. As observed, the estimated stability region using the four-wheel model is bigger (mainly in the yaw rate direction) than that using the bicycle model. Such an observation is explained via two aspects. First, compared with the bicycle model, the calculations of tire slip angles (e.g. (3)-(6)) in the four-wheel vehicle model involve an additional yaw rate term (r) in the denominator, which causes a significant difference between the slip angles of the left and right wheels. Second, when the vehicle is experiencing a certain level of lateral acceleration (even when the steering angle is zero) in a corner, the lateral load transfer distributes more vertical loads to the outer wheels, which consequently generate more friction forces than the inner wheels. The unevenly distributed tire lateral friction forces help the vehicle turns by generating a moment, which

enhances the vehicle yaw stability.

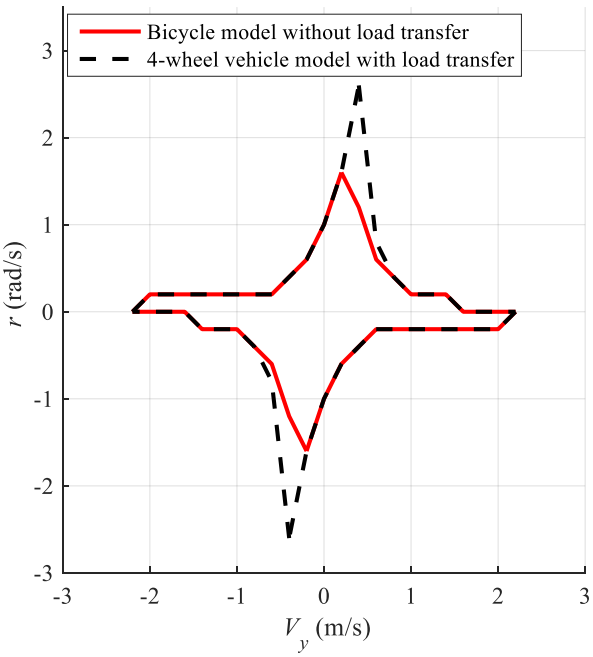

Fig. 10. Comparisons of the Estimated Stability Regions Using a Bicycle Model and a Four-wheel Vehicle Model.

3.2.5. Impact of the Vehicle Longitudinal Velocity

The vehicle longitudinal velocity also has impacts on the estimated lateral stability region. For the demonstration, three longitudinal velocities V_x, namely 10, 20, and 30 m/s, are selected to represent the low, medium, and high speeds driving scenarios, respectively. As shown in Fig. 11, the larger longitudinal velocity, the larger vehicle lateral stability region for the same steering angle δ_f at 0 degree and the tire-road friction coefficient μ at 1. Such an observation can be explained in two aspects. First, based on (3)-(6), for the same V_y and r values, the tire slip angles become smaller when V_x increases. Normally, smaller tire slip angle infers better tire stability, which further

enhances the vehicle lateral stability and results in the graphically enlarged stability regions. Second, let the V_{ymax} and V_{ymin} be the maximum and minimum lateral velocity (actually the extreme velocities in opposite directions) of the estimated stability regions. When V_x increases (10, 20, 30 m/s), the maximum/minimum vehicle side slip angle, $\beta_{max/min} = \tan^{-1}\left(V_{ymax/min} / V_x\right)$, decreases ($\pm 9.9°$, $\pm 6.27°$, $\pm 5.33°$). Therefore, although the stability region becomes larger at a higher longitudinal velocity, the permissible maximum/minimum β decreases, which infers a lower vehicle lateral stability limitation. Moreover, different vehicle longitudinal velocities do not significantly affect the shapes of the stability regions.

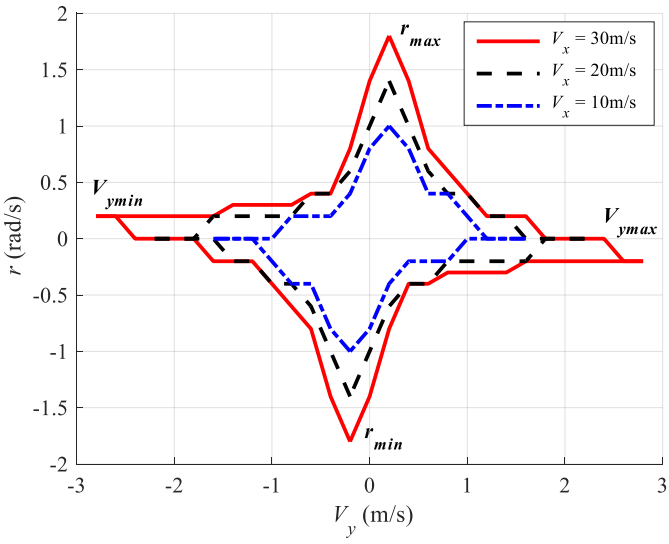

Fig. 11. Impact of the Longitudinal Velocity on the Estimated Lateral Stability Regions.

3.2.6. Impact of the Tire-Road Friction Coefficient

The tire-road friction coefficient directly affects the tire lateral friction forces, thus consequently influencing the estimated stability regions. To demonstrate the impact of tire-

road friction coefficient, three different μ values ($\mu = 1, 0.7, 0.3$) which represent the high, medium, and low friction roads are selected, respectively. In Fig. 12, the stability region becomes smaller as μ decreases for the same vehicle longitudinal velocity V_x at 25 m/s and the steering angle δ_f at 0 degree. This trend is reasonable because the vehicle lateral motion can be hardly controlled and stabilized due to the lack of friction forces on low μ roads. Moreover, the shape of the stability regions under different μ values are similar. In addition to tire-road friction coefficient, other tire parameters can change and introduce tire characteristic differences among four tires, which can also influence vehicle handling characteristics.

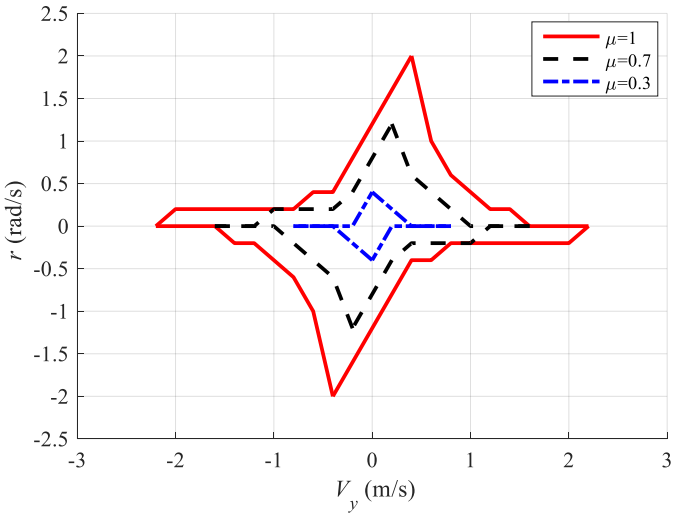

Fig. 12. Impact of the Tire-road Friction Coefficient on the Estimated Lateral Stability Regions.

3.2.7. Impact of the Front Wheel Steering Angle

To demonstrate the impact of the front wheel steering angle on the estimated lateral

stability region, three front wheel steering angles ($\delta_f = -4, 0, 4$ degrees) are applied to the vehicle model. As observed in Fig. 13, the lateral stability region shifts from the lower left to the upper right as the steering angle changes from -4 to 4 degrees for the same V_x at 25m/s and the same μ at 1. Moreover, the shape and size of the stability region do not change much in the shifting process. Note that if the steering angle exceeds a certain value, the "bifurcation" phenomenon could happen [10], which infers that the system equilibrium point is located out of the estimated stability region on the phase plane. As observed in Fig. 13, the system equilibrium points (*) (calculated by setting both $\dot{V}_y$ and $\dot{r}$ in (1) and (2) to zero) has the trend of becoming unstable (move towards the stability region boundary) when the steering angle (either -4 or 4 degrees) is applied, which is consistent with the observations in literature [10].

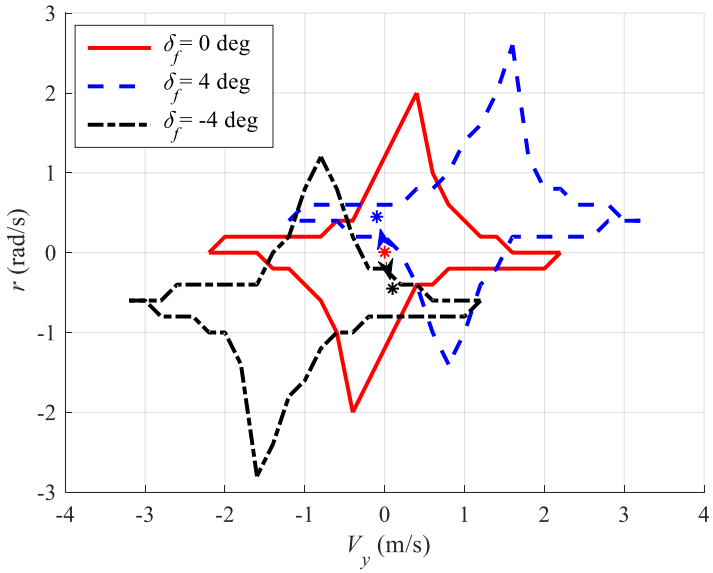

Fig. 13. Impact of the Steering Angle on the Estimated Lateral Stability Regions.

In sum, four different impacts are discussed and analyzed in Section 3.2.7. These

analyses and observations on the variation of the estimated stability region are either consistent with the discussions of other lateral stability regions, such as with respect to μ and δ_f [12][18]-[21], or newly discovered and explained, such as with respect to the four wheel vehicle model and V_x [19]-[21]. These impact analyses show the correctness and contributions of the estimated stability regions.

3.2.8. A Case Study by Matlab/Simulink and CarSim® Co-Simulation

To further validate the estimated stability regions and above discussions, a case study of a high-speed double J-turn maneuver is conducted in the Matlab/Simulink and CarSim co-simulation environment. The vehicle longitudinal velocity is set constant at 90 km/h (25 m/s) and the tire-road friction coefficient μ is set to 0.85. The steering angle input during the maneuver for 20 seconds is shown in Fig. 14. Based on the discussions in Section 3.2.7, the stability region shifts when the steering angle changes. Therefore, without loss of generality, the vehicle state trajectory between 2.5-7.5s and 12.5-17.5s (when the steering angle reaches steady-state values) are used for analysis.

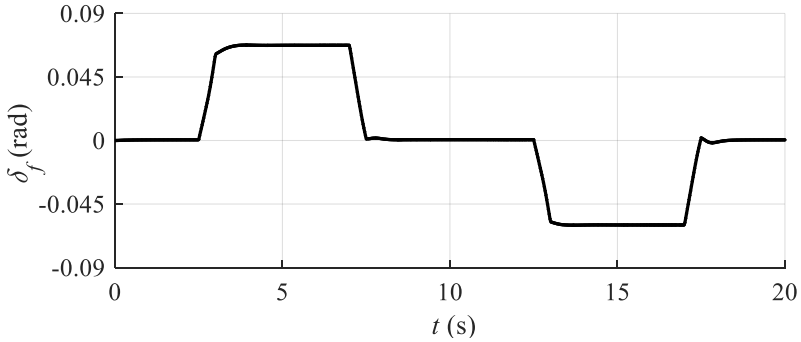

Fig. 14. Front Wheel Steer Angle Input for a High-speed Double J-turn Maneuver.

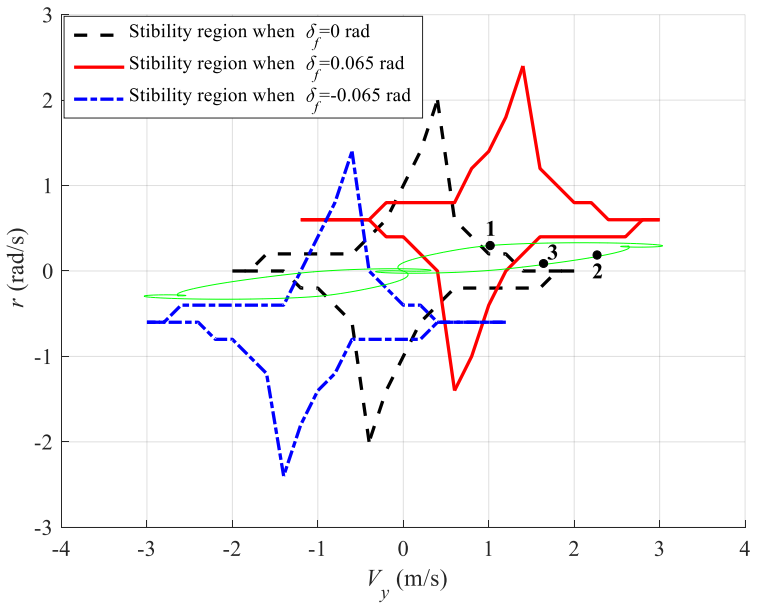

Fig. 15. Vehicle State Trajectory and the Estimated Stability Regions on the $V_y - r$ Phase Plane.

In Fig. 15, the vehicle state trajectory is overlaid with the estimated stability regions. The black dash region represents the estimated stability region when the steering angle is 0 degrees. The areas bounded by the solid red line and dash-dot blue line represent the newly estimated stability regions when the steering angle is 0.065 *rad* and -0.065 *rad*, respectively. The solid green curve represents the vehicle state trajectory of the double J-turn maneuver from CarSim®, where the right half part (with respect to the origin) is mainly the vehicle state trajectory during the first 10 seconds and the left half part is mainly the trajectory during the second 10 seconds. As shown in Fig. 15, the vehicle state trajectory is partially outside the estimated stability boundary during the maneuver, especially on the farther right/left end of the trajectory no matter how the region shifts for such a high-speed J-turn maneuver.

Considering the symmetric property of the stability regions and vehicle state trajectory with respect to the origin in Fig. 15, three data points on the right half trajectory between 2.5 to 7.5 seconds are selected as examples to analyze vehicle stability. Since the steering angle is constant during this period, the stability region defined by the red solid line should be applied for analysis. As observed in Fig. 15, point 1 is in the region while point 2 and 3 are out of the region. The stabilities of these vehicle states points are verified by checking the signs of eigenvalues of the corresponding A_o matrix. As shown in Table 3, the eigenvalues (λ_1 and λ_2) of A_o at point 2 and 3 both have positive real values (unstable) while the eigenvalues of A_o at point 1 are both negative (stable). Therefore, only the A_o at point 1 is Hurwitz and the vehicle states on point 1 is stable.

By checking the steady-state yaw rate response $r_o / \delta_f \big|_{ss}$, the stabilities of these three state points are further analyzed. In Table 3, the $r_o / \delta_f \big|_{ss}$ at point 1 is greater than one third (select $a = 1/3$ based on an empirical value of the yaw rate gain response for understeering [81]) of the neutral steering response ($\frac{1}{3}\frac{r_{(0,0)}}{\delta_f} = \frac{2.739}{3} = 0.913, \text{when} \delta_f = 0.065\text{rad}$) but is still smaller than $\frac{r_{(0,0)}}{\delta_f} = 2.739$. Namely, the vehicle status at point 1 is a little understeering but still in the stable range. However, the $r_o / \delta_f \big|_{ss}$ at point 2 and 3 are both larger than $\frac{r_{(0,0)}}{\delta_f}$, which imply oversteering based on the yaw rate response curve in [81]. The

oversteering characteristics at point 2 and 3 can also be verified by the negative sign of K_{us}^{α}.

Table 3. Simulation Results Analysis

No.	time	V_y (m/s)	r (rad/s)	Stability	λ_1	λ_2	$r_o / \delta_f\big\|_{ss}$	K_{us}^{α}	status
1	3	1.0	0.23	stable	-1.68	-5.98	2.42	0.01	Understeer
2	5	2.3	0.18	unstable	4.46	-11.67	6.73	-0.43	Oversteer
3	7.5	1.6	0.07	unstable	3.08	-14.21	3.8	-0.13	Oversteer

3.3. Conclusions

A new vehicle lateral stability region estimation method, which utilizes a local linearization method based on a four-wheel vehicle model and a nonlinear 2D LuGre tire model, is presented in this chapter. The estimated vehicle lateral stability regions are more conservative compared with the regions estimated by the phase portrait and Lyapunov method in the previous studies. The conservation is mainly featured from the stricter and simultaneously applied vehicle and tire stability criteria, which are mathematically derived by using the applied local linearization method. Moreover, simulation results show that the lateral load transfer, vehicle longitudinal velocity, tire-road friction coefficient, and steering angle all have impacts on the estimated vehicle lateral stability regions. The estimated stability regions are validated through a high-speed double J-turn maneuver in the co-simulation environment of Matlab/Simulink and high-fidelity CarSim. The estimated conservative lateral stability region has the potential to be used for vehicle lateral stability control of automated vehicles.

CHAPTER 4

REGION-BASED VEHICLE LATERAL STABILITY CONTROL

Based on the estimated vehicle lateral driving stability regions in Chapter 3, a series of vehicle lateral stability controllers were designed. In this chapter, two sliding mode control methods and one non-overshooting model predictive control are introduced. The main contents in sections 4.2 and 4.3 were presented in the author's previous publication [96], while the main contents in section 4.4 were presented in the author's previous publication [90] [4].

4.1. Overview

Among various vehicle stability control methods, such as reference tracking [98]-[100], traction control [101], and electronic stability control [102], the stability region-based control is regarded as an intuitive and efficient approach [17] and thus was widely studied in the past decades. Generally, the region-based stability control typically intervenes when a vehicle is about to lose stability, which is indicated by vehicle states approaching the region boundaries. Therefore, the region-based control is feasible to be either applied individually or integrated with additional (performance) control purposes. To achieve region-based control, different vehicle lateral stability regions were defined or estimated and various vehicle lateral stability control methods were proposed correspondingly [9]-[21][30]-[37].

[4] The cited contents in section 4.2 and 4.3 are with permission of Copyright © 2021 IEEE, to be reprinted from [Huang and Chen, *IEEE Transactions on Vehicular Technology*, 2021]. The cited contents in section 4.4 are with permission of Copyright © 2019 IEEE, to be reprinted from [Huang and Chen, in *Proceedings of American Control Conference*, 2019].

Although different region-based stability control methods based on related stability regions were discussed, three main issues still need to be further investigated and resolved in terms of effective and robust control. First, the stability regions were typically simplified in regular shapes with straight-line boundaries for vehicle stability analysis and the corresponding control design. Consequently, the stability analysis and control results may not be accurate and effective, especially in the applications of AGVs. Second, the position of applied stability regions in the literature were all fixed, which did not correctly describe features of stability regions for control design. The locations of (different) stability regions on (the corresponding) phase planes were found to be shiftable with respect to a steering angle significantly. Hence, the stability regions used for control should be described as varying or shifting areas with respect to a steering angle. In the literature, one possible reason for using the fixed regions is that the quantitative or explicit relationship between the shifting stability regions and the steering angle was not determined, although the trend was identified through simulation results. Third, the vehicle state trajectories were not guaranteed to be controlled in the stability regions. Namely, although the vehicle state trajectories were controlled back to the stability regions, the control signals or actions were only triggered after the vehicle states left the regions, which have already introduced (slightly or temporarily) unstable vehicle statuses. For AGVs, even slightly or temporarily unstable vehicle statuses can significantly affect vehicle safety, which makes the problem of stability-guaranteed control necessary and important.

The aforementioned issues were addressed in the author's previous studies [87]-[90], whose major contributions are introduced in this chapter. Specifically, in section 4.2, based

on the estimated stability region, a novel analysis method of vehicle stability statuses by using the projection method is proposed. The shifting vector and dynamic margin of the stability region are integrated into the projection method. As the result, an effective and robust region-based stability analysis is developed. In section 4.3, based on the stability analysis, dynamic SMC designs using the dynamic margin as the sliding surface are presented. The dynamic SMC designs are separately applied to two control configurations, namely active front wheel steering (AFS) + direct yaw moment control (DYC) and active front wheel steering (AFS) + active rear wheel steering (ARS). In section 4.4, without the chattering issues in SMCs, a non-overshooting model predictive control algorithm is presented.

4.2. Shifting Function and Dynamic Margin

4.2.1. Shiftable Stability Regions

Since a varying steering angle is common in vehicle lateral motions and closely related to lateral stability regions, the explicit relationship between the stability region variation and the steering angle needs to be developed. In literature, the varying trend of (various) stability regions with respect to the steering angle was usually discussed based on the baseline region when $\delta_f = 0$ through simulation results [9][10]. However, the quantitative relationship between the movement of stability regions and the steering angle is not developed yet.

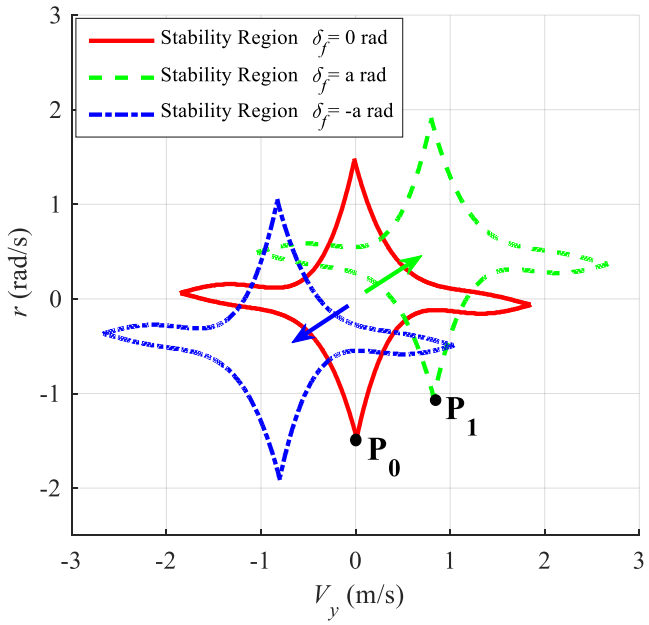

Fig. 16. The Shifting Feature of Vehicle Lateral Stability Regions.

The estimation process of stability regions for continuously varying steering angles is complex and may not be real-time implementable. Even if lookup tables could be created offline for different (discrete) steering angles, the calibrations and storage memories could also face other challenges. Thus, an explicit and simple relationship between the baseline stability region ($\delta_f = 0$) and the varying steering angle will benefit practical applications. To achieve this goal, the shifting feature of the stability region is described in Fig. 16. When the steering angle changes, the stability region shifts along a specific direction with a similar size and shape [94]. Therefore, as long as a proper shifting vector is formulated, without re-estimation, the varying stability region at any steering angle can be obtained by applying the shifting vector to the boundary functions of the baseline region at $\delta_f = 0$. The shifting vector is derived as follows.

Since the stability region adopted in this paper is related to vehicle handling stability, it is applicable to discuss the shifting feature based on tire statuses. In Fig. 16, the tire status at P_0 and P_1 are analyzed as a typical example because P_0 (P_1) is the lowest point of the corresponding stability region for $\delta_f = 0$ ($\delta_f = a$ rad). At $P_0\left(V_{y0}, r_0\right)$, the corresponding calculations of the front and rear tire slip angles with $\delta_f = 0$ are shown in (40) and (41). Similarly, the front and rear slip angles at $P_1\left(V_{y1}, r_1\right)$ with $\delta_f = a$ are calculated in (42) and (43).

$$\begin{cases} \alpha_{f0} = -\dfrac{V_{y0} + l_f r_0}{V_x} & (40) \\ \alpha_{r0} = -\dfrac{V_{y0} - l_r r_0}{V_x} & (41) \end{cases},$$

$$\begin{cases} \alpha_{f1} = a - \dfrac{V_{y1} + l_f r_1}{V_x} & (42) \\ \alpha_{r1} = -\dfrac{V_{y1} - l_r r_1}{V_x} & (43) \end{cases}.$$

Based on the calculations in (40)-(43), the tire slip angles at P_0 and P_1 are found to satisfy the following relationship: $\alpha_{f0} \approx \alpha_{f1}$, $\alpha_{r0} \approx \alpha_{r1}$, and the slip angle differences (in absolute values) are less than 0.1% of the initial slip angles (α_{f0} and α_{r0}) (as shown in Table 4). Therefore, the slip angles at P_0 and P_1 can be assumed to be the same. By checking the whole stability region, the discovered relationship between P_0 and P_1 is not unique. Specifically, for all the points on the stability region boundaries for the case of $\delta_f = 0$, the corresponding points that have the same relative location on the shifted boundary for the case of $\delta_f = a$ can be found. Then, the same slip angle calculations in (40)-(43) are applied

to these pairs of points. The statistical analyses about the slip angle difference for all the pairs of points are shown in Table 4, where $\Delta\alpha_f = \alpha_{f0} - \alpha_{f1}$ and $\Delta\alpha_r = \alpha_{r0} - \alpha_{r1}$.

Table 4. Statistical Analysis of the Slip Angle Difference

Slip angle difference (rad) & percentage to $\alpha_{f/r0}$	$\Delta\alpha_f$	$\frac{\Delta\alpha_f}{\alpha_{f0}}(\%)$	$\Delta\alpha_r$	$\frac{\Delta\alpha_r}{\alpha_{r0}}(\%)$
Maximum value	8.3×10^{-3}	9×10^{-2}	1.1×10^{-16}	6.9×10^{-10}
Minimum value	8.3×10^{-5}	7×10^{-3}	0	0
Mean value	1.4×10^{-3}	1×10^{-2}	7.6×10^{-18}	6.2×10^{-12}
Variance value	3×10^{-12}	5.1×10^{-6}	8.2×10^{-69}	1.8×10^{-36}

The results shown in Table 4 are able to prove that $\alpha_{f0} = \alpha_{f1}$ and $\alpha_{r0} = \alpha_{r1}$ are valid for each pair of points since $\Delta\alpha_f$ and $\Delta\alpha_r$ are both small enough. Thus, by applying such a relationship to (40)-(43), for any point (V_{y0}, r_0) on the stability region boundary for $\delta_f = 0$, the corresponding point (V_{y1}, r_1) on the shifted stability region boundary can be determined as

$$\begin{cases} V_{y1} = V_{y0} + \dfrac{V_x l_r \delta_f}{l_f + l_r} & (44) \\ r_1 = r_0 + \dfrac{V_x \delta_f}{l_f + l_r} & (45) \end{cases}.$$

The relationships in (44) and (45) define a shifting vector in the $\begin{bmatrix} V_y & r \end{bmatrix}^T$ direction as a function of the steering angle δ_f, where the V_{y0} and r_0 are any point on the stability region boundary for $\delta_f = 0$. Such a shifting vector can be easily applied to calculate the explicit functions of shifting stability boundaries. In [86], the shifting analysis was

extended with the consideration of rear wheel steering angles. Based on the four boundary functions shown in Fig. 18 ($\delta_f = 0$, $\delta_r = 0$), with any steering angle δ_f and δ_r, the four new boundary functions are expressed as

$$\begin{cases} b_1 = f_1(V_y - S_{V_y}, r - S_r) \\ b_2 = f_2(V_y - S_{V_y}, r - S_r) \\ b_3 = f_3(V_y - S_{V_y}, r - S_r) \\ b_4 = f_4(V_y - S_{V_y}, r - S_r) \end{cases}, \tag{46}$$

where $S_{V_y} = \dfrac{V_x\left(l_r\delta_f + l_f\delta_r\right)}{l_f + l_r}$ and $S_r = \dfrac{V_x\left(\delta_f - \delta_r\right)}{l_f + l_r}$ are the length of the shifting vector in the V_y and r directions, respectively.

Remark 3. The lateral load transfer, which causes asymmetric vertical loads on left and right tires, has been considered in the shiftable stability regions by adopting the double-track vehicle model in section 2. The shifting properties for other asymmetric conditions, such as split μ for left and right tires, need to be discussed based on re-estimated stability regions from the authors' previous work [94], which will be discussed in future work.

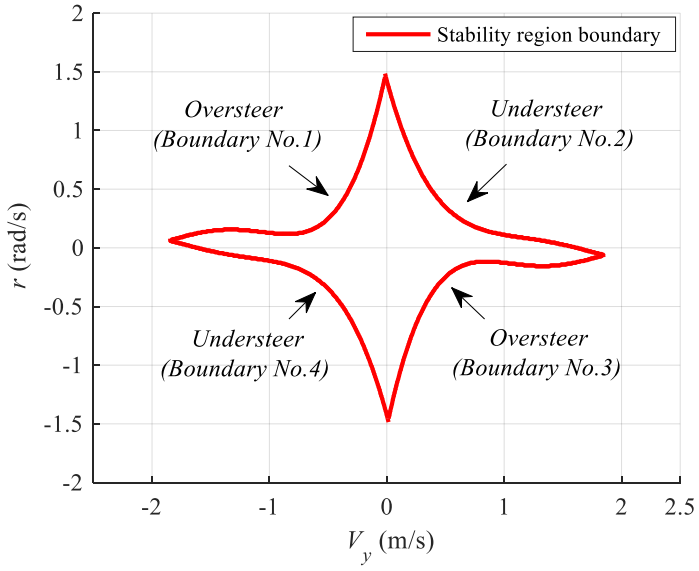

Fig. 17. A Vehicle Lateral Stability Region Estimated in [94].

In the authors' previous work [94], a novel vehicle lateral stability region was estimated, which is used to analyze vehicle lateral stability and design the corresponding stability control. Note that other stability regions could be also applied without influencing the following process and contributions on the stability analysis and control design in this paper.

The lateral stability region shown in Fig. 17 is estimated by a local linearization method, where the stability criteria are formulated with a comprehensive and practical understanding of vehicle handling stability and tire stability. Due to this reason, the estimated stability regions are more conservative than other stability regions. However, this does not necessarily limit the vehicle driving performance. As shown in Fig. 17, under the conditions of $V_x = 25m/s$, $\mu = 0.75$, and $\delta_f = 0$ deg, a vehicle lateral stability region is shown by a closed irregular shape on the $V_y - r$ phase plane. The stability region in Fig.

17 typically consists of four boundaries, where two are defined as oversteering boundaries and the other two are defined as understeering boundaries.

Given the stability region in Fig. 17, the vehicle lateral stability status can be analyzed by checking the relative distance between the vehicle state point (V_y, r) and the region boundaries. If the stability boundaries were simplified, (e.g., as straight lines [14][36]), the relative location could be easily determined. However, since the stability boundaries of the region in Fig. 17 are irregular, the existing analysis methods are not applicable. To address this issue, a projection method is proposed to achieve two main purposes for stability analysis.

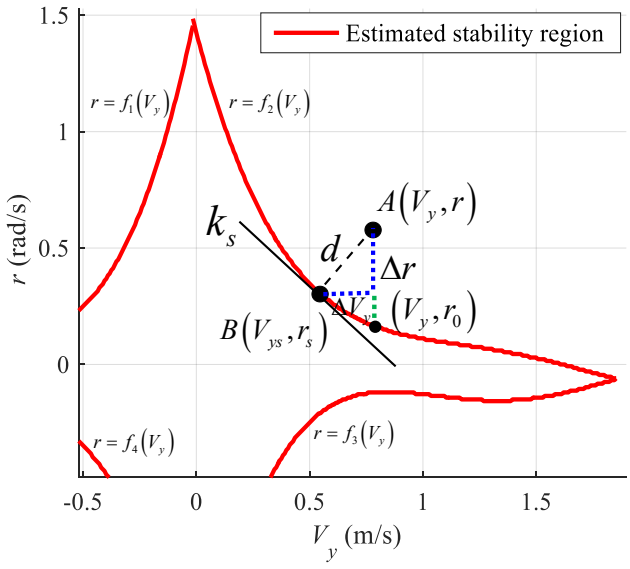

Fig. 18. Projection Method and the Closest Point on the Boundary.

The first purpose of the projection method is to determine the closest point on the stability boundaries that has the minimum distance to the vehicle state point. As shown in Fig. 18, the stability region boundaries can be formulated as four polynomial functions $r = f_j(V_y)$, $j = 1,2,3,4$. For one vehicle state point $A(V_y, r)$ located inside or outside of

the stability region, there exists a point $B\left(V_{ys}, r_s\right)$ on the boundaries, which has the minimum distance to point *A*. Point *B* can be determined by the projection method, which indicates that if $B\left(V_{ys}, r_s\right)$ is the projection of $A\left(V_y, r\right)$ on the boundary, the connection between *A* and *B* is orthogonal to the tangent (k_s) of the function $f_j\left(V_y\right)$ at *B*. The slope of *AB*, k_{AB}, therefore has the following relationship with the tangent k_s.

$$k_{AB} \cdot k_s = -1, \tag{47}$$

where $k_{AB} = \dfrac{V_y - V_{ys}}{r - r_s}$ and $k_s = f_j'\left(V_{ys}\right)$. Then, (47) can be further written in (48) by substituting k_{AB}, k_s, and the boundary function $r = f_j\left(V_y\right)$.

$$\frac{V_y - V_{ys}}{r - f\left(V_{ys}\right)} f_j'\left(V_{ys}\right) = -1 \ . \tag{48}$$

By numerically calculating the roots of (48) in the searching range, defined by the boundary length, the V_{ys} and the corresponding r_s can be obtained. Finally, with all the required values, the distance between point *A* and *B* is given by

$$d = \sqrt{\left(V_y - V_{ys}\right)^2 + \left(r - r_s\right)^2} \ . \tag{49}$$

For any vehicle state point, the above calculation (47)-(49) regarding all the four boundary functions are applied. By comparison, the shortest distance and the closest point on the stability region boundaries can be determined.

Remark 4. Theoretically, for each boundary function $r = f_j\left(V_y\right)$, $j = 1,2,3,4$, a unique solution (point) can be ensured since the boundary functions are convex (with respect to

the inside area). Practically, if multiple points (solutions) on one boundary are found due to insufficient calculation accuracy, the point that has the minimum distance to the center of the region is selected as the unique point. From the region-based control point of view, a shorter distance to the region center normally infers a more stable status, which is better to be maintained. If multiple solutions are obtained for the four boundaries (multiple points from different boundaries have the same minimum distance), the same idea used for the single boundary is applied again to select the unique point.

The second purpose is to determine the vehicle stability status (whether the vehicle state is in the stability region or not). As shown in Fig. 18, based on the analysis results from the projection method, the number of the closest boundary (j) to point A can be obtained. Then, by substituting V_y at the current vehicle state point A into the corresponding boundary function, the yaw rate value r_0 is calculated as $r_0 = f_j(V_y)$. Note that the point (V_y, r_0) is on the boundary. For example, as shown in Fig. 18, the second boundary $(j = 2)$ is detected as the closest boundary to point A, $r_0 = f_2(V_y)$. Therefore, if $r > r_0$, A is out of the region; if $r < r_0$, A is within the region; if $r = r_0$, A is on the region boundary. The determination algorithm of vehicle stability status for each boundary is summarized in Table 5. If the vehicle status is unstable (out), the state differences (as ΔV_y and Δr in Fig. 18) are fed back to the controller as the control error signals.

Table 5. Determination of Vehicle Stability Status

Boundary No. 1&2	If $r > r_0$	Unstable (out)
	If $r < r_0$	Stable (in)
Boundary No. 3&4	If $r < r_0$	Unstable (out)
	If $r > r_0$	Stable (in)

Note: (in/out) = (vehicle state point is in/out of the region).

Remark 5. To handle estimation errors of vehicle states, a worst-case measurement/observation scenario is assumed and involved in the vehicle stability analyzing process, which largely increases the robustness of analysis [89]. To tackle the uncertainties in tire-road friction coefficient estimation, a robust scale coefficient (normally ≤ 1), which makes the region smaller and more conservative, is applied [89]. Meanwhile, the size of the estimated stability region is adaptive to the change of friction coefficient.

4.2.2. Dynamic Margin of the Stability Region

In the literature, the region-based vehicle stability control was only activated after the vehicle state trajectory penetrates the boundary [17][30]. Therefore, the vehicle state trajectories were inevitably out of stability regions for a short time and then controlled back to the regions. To avoid the undesired vehicle control phenomena, a dynamic margin of the stability region, which aims at activating the controller before the vehicle state trajectory across the stability region boundary, is designed.

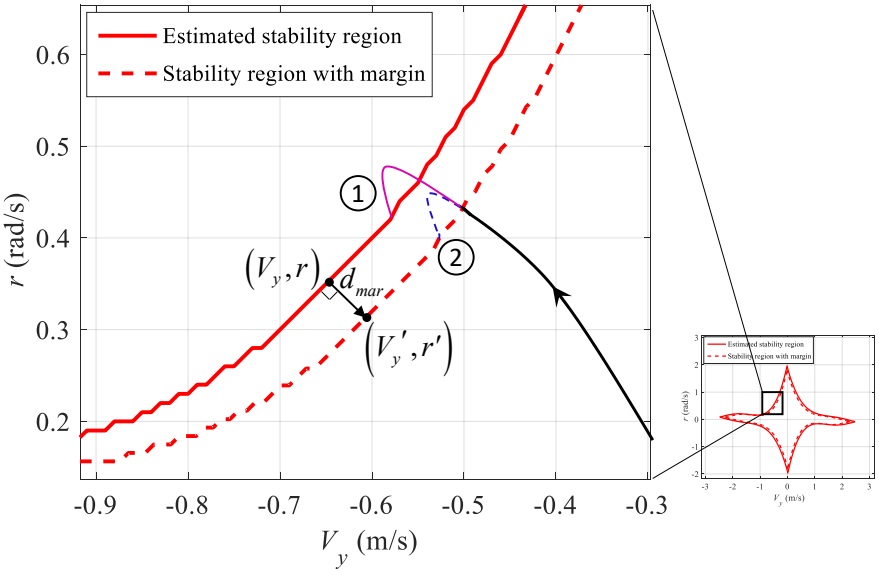

Fig. 19. A Comparison Between Controlled Vehicle State Trajectories Based on ① Stability Region, ② Stability Region with a Margin.

As shown in Fig. 19, as the vehicle state trajectory approaches the stability region boundary, if the stability controller is activated based on the actual stability boundaries (case ①), the vehicle state trajectory will be partially out of the region. On the other hand, if the controller is actuated based on the stability boundaries with a margin (case ②), the vehicle state trajectory could be completely contained in the stability region without any unstable risks. The essential difference between case ① and case ② is the different control activation timings, which are determined by the relative locations between the vehicle state trajectory and the stability boundaries. Although a margin design inward of the stability boundaries can guarantee that the state trajectory will never cross the boundary, a conservative margin, which activates the stability control too early, may cause conservative vehicle dynamic performance. Thus, neither unstable vehicle status nor conservative

vehicle performance is desired. Therefore, a proper margin that can balance the two requirements is necessary. To address this issue, a dynamic margin of the stability region is designed as follows.

The dynamic margin is defined as a vector, which is pointing inward and perpendicular to the stability region boundaries. The length of the margin vector is calculated dynamically as the distance that the vehicle state trajectory travels on the phase plane over at least one sampling time. The calculation of the length of the margin d_{mar} is shown in (50).

$$d_{mar} = \sqrt{\Delta V_y{}^2 + \Delta r^2} = \sqrt{\left(n\Delta t\dot{V}_y\right)^2 + \left(n\Delta t\dot{r}\right)^2}, n \geq 1, \tag{50}$$

where n is the number of sampling time. By substituting the vehicle dynamics in (1) and (2) with zero control inputs into (50), the stability margin is then formulated as a nonlinear function of the vehicle lateral velocity, yaw rate, longitudinal velocity, and tire-road friction coefficient as

$$d_{mar} = f\left(V_y, r, V_x, \mu\right), \tag{51}$$

where μ in (51) is can be explicitly expressed after substituting (7) into (1) and (2). Note that the values of V_y and r in the stability margin (51) are selected at the points on the stability region boundaries. In the vehicle stability analysis, for any measured (V_y, r), the closest point (V_{ys}, r_s) to (V_y, r) can be found on the boundaries. By substituting (V_{ys}, r_s) to (51), the corresponding margin d is calculated, which dynamically changes as the values of (V_{ys}, r_s) change. As shown in Fig. 19, with the proposed dynamic margin, the dashed curves depict a smaller stability region. For each point on the original boundaries, a

corresponding new point (V_y', r') can be determined by applying the margin d_{mar} inwards. All the new points compose the boundaries of the stability region with margin.

Using the dynamic margin as a new reference, which can be understood as a shrank stability region, the projection method and the formulated shifting vector can be correspondingly applied to develop a complete stability analysis tool, with the procedure described in the following Algorithm 1.

Algorithm 1. Region-based Vehicle Lateral Stability Analysis

Specify boundary functions and shifting vector (S) for the originally estimated vehicle lateral stability region.

for each (V_y, r) and δ_f measured in real-time do

apply the dynamic margin (d_{mar}) and S to the boundary functions and calculate $\left(V_{ys}, r_s\right)$ by the projection method;

if status = 'unstable' by Table 5 then

return $V_{ys}, r_s, \dot{V}_{ys}, \dot{r}_s$ to the controller;

end if status = 'stable' by Table 5

end for

return status and $V_{ys}, r_s, \dot{V}_{ys}, \dot{r}_s$.

4.3. Dynamic Sliding Mode Control

Based on the stability analysis results from Algorithm 1, dynamic SMCs are designed to keep the vehicle state trajectory always stay in the stability region. Although SMC is an effective method to handle robust control problems, the chattering (discontinuity) issue in

control signals always prevents its applications [105]. To address this issue, dynamic SMC was proposed, where the chattering only happens in the control derivative [106]. In this dissertation, instead of using a standard SMC, dynamic SMCs are adopted to reduce chattering in control signals. In this section, two different dynamic SMCs are designed for AFS + DYC and AFS +ARS respectively.

4.3.1. AFS and DYC

4.3.1.1.Controller Design

The proposed stability control is realized via an integrated AFS and DYC design, which overcomes some limitations of separate AFS and DYC methods. Specifically, when the only AFS is applied, due to the sensitivity of the estimated stability region with respect to the steering angle, bifurcation phenomena could happen for a large steering angle (mainly caused by nonlinear tire forces). Therefore, the control effects of the AFS method could be significantly limited. To overcome such a limitation, the DYC method is integrated since the DYC (compared with AFS) does not have direct impacts on tire steering and slip angles by only applying longitudinal driving/braking forces. With the integrated AFS and DYC method, the requirements of the control efforts on both methods can be largely reduced, which makes the proposed dynamic SMC control design more feasible for practical applications. Note that if not specified, all the stability regions in the following contents are the stability regions with the proposed margin. The details of the proposed sliding mode control are described as follows.

First, if the vehicle state trajectory is within the stability region, no control will be applied. Second, when the state trajectory approaches the stability margin, the stability

control will be activated. In this case, the vehicle state trajectory will be controlled to slide on the stability margin boundaries until the trajectory moves inward from the boundaries. Thus, the sliding surfaces are selected as

$$S=\begin{bmatrix} s_1 \\ s_2 \end{bmatrix}=\begin{bmatrix} \dot{V}_y-\dot{V}_{ys}+\lambda_1\left(V_y-V_{ys}\right) \\ \dot{r}-\dot{r}_s+\lambda_2\left(r-r_s\right) \end{bmatrix}, \tag{52}$$

where s_1 and s_2 are the dynamic sliding surfaces with respect to the errors of the states ($\Delta V_y=V_y-V_{ys}$ and $\Delta r=r-r_s$) given by the projection method. λ_1 and λ_2 are positive constants. The reaching condition of the sliding surface is $S=\bar{0}$ $\left(s_1=0,s_2=0\right)$.

Proposition 1. The control law in (53) ensures that the reaching condition of the sliding surface is satisfied.

$$\begin{cases} F_{yAFS}=\left[\dot{V}_{ys}-\lambda_1\left(V_y-V_{ys}\right)-K_1\int sign(s_1)dt+V_x r\right]m_v \\ \qquad -\left[\left(F_{yfl}+F_{yfr}\right)\cos\delta_f+F_{yrl}+F_{yrr}\right] \\ M_{DYC}=\left[\dot{r}_s-\lambda_2\left(r-r_s\right)-K_2\int sign(s_2)dt\right]I_z \\ \qquad -\left\{l_f\left[\left(F_{yfl}+F_{yfr}\right)\cos\delta_f+F_{yAFS}\right]\right. \\ \qquad \left.-l_r\left(F_{yrl}+F_{yrr}\right)+l_s\left(F_{yfl}-F_{yfr}\right)\sin\delta_f\right\} \end{cases}, \tag{53}$$

where F_{yAFS} and M_{DYC} are the lateral force and yaw moment generated by AFS and DYC respectively.

The proof of Proposition 1 is given as follows.

Proof. Defining a Lyapunov function as $V=S^TS/2$. Then, the derivative of V is written as

$$\dot{V} = s_1\dot{s}_1 + s_2\dot{s}_2 = s_1\left[\ddot{V}_y - \ddot{V}_{ys} + \lambda_1\left(\dot{V}_y - \dot{V}_{ys}\right)\right] + s_2\left[\ddot{r} - \ddot{r}_s + \lambda_2\left(\dot{r} - \dot{r}_s\right)\right] \quad (54)$$

Substituting (53) into (1) and (2),

$$\begin{cases} \dot{V}_y = -K_1\int sign(s_1)dt + d_1/m_v + \dot{V}_{ys} - \lambda_1\left(V_y - V_{ys}\right) \\ \dot{r} = -K_2\int sign(s_2)dt + d_2/m_v + \dot{r}_s - \lambda_2\left(r - r_s\right) \end{cases} \quad (55)$$

Differentiating both sides of (55) and then substitute the results into (54), $\dot{V}$ becomes

$$\begin{aligned} \dot{V} &= s_1\left[-K_1 sign(s_1) + \dot{d}_1/m_v + \ddot{V}_{ys} - \lambda_1\left(\dot{V}_y - \dot{V}_{ys}\right) - \ddot{V}_{ys} + \lambda_1\left(\dot{V}_y - \dot{V}_{ys}\right)\right] \\ &\quad + s_2\left[-K_2 sign(s_2) + \dot{d}_2/m_v + \ddot{r}_s - \lambda_2\left(\dot{r} - \dot{r}_s\right) - \ddot{r}_s + \lambda_2\left(\dot{r} - \dot{r}_s\right)\right] \\ &= s_1\left[-K_1 sign(s_1) + \dot{d}_1/m_v\right] + s_2\left[-K_2 sign(s_2) + \dot{d}_2/m_v\right] \\ &= -\left(K_1 - sign(s_1)\,\dot{d}_1/m_v\right)|s_1| - \left(K_2 - sign(s_2)\,\dot{d}_2/m_v\right)|s_2| < 0 \end{aligned} \quad (56)$$

By selecting the positive control $K_1 > \left|\dot{d}_1/m_v\right|$ and $K_2 > \left|\dot{d}_2/m_v\right|$, $\dot{V}$ will be negative and the Lyapunov function V converges to zero, which infers the reaching condition of the sliding surface is robustly satisfied. ■

Remark 6. In vehicle control, the desired control efforts in (53) need to be realized by vehicle actuation systems. Specifically, for AFS, the additional active front wheel steering angle can be determined using F_{yAFS} and $F_{yfl} + F_{yfr}$. First, based on the total desired lateral force ($F_{yAFS} + F_{yfl} + F_{yfr}$), a desired tire slip angle α_c can be obtained by a reverse tire model. Then, the required additional front wheel steering angle δ_{AFS} can be calculated as

$$\delta_{AFS} = \alpha_c - \delta_f + \tan^{-1}\left(\frac{V_y + l_f r}{V_x}\right), \quad (57)$$

where δ_f is the steering angle given by the driver, V_y and r are the real-time vehicle states measurements. The actual steering angle applied on the front wheels is $\delta_f + \delta_{AFS}$. For DYC, the desired yaw moment is realized by evenly distributing differential braking/driving forces between left and right tires. Depending on the yaw moment direction, the braking or driving force on each wheel can be calculated as

$$\begin{aligned} F_{xfl} &= -\frac{M_{DYC}}{4l_s \cos\left(\delta_f + \delta_{AFS}\right)}; F_{xfr} = \frac{M_{DYC}}{4l_s \cos\left(\delta_f + \delta_{AFS}\right)}; \\ F_{xrl} &= -\frac{M_{DYC}}{4l_s}; F_{xrr} = \frac{M_{DYC}}{4l_s} \end{aligned}, \tag{58}$$

where the negative sign denotes the braking force and the positive sign denotes the driving force. Through adjusting the positive weighting constants λ_1, λ_2, K_1, and K_2 in (18), the efforts of AFS and DYC can be adjusted.

To validate the proposed vehicle lateral stability analysis and control design, two Matlab-Simulink and CarSim® co-simulation scenarios, namely a high-speed cornering and a high-speed double lane change (DLC) maneuvers, are conducted and discussed. In the author's previous study [89], the superior of the proposed dynamic margin was specifically discussed and verified by comparing the cases of using the regions with and without the margin. In the authors' previous study [95], the effectiveness of the shiftable stability region has been experimentally validated. In this section, for conciseness, all the stability regions adopted in the controller design and simulation, if not specified, are constructed with the proposed dynamic margin. A C-class hatchback vehicle in CarSim® database is selected as the test vehicle, where the main vehicle parameters are listed in Table 2.

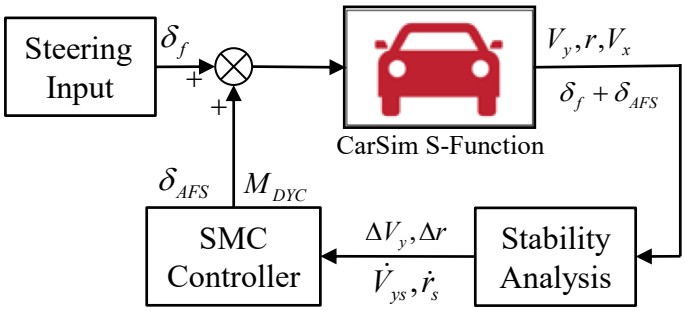

Fig. 20. Simulation Structure Diagram.

Based on the proposed stability analysis and control design, the simulation is structured as shown in Fig. 20, where the driver's steering input (δ_f), active front steering angle (δ_{AFS}), and yaw moment (M_{DYC}) are the three inputs to the CarSim® vehicle model. The longitudinal velocity (V_x), lateral velocity (V_y), yaw rate (r), and total steering angle $(\delta_f + \delta_{AFS})$ are the four exported signals from the CarSim® vehicle model. These four signals can be either directly measured or estimated to fulfill the requirements for the application to a real vehicle [107]. The stability analysis module, which consists of the projection method, shifting vector, and the dynamic margin, determines the vehicle stability status and outputs the necessary feedback errors to the SMC controller if the vehicle status is unstable (refer to Table 5). Based on the vehicle stability status and feedback errors, the control efforts are calculated and finally imported into the CarSim® vehicle model. Considering practical applications, the total steering angle, AFS angle, and steering rate of AFS are limited to [-30°, +30°], [-10°, +10°], and [-10°/s, +10°/s], respectively [108]. The yaw moment by DYC is limited to [-2000Nm, +2000Nm] [109].

4.3.1.2.Simulation - High-speed Cornering Maneuver

A high-speed cornering maneuver is selected to represent the scenarios that demand vehicle lateral stability at high speeds (e.g., cornering on the highway). In this case, with a constant high speed (90 km/h) and tire-road friction coefficient $\mu = 0.8$, a feedforward front steering angle is applied to the vehicle as shown in Fig. 21. The vehicle is expected to reach a steady-state after a certain time of constant steering. If the vehicle is unstable, the vehicle may likely have oversteering or severe understeering and thus operate unsafely.

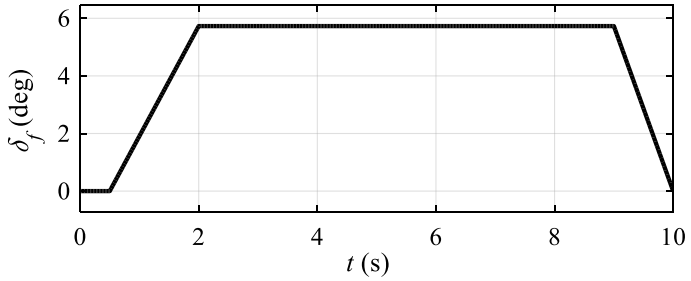

Fig. 21. Front Steering Angle Input in a High-speed Cornering Maneuver.

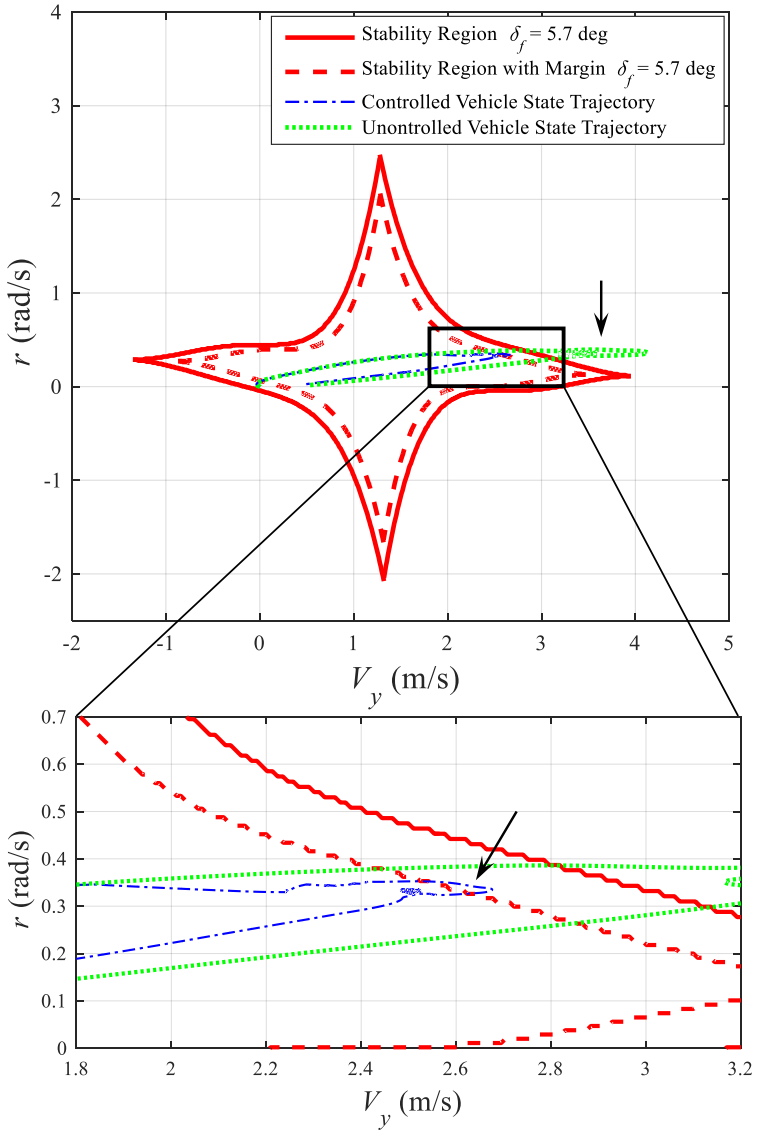

Fig. 22. Comparison of Vehicle State Trajectories Between the Controlled and Uncontrolled Cases.

In Fig. 22, the vehicle state trajectories of the uncontrolled and controlled cases are plotted and compared on a $V_y - r$ phase plane. The shifted stability region (solid curves) at the constant steering period (2-9s) and the corresponding margin (dashed curves) are also overlaid in the figure. As observed, without control, a part of the trajectory is out of

the upper-right boundary, which indicates that the vehicle is operating in an unstable (understeering) mode and may depart from the lane for a potential collision with other vehicles or road facilities. On the other hand, with the proposed control algorithm, the trajectory is always controlled in the region. Zooming into the portion that is close to the boundary, it can be observed that the undesired trajectory penetration is successfully avoided by the proposed dynamic margin.

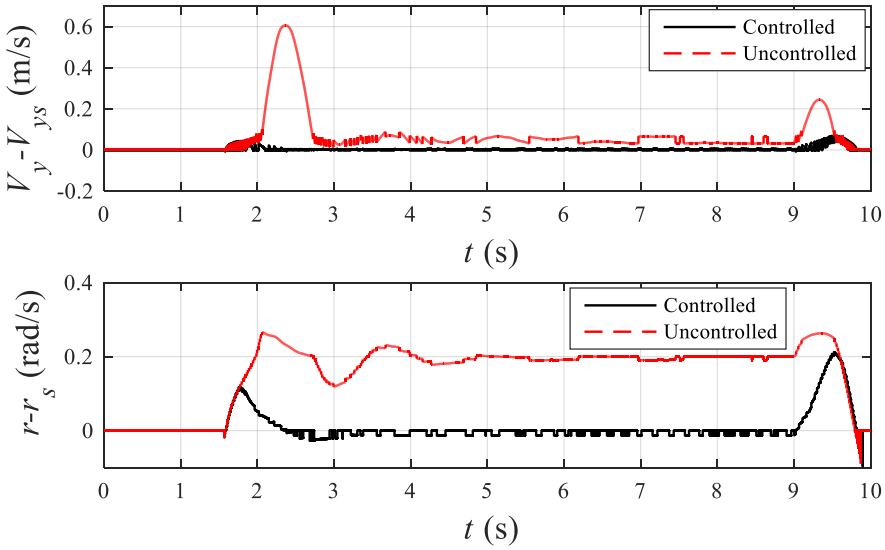

Fig. 23. Comparison of $V_y - V_{ys}$ and $r - r_s$ Between the Controlled and Uncontrolled Cases.

In Fig. 23, the vehicle state errors ($V_y - V_{ys}$ and $r - r_s$) with respect to the closest point on the boundary for the uncontrolled and controlled cases are presented and compared. As observed, without control, both $V_y - V_{ys}$ and $r - r_s$ (dashed) are relatively large, which is consistent with the observation in Fig. 22 that the vehicle trajectory is out of and far away from the stability region. On the other hand, with the proposed control for the same

maneuver, both $V_y - V_{ys}$ and $r - r_s$ (solid) are reduced to small values. Note that in Fig. 23, the small oscillation of $V_y - V_{ys}$ and $r - r_s$ in the controlled case is due to the intermittent controller activation (the controller is not activated until the vehicle state is approaching the boundary) but not the SMC chattering. For the uncontrolled case, the small oscillation is caused by the comparison of $\left(V_{ys}, r_s\right)$ in the projection method, which can be eliminated by increasing the accuracy of distance calculation. Based on the demonstration in Fig. 18, graphically, the small $V_y - V_{ys}$ (ΔV_y) and $r - r_s$ (Δr) infer that the vehicle state point A is close to the point B on the stability boundaries (with margin), meaning that the vehicle state point is "sliding" on the stability boundaries (with margin). In the calculation of dynamic stability region margin (*d* in (50)), based on a commonly adopted vehicle minimum reaction time as 0.01*s*, *n=10* (10 times of the sampling time (0.001*s*)) is selected.

The total steering angle and the moment of DYC applied to the vehicle are presented in Fig. 24. As observed, both the total steering angle ([-30°, +30°]) and yaw moment values (<1000Nm) are within a reasonable range and practically implementable. Fig. 25 compares the vehicle global trajectories of the controlled and uncontrolled cases with an ideal trajectory, which is obtained by applying the same steering signal to the CarSim® racecar model and keeping other parameters the same. It is observed that the cornering radius of the controlled case is smaller than that of the uncontrolled case. For the given steering input at a high speed, when the uncontrolled case is determined as unstable and has the understeering characteristic based on the analysis in Fig. 22, the proposed control helps the vehicle to avoid the understeering and reduce the cornering radius, which makes the vehicle trajectory closer to the ideal case.

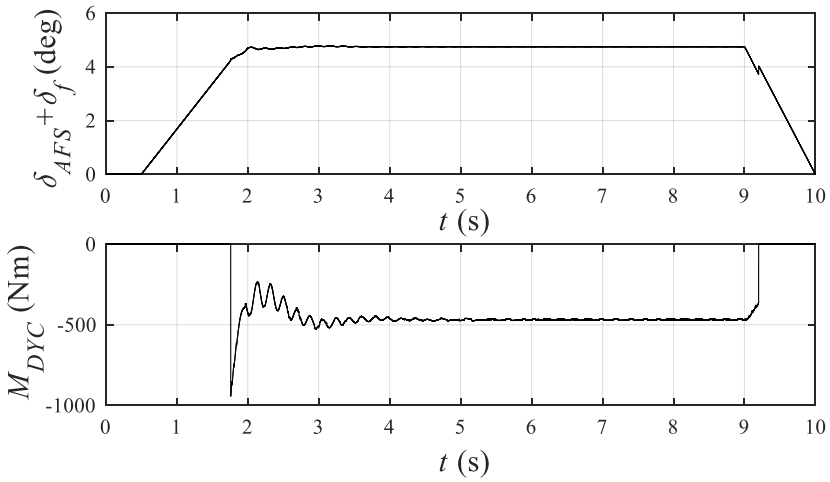

Fig. 24. Control Efforts of AFS and DYC for the High-speed Cornering Maneuver.

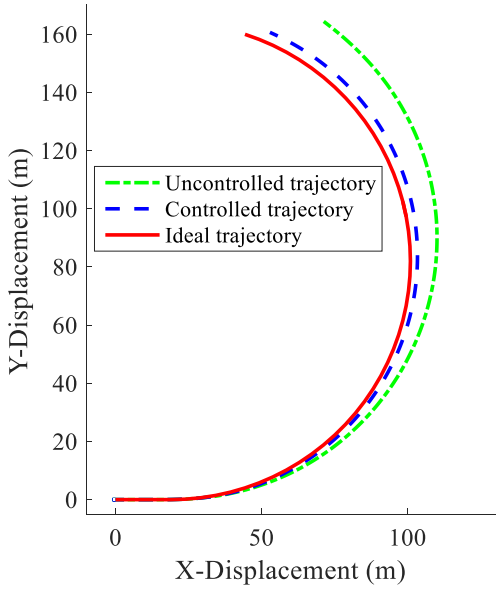

Fig. 25. Comparison of Vehicle Global Trajectories Between the Controlled and Uncontrolled Cases for the High-speed Cornering Maneuver.

4.3.1.3.Simulation - Double Lane Change Maneuver

In some emergencies, such as obstacle avoidance, vehicles are likely to lose stability, especially on low friction surfaces. In this subsection, the high-speed DLC maneuver is

conducted on both low and high friction surfaces to verify the effectiveness of the proposed stability control. In both low-μ and high-μ situations, a controlled case and an uncontrolled case are compared. Based on the driver model in the CarSim® database, the manually controlled front steering angle is given in Fig. 26. As observed, since the steering angle changes so rapidly during the double lane change, the proposed shifting vector becomes a critical feature in such a situation.

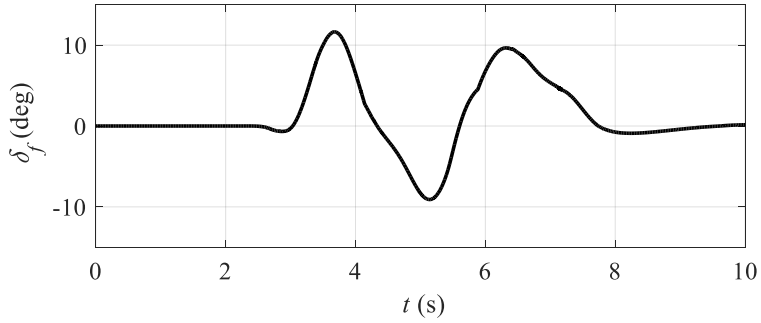

Fig. 26. Front Steering Angle Input in DLC Maneuver.

In the low-μ case, the vehicle speed is set to 90 *km/h* and $\mu = 0.5$. The comparison between the vehicle global trajectories of the uncontrolled, controlled, and ideal cases are shown in Fig. 27, where the trajectory in the ideal case is defined as the center of the lanes in DLC. As observed, the vehicle trajectory with the proposed control algorithm is closer to the ideal trajectory. Besides the vehicle trajectory improvement, more importantly, the vehicle states are also well-stabilized, which infers a better vehicle handling performance and lateral stability during the double lane change. To further illustrate this point, the results presented in Fig. 28 are discussed as follows.

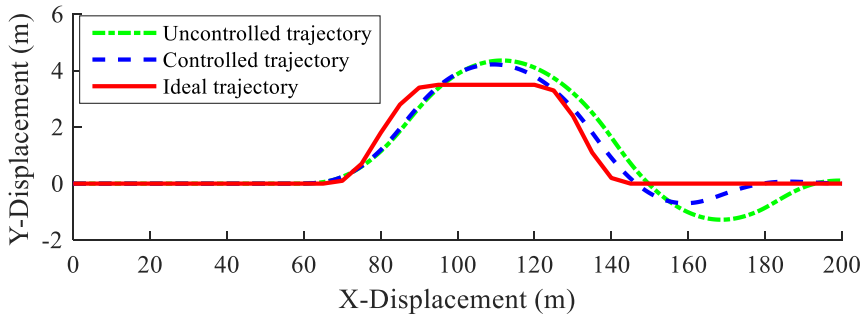

Fig. 27. Comparison of Vehicle Global Trajectories on a Low μ Road in DLC Maneuver.

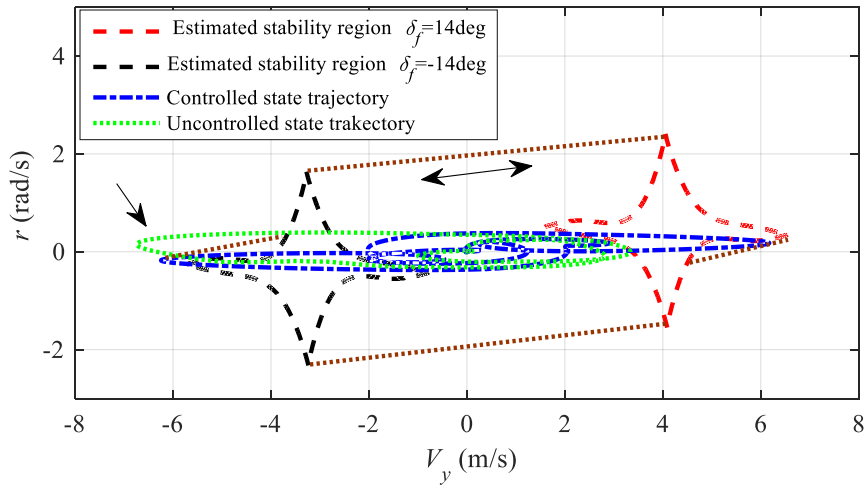

Fig. 28. Comparison of Vehicle State Trajectory on a Low μ Road in DLC Maneuver.

In Fig. 28, the comparison of vehicle state trajectories and the shifted stability regions at two extreme positions (when $\delta_{AFS}+\delta_f=\pm 14\,\text{deg}$) are presented. According to the shifting feature, as the steering angle changes between the maximum positive and negative values, the stability region shifts within the area bounded by the dotted lines between the two regions at the extreme positions. As observed, with the proposed control design, the vehicle state trajectory is well covered by the bounded area (depicted by the envelope plotted in dotted brown lines that consists of all the shiftable stability region boundaries)

as the stability region shifts. On the other hand, without control, no matter how the stability region shifts inside the bounded area, the vehicle state trajectory cannot be fully covered since the unstable vehicle state trajectory can be observed even when the stability region is shifted to the extreme position. Such an observation can also be verified by the stability status check results shown in Fig. 29. When the vehicle state trajectory is out of the stability region, the projection method determines the vehicle stability status as 'out'. During the whole process, the vehicle shows an unstable status twice, where the second one can be clearly observed (pointed by the arrow) in Fig. 28.

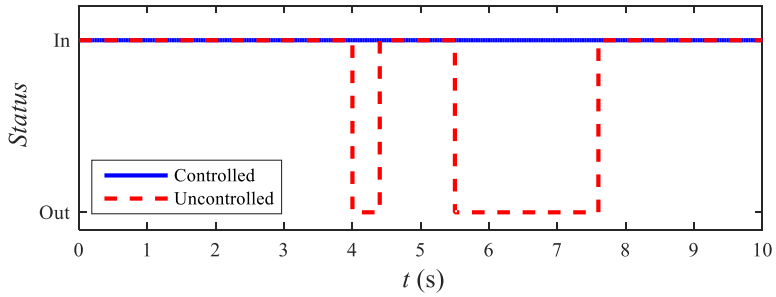

Fig. 29. Comparison of Vehicle Stability Status.

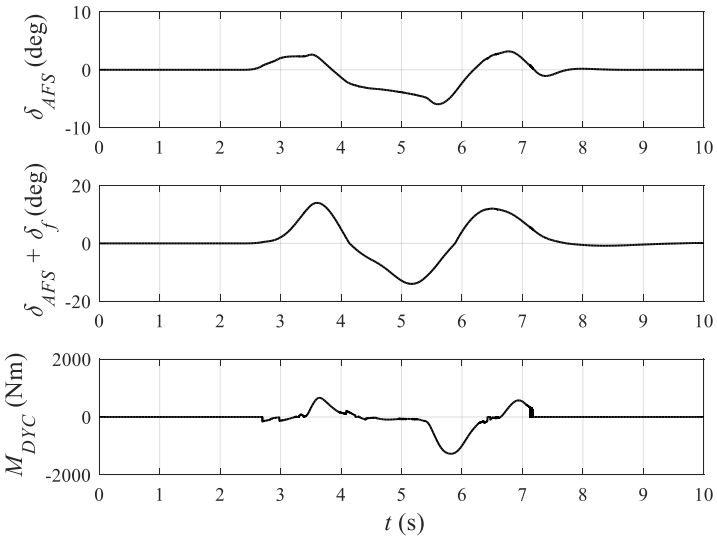

Fig. 30. Control Efforts of AFS and DYC in DLC Maneuver.

The applied control efforts of AFS and DYC during the double lane change are shown in Fig. 30. As observed, the maximum active steering angle is 6 degrees, the maximum total steering angle is 14 degrees, and the maximum yaw moment is 1200 Nm, which are all reasonable values and can be realized in practice [108][109].

In the high-μ case ($\mu = 0.8$), the same DLC simulation as in the low-μ situation was conducted. The comparison between the vehicle global trajectories of the uncontrolled, controlled, and ideal cases are shown in Fig. 31. As observed, the trajectory of the controlled vehicle is closer to the ideal trajectory compared with that of the uncontrolled vehicle. Similar to the low-μ case, the vehicle states are also well-stabilized. In Fig. 32, the vehicle state trajectory comparison and the shiftable stability regions at the positions of the maximum positive (11.4 deg) and negative (-9.16 deg) steering angles are presented. For the same DLC maneuver, since the higher μ allows larger tire lateral force, the required extreme steering angles are smaller than those on the low friction surface. As the steering angle changes, the stability region also shifts inside a bounded area between the regions at the extreme positions. As shown in Fig. 32, the controlled vehicle states trajectory (dash-dotted), which is covered by the bounded area, is within the stability regions all the time compared with that (dotted) in the uncontrolled case, indicating better vehicle stability and handling in the lateral direction. Based on the above analyses, it can be concluded that the proposed control algorithm can successfully ensure the vehicle's lateral stability.

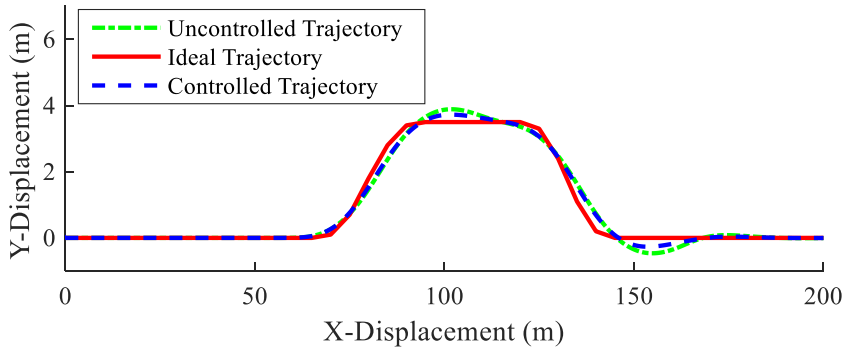

Fig. 31. Comparison of Vehicle Global Trajectories on a High μ Road in Double Lane Change Maneuver.

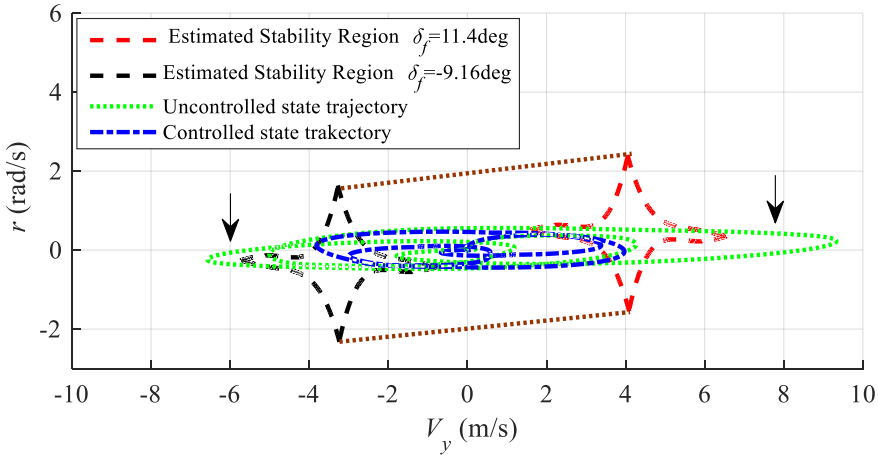

Fig. 32. Comparison of Vehicle State Trajectories on a High μ Road in Double Lane Change Maneuver.

4.3.2. AFS and ARS

4.3.2.1.Controller Design

To keep the vehicle always operate stably, an integrated AFS and ARS controller is designed. Comparing with the AFS plus DYC configuration, the integrated AFS plus ARS enables the stability region to shift along any combined direction (refer to (46)), which

enlarges the possible coverage of the stability region. The general control goal is also to keep the vehicle state trajectory always in the estimated stability region. With the mathematical representation of stability boundary function as $r = f\left(V_y\right)$, the sliding surface is selected as $S_s = r - f\left(V_y\right)$. If $S_s = 0$ is maintained, vehicle states $\left(V_y, r\right)$ will move along the stability region boundaries if the vehicle has a trend of being unstable. Suppose vehicle state errors ΔV_y and Δr are defined as,

$$\begin{cases} \Delta V_y = V_y - V_{ys} \\ \Delta r = r - r_s \end{cases}, \tag{59}$$

where V_{ys} and r_s are the coordinates of the closest point on the boundary to the current vehicle state $\left(V_y, r\right)$. Since $\left(V_{ys}, r_s\right)$ is always on the sliding surface, therefore, if ΔV_y and Δr are both converging to zero, which refers to $V_y = V_{ys}$ and $r = r_s$, the reaching conditions of the sliding surface will also be satisfied.

Proposition: Desired corrective lateral forces F_{yAFS} and F_{yARS}, which are generated by AFS and ARS, are shown in Eq. (60) and (61) respectively.

$$\begin{aligned} F_{yAFS} = & \frac{l_r}{l_f + l_r}\left(-k_1 \cdot \mathrm{sat}\left(V_y - V_{ys}\right) + \dot{V}_{ys} + V_x r\right) m_v \\ & - \left(F_{yfl} + F_{yfr}\right)\cos\delta_f + \frac{\left(-k_2 \cdot \mathrm{sat}\left(r - r_s\right) + \dot{r}_s\right) I_z}{l_f + l_r} \\ & + \frac{l_s\left[\left(F_{yfl} - F_{yflr}\right)\sin\delta_f - \left(F_{yrl} - F_{yrr}\right)\sin\delta_r\right]}{l_f + l_r}, \end{aligned} \tag{60}$$

$$
\begin{aligned}
F_{yARS} = \frac{1}{l_f + l_r} \Big\{ & l_f \left(-k_1 \text{sat}\left(V_y - V_{ys} \right) + \dot{V}_{ys} + V_x r \right) m_v \\
& - \left(-k_2 \text{sat}\left(r - r_s \right) + \dot{r}_s \right) I_z \\
& + l_s \left[\left(F_{yfl} - F_{yflr} \right) \sin \delta_f - \left(F_{yrl} - F_{yrr} \right) \sin \delta_r \right] \Big\} \\
& - \left(F_{yrl} + F_{yrr} \right),
\end{aligned}
\tag{61}
$$

where k_1 and k_2 are positive control gains.

Proof: A Lyapunov function candidate V, which consists of the defined sliding surface and its transpose, is constructed as,

$$
V = \frac{1}{2} S_s{}^T S_s > 0 . \tag{62}
$$

To satisfy the reaching condition of the sliding surface S_s, it is required that the derivation of Lyapunov function $\dot{V}$ to be negative definite as shown in (63),

$$
\begin{aligned}
\dot{V} = S_s^T \dot{S}_s &= \begin{bmatrix} \Delta V_y & \Delta r \end{bmatrix} \begin{bmatrix} \Delta \dot{V}_y \\ \Delta \dot{r} \end{bmatrix} . \\
&= \Delta V_y \Delta \dot{V}_y + \Delta r \Delta \dot{r} < 0
\end{aligned}
\tag{63}
$$

Thus, the derivatives of the sliding surface are selected to satisfy condition (63),

$$
\begin{bmatrix} \Delta \dot{V}_y \\ \Delta \dot{r} \end{bmatrix} = \begin{bmatrix} -k_1 sat\left(\Delta V_y \right) \\ -k_2 sat\left(\Delta r \right) \end{bmatrix}, \tag{64}
$$

where k_1 and k_2 are positive values and sat is the saturation function as shown in (65):

$$
sat(x) = \begin{cases} 1 & if \quad x \geq t \\ x & if \quad -t < x < t \\ -1 & if \quad x \leq -t \end{cases}, \tag{65}
$$

where t is the saturation threshold. Substitute (59) into (64), it gives,

$$\begin{bmatrix} \dot{V}_y - \dot{V}_{ys} \\ \dot{r} - \dot{r}_s \end{bmatrix} = \begin{bmatrix} -k_1 \cdot sat\left(\Delta V_y\right) \\ -k_2 \cdot sat\left(\Delta r\right) \end{bmatrix}. \tag{66}$$

Then, Eq. (66) can be rewritten as,

$$\begin{bmatrix} \dot{V}_y \\ \dot{r} \end{bmatrix} = \begin{bmatrix} -k_1 \cdot sat\left(\Delta V_y\right) + \dot{V}_{ys} \\ -k_2 \cdot sat\left(\Delta r\right) + \dot{r}_s \end{bmatrix}. \tag{67}$$

Substitute vehicle dynamic equations (1) and (2) into (67), the expressions of desired corrective lateral forces F_{yAFS} and F_{yARS}, as shown in (60) and (61), can be derived. ■

The next step is to convert the desired force into corrective active steering angles, which are δ_{fc} and δ_{rc}. The calculation of tire slip angle with active steering systems are:

$$\begin{aligned} \alpha_f &= \delta_f + \delta_{fc} - \tan^{-1}\left(\frac{V_y + l_f \cdot r}{V_x}\right) \\ \alpha_r &= \delta_r + \delta_{rc} - \tan^{-1}\left(\frac{V_y - l_r \cdot r}{V_x}\right) \end{aligned}, \tag{68}$$

where α_f and α_r can be calculated by the reverse of tire model function based on the sum of required corrective lateral force and current tire forces. Normally, rear wheel steering angle δ_r is initialized as 0, and front wheel steering angle δ_f can be easily measured. Therefore, the final representation of corrective steering angles is:

$$\begin{aligned}\delta_{fc} &= f_{LuGre}{}^{-1}\left(\left(F_{yfl}+F_{yflr}\right)\cos\delta_f + F_{yAFS}\right) \\ &\quad -\delta_f + \tan^{-1}\left(\frac{V_y + l_f \cdot r}{V_x}\right) \\ \delta_{rc} &= f_{LuGre}{}^{-1}\left(\left(F_{yrl}+F_{yrr}\right)\cos\delta_r + F_{yARS}\right) \\ &\quad + \tan^{-1}\left(\frac{V_y - l_r \cdot r}{V_x}\right)\end{aligned}, \tag{69}$$

where F_{yAFS} and F_{yARS} are obtained by (60) and (61).

Remark: As presented in (60) and (61), both F_{yAFS} and F_{yARS} are determined by the error dynamics of ΔV_y and Δr with two separate control gains. The AFS and ARS are integrated in such a manner so that the direction and the magnitude of active steering systems are determined automatically without any coupling relationships and relying on longitudinal velocity thresholds.

To validate the effectiveness of the estimated stability region and proposed integrated AFS and ARS control algorithm, Matlab/Simulink® and CarSim® co-simulation about a high-speed constant cornering maneuver and double lane change are carried out and corresponding results are presented and discussed. A 2012 C-class hatchback vehicle model from the CarSim® database, of which the parameters are shown in Table 2, is adopted for simulation. The general control structure of the system is shown in Fig. 33. Steering signal δ_f from the driver is firstly inputted into the system, δ_{fc} and δ_{rc} are active front and rear wheel steering angle in addition to δ_f. Vehicle yaw rate and lateral velocity are assumed to be observable. Then, based on observed vehicle states, a series of stability analyses introduced in section 4.2 is applied with real-time updated stability regions.

Thereafter, SMC controller calculates control efforts, which will be finally inputted to the system as active steering angles.

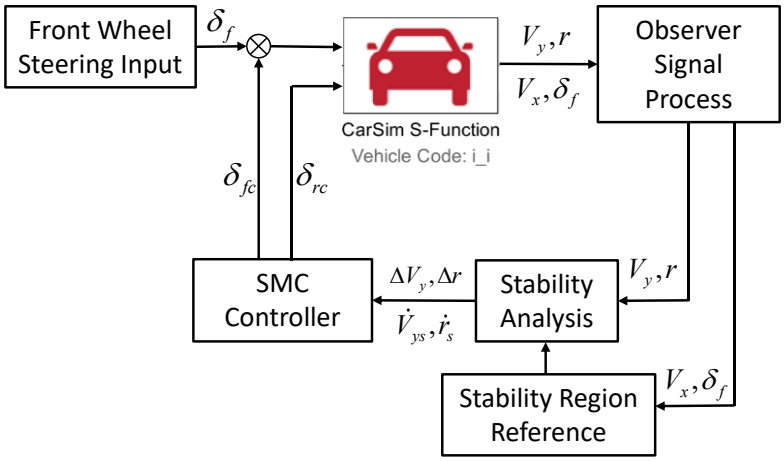

Fig. 33. Simulation Control Structure

4.3.2.2.Simulation - Constant Cornering Maneuver

To show the effectiveness of the proposed control algorithm, especially for steady-state vehicle stability, a high-speed constant cornering maneuver, with a constant V_x at 90km/h, is utilized as an example. The tire-road friction coefficient μ is set to be 0.8. Front wheel steering input from the driver is shown in Fig. 34. The steering angle starts from 0 degrees and then ramps up to 8.6 degrees (0.15rad) in five seconds. After keeping at constant at 8.6 degrees for 4 seconds, it ramps down to 0 degrees again.

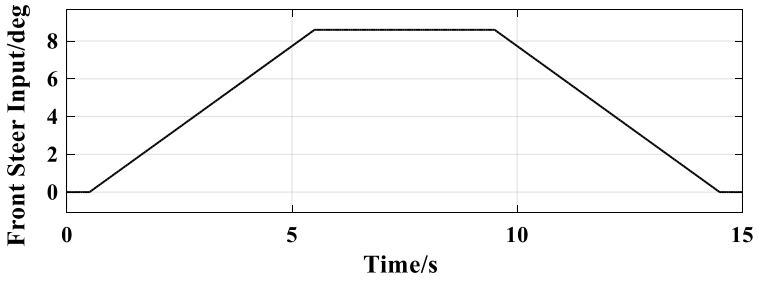

Fig. 34. Steering Angle Input of Front Wheels.

Vehicle state trajectory overlaid with steady stability region and stability status over the whole simulation process time, with AFS only and with the integrated AFS and ARS control, are shown and compared in Fig. 35 and Fig. 36 respectively. In Fig. 35, it can be observed that with only AFS control, even the stability region shifts along the arrow direction as the steering angle is changing, there is still a portion of the vehicle state trajectory located out of the region. However, with the proposed AFS and ARS integrated control algorithm, the vehicle state trajectory is always located within the stability region.

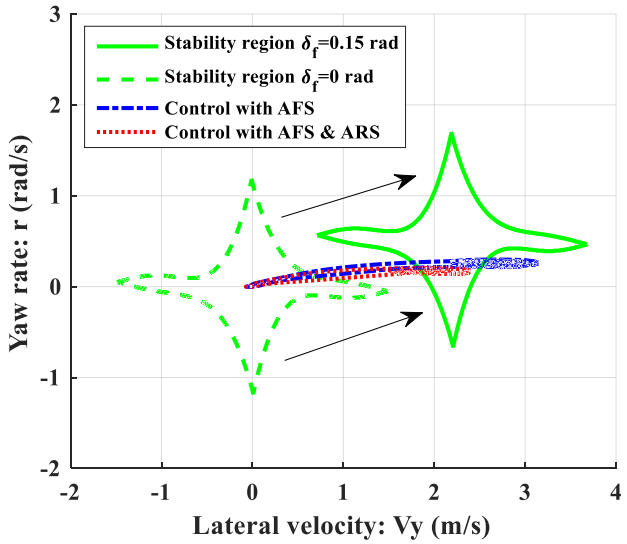

Fig. 35. Vehicle Stability Status Comparisons on the Phase Plane.

Note that both vehicle state trajectory and stability region move during the whole simulation period, thus, to check vehicle stability status during the whole procedure, vehicle status plot, as shown in Fig. 36, is presented for analysis. As observed in subplot a), with AFS controller, vehicle status is partially detected as out of the region (unstable). However, with proposed integrated control as shown in subplot b), vehicle status chatters between stable and unstable for most of the simulation period with regard to the stability boundary with margin. This alternative stability status change refers to the case that vehicle

states are controlled to move along the sliding surface, which helps the vehicle to maintain stable status in a critical way. In subplot c), vehicle status is determined according to the actual stability region. Benefit from the application of stability region margin, vehicle state is controlled always within stability region and shows the stable status (In).

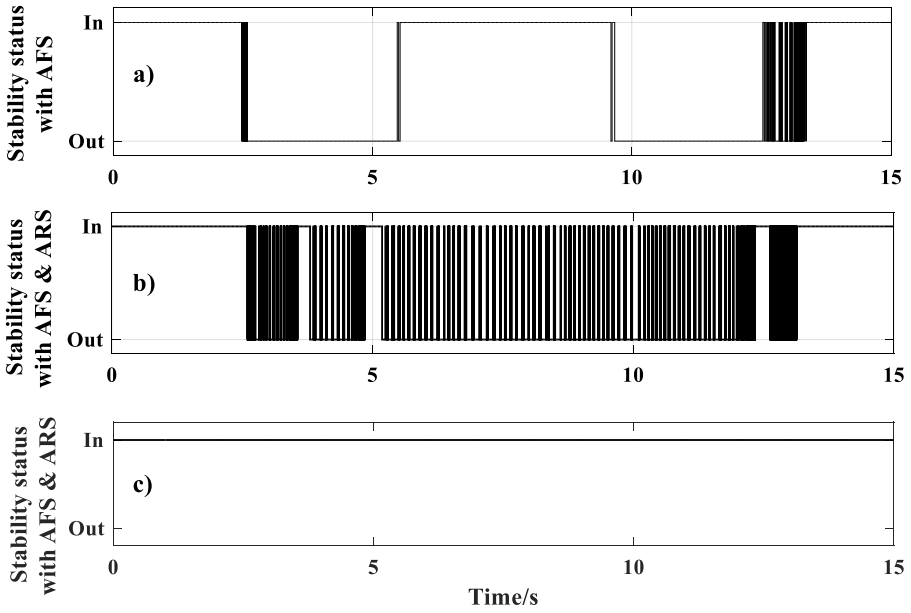

Fig. 36. Vehicle Status Comparison, a)AFS; b)AFS+ARS w.r.t. Stability Region With Margin; c) AFS+ARS w.r.t. Original Stability Region.

The actual front and rear wheel steering angles are shown in Fig. 37. As observed, the direction of the rear wheel steering angle, which is determined automatically based on the proposed control algorithm, is the same as that of front wheels at high speed to make the vehicle stable.

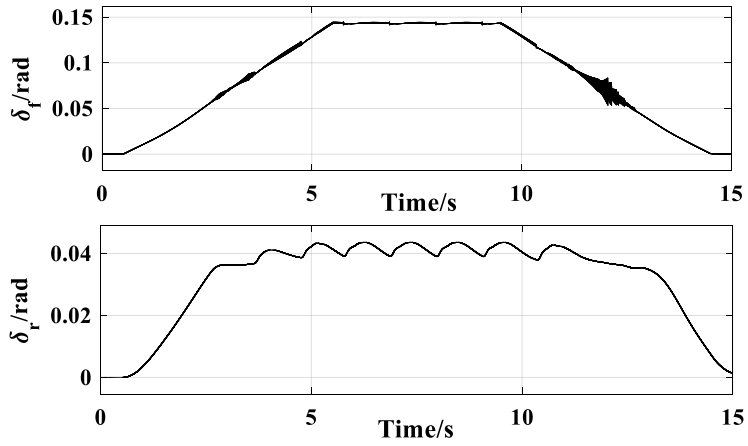

Fig. 37. Actual Front and Rear Steering Angles.

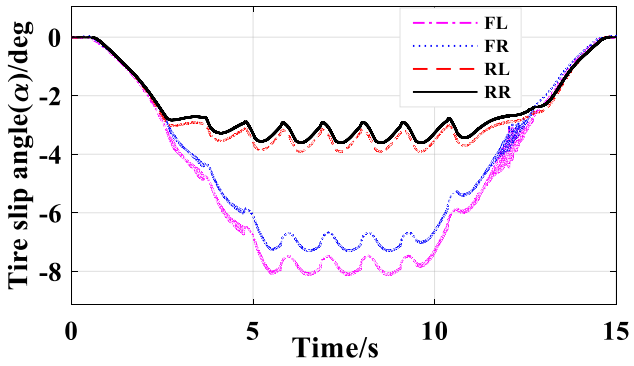

Fig. 38. Tire Slip Angles.

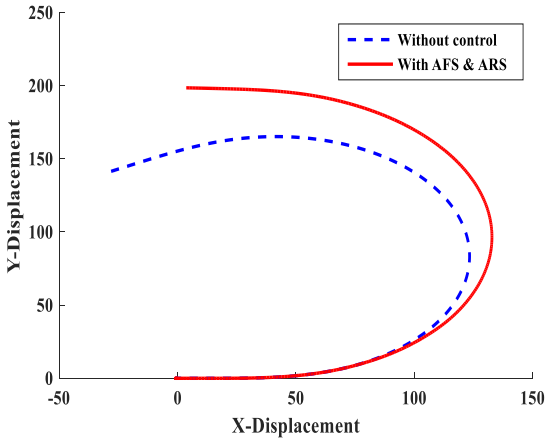

Fig. 39. Vehicle Trajectory Comparison.

Fig. 38 shows the slip angle of each tire. As observed, even front two tires show larger slip angle than the rear wheels, they are relatively small values, which refer to stable tire conditions without saturation based on the tire model. Moreover, the effectiveness of the proposed controller can be also reflected by the vehicle displacement trajectory. As shown in Fig. 39, the cornering radius of the case with integrated AFS and ARS control is larger than that of the case without control, which implies that the unstable (oversteering) condition for the uncontrolled case is corrected by the proposed control algorithm.

4.3.2.3.Simulation - Double Lane Change Maneuver

To further demonstrate the effectiveness of the proposed control algorithm, a more challenging double lane change maneuver is applied. Vehicle longitudinal velocity V_x is initially set to 90km/h and the road friction coefficient μ is set to 0.5 as a low friction condition. As observed in Fig. 40, the trajectory of the vehicle with integrated AFS and ARS control is closer to the road reference compared with that of the vehicle with only AFS control. This observation indicates that vehicle lateral tracking behavior can also be improved while vehicle stability is controlled.

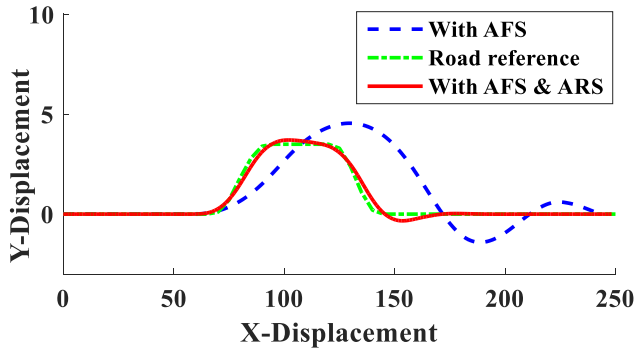

Fig. 40. Vehicle Double Lane Change Trajectory Comparisons.

The actual front and rear steering angles during double lane change are shown in Fig. 41. As observed, the rear wheels are steered in the same direction as the front wheels for most of the time to stable the vehicle's lateral motion. However, front and rear steering directions do not necessarily need to be the same. The direction and magnitude of the integrated active steering system are automatically determined by (69). For example, around 7 seconds, front and rear wheels are steered oppositely to generate a large yaw moment to keep the vehicle in the right direction.

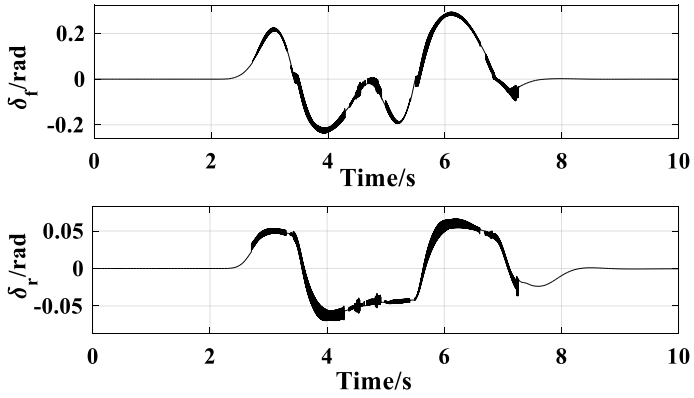

Fig. 41. Actual Front and Rear Steering Angles for a Double Lane Change.

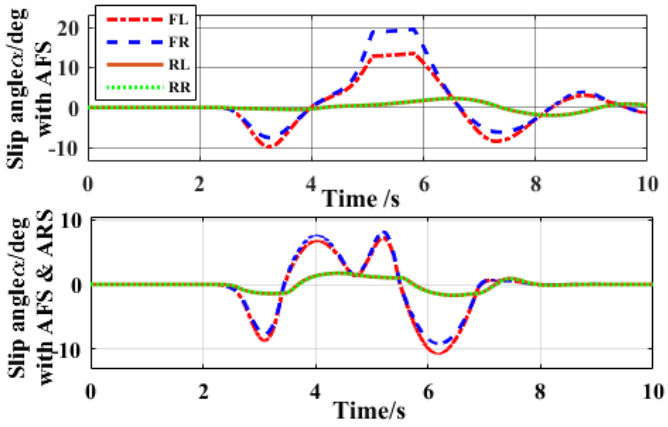

Fig. 42. Tire Slip Angle Comparisons for a Double Lane Change.

Slip angles of each wheel under the case with only AFS control and with integrated AFS and ARS control are shown and compared in Fig. 42. As observed, with only AFS control, tire slip angles of the front two wheels both exceed 20 degrees, which typically lead to unstable tire status and ineffective control results. However, for the case with integrated AFS and ARS control, slip angles of all the tires are significantly reduced to small values, which indicates that all the tires are working stably.

4.4. Non-Overshooting Model Predictive Control

Although the dynamic SMC controllers in section 4.3 show their effectiveness in guaranteeing vehicle stability, the signal chattering issues, although was reduced compared with normal SMC, can still be observed in the simulations. To address this issue, if the boundaries are considered as references, a non-overshooting control design with respect to the references can satisfy the vehicle stability control requirements. Theoretically, non-overshooting control design in the literature can be generally categorized into two groups for linear and nonlinear systems, respectively. Although the non-overshooting control designs for some specific systems (especially for nonlinear systems in certain forms) were studied, a uniformed non-overshooting control design for general dynamic systems has not been discussed in the literature. In this section, through the advantages of handling constraints, model predictive control (MPC) is utilized as an appropriate approach to develop a uniformed non-overshooting control design for general dynamic systems. Specifically, during the entire prediction horizon, non-overshooting inequality constraints are applied at each sampling time to avoid the overshooting of system outputs. Four

different non-overshooting constraints in terms of different system output responses are proposed and discussed.

To apply the proposed non-overshooting MPC to the region-based vehicle stability control problem, the descriptions of non-overshooting constraints with respect to the stability boundaries are essential. Thus, a set of reformed inequality constraints, which are derived based on the characteristics of the estimated stability regions, are proposed and implemented in the non-overshooting MPC design. The proposed non-overshooting MPC control is applied to resolve a region-based vehicle lateral stability control problem.

4.4.1. Non-overshooting Constraints

Consider a general nonlinear system in the discrete-time form,

$$\begin{aligned} x(k+1) &= f\left(x(k), u(k)\right), \\ y(k) &= h\left(x(k)\right), \end{aligned} \tag{70}$$

where $x(k) \in R^n$ is the state vector at the time step k, $u(k) \in R^m$ is the control input vector, and $y(k) \in R^p$ is the output vector. The objective of the MPC design is to find a control input that minimizes the following cost function,

$$\begin{aligned} J(k) = &\sum_{j=1}^{N-1} \left[x(k+j|k) - x_{ref} \right]^T Q \left[x(k+j|k) - x_{ref} \right] \\ &+ \sum_{j=1}^{P-1} \Delta u(k+j|k)^T R \Delta u(k+j|k) \end{aligned}, \tag{71}$$

subject to,

$$\begin{aligned} &x(k+j|k) \in X, \\ &u(k+j|k) \in U, \ 0 \le j \le P-1, \end{aligned} \tag{72}$$

where Q and R are the weighting matrices. x_{ref} is the reference at each sampling instant. N and P are the prediction and control horizon, respectively. X and U are the compact subset of R^n and R^m, respectively. Δu is defined as $\Delta u(k+j|k) = u(k+j|k) - u(k+j-1|k)$. The final control sequence is $u(\cdot|k) = \left[u(k|k), \ldots, u(k+P-1|k)\right]^T$, where only the first element is applied to the system (70).

To achieve the non-overshooting MPC design of system outputs with respect to the references, four different inequality constraints (C1-C4) are proposed as follows,

C1: $y_i(k+1|k) \le y_{i-ref}$;

C2: $y_i(k+j|k) \le y_{i-ref}$, where $1 \le j \le N$;

C3: $y_i(k+N|k) \le y_{i-ref}$ & $y_i(k+j|k) \le y_i(k+N|k)$, where $1 \le j \le N-1$;

C4: $y_i(k+N|k) \le y_{i-ref}$ & $y_i(k+j|k) \le y_i(k+j+1|k)$, where $1 \le j \le N-1$,

where $y_i(k+j|k)$ is the predicted value of the *i*th system output at the *j*th prediction horizon step and the y_{i-ref} is the *i*th reference variable. In these four constraints, C1 requires the value of the first prediction horizon step is less than or equal to the reference. C2 requires the system output at each predicted time step to be constrained. C3 contains two inequalities, where the first requires the last step in the prediction horizon is less or equal than the reference, and the other limits the output at each step to be less or equal than the value at the last step. C4 also contains two inequalities, in which the first is the same as the first one in C3, and the second one forms a constraint chain between each time step,

which infers a monotonic characteristic. The intrinsic differences among C1-C4 are illustrated by the following proposition.

Proposition 1. Assume the prediction and control horizons in MPC have the same length N, the non-overshooting constraints of system outputs with respect to the reference at the *j*th step in the prediction horizon ($y_i\left(k+j|k\right)$, $1 \le j \le N$) cannot guarantee the system outputs are non-overshooting at other predicted time steps ($y_i\left(k+n|k\right)$, $n \ne j$, $1 \le n \le N$).

Proof. To demonstrate if the constraints applied to the *j*th step $y_i\left(k+j|k\right)$ have impacts on other $y_i\left(k+n|k\right), n \ne j$ in the prediction horizon, two different cases should be considered: 1) impacts on the previous steps $y_i\left(k+n|k\right), 0 < n < j$; 2) impacts on the following steps $y_i\left(k+n|k\right), j < n < N$.

Case 1: To evaluate if the constraints at the *j*th step have impacts on the previous steps, a constraint chain can be formed by only analyzing if the constraints on the *j*th step have impacts on the *j-1*th step.

$$x\left(k+j|k\right) = f\left(x\left(k+j-1|k\right), u\left(k+j-1|k\right)\right) \le x_{ref}\,, \tag{73}$$

$$x\left(k+j-1|k\right) \le x\left(k+j|k\right) = f\left(x\left(k+j-1|k\right), u\left(k+j-1|k\right)\right). \tag{74}$$

Assume that the inequality (73) is the constraint on the system state vector (selected as the system output) at the *j*th step in the prediction horizon. Only when the inequality (74) is satisfied, $x\left(k+j-1|k\right) \le x_{ref}$ at the *j-1*th step holds. However, since $u\left(k+j-1|k\right)$ in (74) is independently determined by the optimization problem without any non-overshooting constraints yet, the inequality in (74) could not be guaranteed. Therefore, the

constraint chain may not be formed and the constraints on $y_i\left(k+j|k\right)$ at the *j*th step cannot sufficiently imply any constraints on $y_i\left(k+n|k\right),\ 0<n<j$.

Case 2: Similar to the constraint chain analysis in Case 1, assume $x\left(k+j|k\right)\le x_{ref}$ is the constraint on the system state vector (selected as the system output) at the *j*th step in the prediction horizon. Only when the inequality (75) is satisfied, $x\left(k+j+1|k\right)\le x_{ref}$ holds.

$$x\left(k+j+1|k\right)=f\left(x\left(k+j|k\right),u\left(k+j|k\right)\right)\le x\left(k+j|k\right) \tag{75}$$

However, due to a similar reason for the control as explained in Case 1, the constraint (75) cannot be guaranteed. Therefore, the constraints on $y_i\left(k+j|k\right)$ cannot sufficiently imply any constraints on $y_i\left(k+n|k\right), j<n<N$. ■

Remark 7. From Proposition 1, the constraints on one time step do not necessarily have impacts on other time steps before or after in the prediction horizon. Thus, by adding more restrictions on each time step for the four non-overshooting constraints from C1 to C4, the constraints become stricter and consequently result in different system output responses.

4.4.2. Numerical Examples and Discussions

In this section, a linear system and a nonlinear system are taken as examples to briefly illustrate and compare the impacts of the proposed constraints in section 4.4.1.

Linear system:

Consider a simple mass-spring-damper system in the state space form [110],

$$\begin{aligned} \dot{x} &= Ax + Bu \\ y &= Cx + Du \end{aligned}, \tag{76}$$

where $x = \begin{bmatrix} z \\ v \end{bmatrix}$, $A = \begin{bmatrix} 0 & 1 \\ -\frac{k}{m} & -\frac{b}{m} \end{bmatrix}$, $B = \begin{bmatrix} 0 \\ \frac{1}{m} \end{bmatrix}$, $C = \begin{bmatrix} 1 & 0 \end{bmatrix}$, and $D = \begin{bmatrix} 0 \\ 0 \end{bmatrix}$. The parameter values are $m = 5kg$, $k = 0.1\ N/m$, and $b = 0.1\ N \cdot s/m$. The initial condition is $x(0) = \begin{bmatrix} 0 & 0 \end{bmatrix}^T$ and the reference is $x_{ref} = \begin{bmatrix} 4 & 0 \end{bmatrix}^T$. Weighting matrices in the MPC design are $Q = \begin{bmatrix} 10 & 1 \\ 1 & 10 \end{bmatrix}$ and $R = \begin{bmatrix} 1 \end{bmatrix}$. The prediction and control horizons are set to 10. The sampling instant is $T_s = 0.05s$.

In Fig. 43, the step responses for different constraints are compared. For an MPC design without any non-overshooting constraints, an obvious output overshoot (the green triangular dash line) with respect to the reference is observed.

For the same MPC design with different non-overshooting constraints C1-C4, the step responses are shown in Fig. 43 as well. All four constraints successfully eliminate the overshoot. However, the system responses are quite different. As mentioned in Remark 1, although only the first step in the control sequence is applied to the system, the additional constraints applied to other time steps (in C2-C4) still have impacts on the optimized control sequence, which causes different system output responses.

The first difference is about convergence. For C1, the system output oscillates after reaching the reference at 1.5s. For C2 and C3, similar oscillations with smaller amplitudes are observed. Based on Proposition 1, the output variation cannot be guaranteed for C1-C3 even if the control goal is achieved by minimizing the cost function. However, for C4, the

system output reaches the reference monotonically without any oscillation. The second difference of the system responses for different constraints is the settling time (w.r.t. 98% reference). For four non-overshooting constraints, C1 gives the shortest settling time. C2 and C3 cause similar but longer settling time compared with C1. C4 generates the longest settling time among the four constraints. From C1 to C4, since the constraints become stricter, the optimized control input sequence becomes more conservative, which may cause a longer settling time.

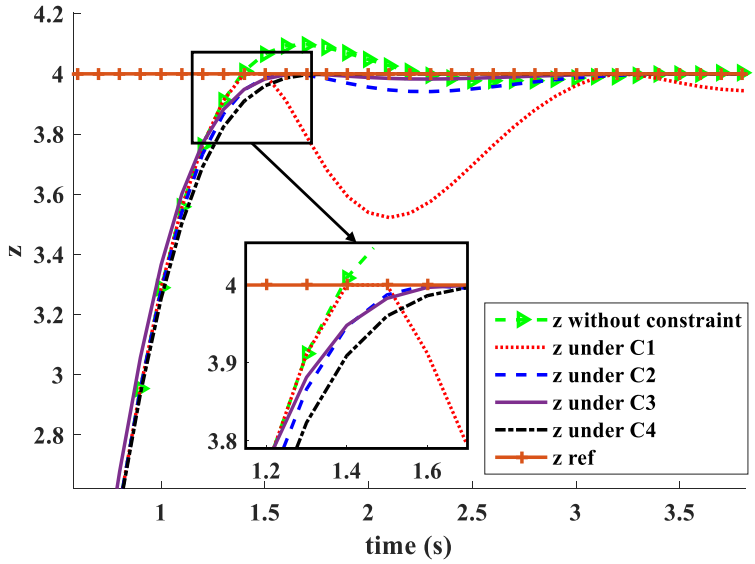

Fig. 43. Comparisons on Step Responses of a Linear System for Different Non-overshooting MPC Constraints.

Nonlinear system: Consider a cart-pendulum system with the following dynamics [110],

$$x = \begin{bmatrix} z & \dot{z} & \theta & \dot{\theta} \end{bmatrix}^T$$

$$\dot{x} = \begin{bmatrix} \dot{z} \\ \dfrac{F - K_d \dot{z} - m_p L \dot{\theta}^2 \sin\theta + m_p g \sin\theta \cos\theta}{m_c + m_p \sin^2\theta} \\ \dot{\theta} \\ \dfrac{\left(F - K_d \dot{z} - m_p L \dot{\theta}^2 \sin\theta\right)\cos\theta + \left(m_c + m_p\right) g \sin\theta}{L\left(m_c + m_p\right) - m_p L \cos^2\theta} \end{bmatrix}, \tag{77}$$

where z, θ, and u are the cart position, pendulum angle, and input force applied on the cart. The parameter values are $m_p = m_c = 1kg$, $L = 0.5m$, and $K_d = 10\ \ N \cdot s/m$. The initial condition is $x(0) = \begin{bmatrix} 0 & 0 & -\pi & 0 \end{bmatrix}^T$ and reference is $x_{ref} = \begin{bmatrix} 4 & 0 & 0 & 0 \end{bmatrix}^T$. Weighting matrices are $Q = \begin{bmatrix} 10 & 0 \\ 0 & I_3 \end{bmatrix}$ and $R = \begin{bmatrix} 1 \end{bmatrix}$. The prediction and control horizons are 10 time steps with the sampling step at $T_s = 0.05s$.

As observed in Fig. 44, the overshoots of the nonlinear system responses are similar to those of the linear system example for the MPC design without and with the non-overshooting constraints C1-C4. For other characteristics of system responses, the oscillations are still observed for C1-C3, but the amplitudes become smaller as the constraints become stricter. For C4, since the system response is required to be monotonic, the system output reaches the reference without oscillation although settling down slower than those for C1-C3.

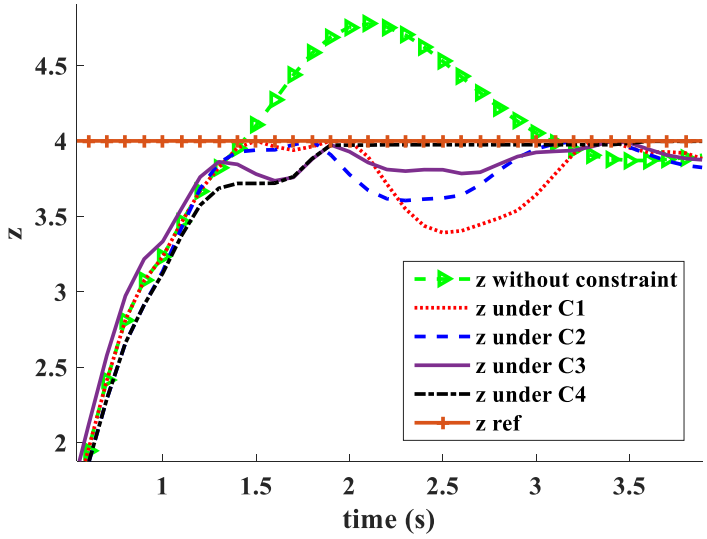

Fig. 44. Comparisons on Step Responses of a Nonlinear System for Different Non-overshooting MPC Constraints.

By decreasing the sampling time of a discrete-time system, both the overshoot percentage and the response oscillation will be reduced. By decreasing the R weighting for control in the cost function, the overshoot percentage and the response oscillation will also be reduced. These well-known facts are also true for the non-overshooting MPC design.

However, as the sampling time becomes small, the computational effort increases dramatically. Moreover, as R decreases, the control input becomes more aggressive, which usually causes impractical control efforts and may violate the system capability. Therefore, to reduce the overshoot percentage and oscillation, small sampling time periods and R values are probably not practical and effective. Thus, the four non-overshooting constraints C1-C4 provide different options.

4.4.3. Non-overshooting MPC for Vehicle Stability Control

The control objective is to minimize the following cost function when the vehicle states are going to pass the stability boundary,

$$\begin{aligned} J(k) = &\sum_{j=1}^{N-1} \left[x(k+j|k) - x_s \right]^T Q \left[x(k+j|k) - x_s \right] \\ &+ \sum_{j=1}^{P-1} \Delta u(k+j|k)^T R \Delta u(k+j|k) \end{aligned} \tag{78}$$

where $x = \left[V_y, r \right]^T$, $x_s = \left[V_{ys}, r_s \right]^T$, $Q = \begin{bmatrix} 10 & 1 \\ 1 & 10 \end{bmatrix}$, $R = \left[0.001 \right]$ and $\Delta u(k+j|k) = F_{y-AFS}(k+j|k) - F_{y-AFS}(k+j-1|k)$.

The minimization is subject to the non-overshooting constraints, which guarantee that vehicle states are always within the stability region. Using the mathematical expressions of each stability region boundary, the non-overshooting constraints are reformed as follows,

$$\begin{aligned} &No.\text{seg} = 1: \quad r \le f_1(V_y) \quad \& \quad V_y \in \left[V_{y-\min}, V_{y-mid} \right]; \\ &No.\text{seg} = 2: \quad r \le f_2(V_y) \quad \& \quad V_y \in \left[V_{y-mid}, V_{y-\max} \right]; \\ &No.\text{seg} = 3: \quad r \ge f_3(V_y) \quad \& \quad V_y \in \left[V_{y-mid}, V_{y-\max} \right]; \\ &No.\text{seg} = 4: \quad r \ge f_4(V_y) \quad \& \quad V_y \in \left[V_{y-\min}, V_{y-mid} \right]. \end{aligned} \tag{79}$$

Among the four constraints in (79), the most applicable one is selected depending on the *No*.seg, which is obtained from the preliminary stability analysis. Note that in (79), if the *No*.seg is 1 or 2, the constraints represent a non-overshooting problem; if the *No*.seg is 3 or 4, the constraints represent a non-overshooting problem in an opposite direction. In this MPC design, among the four non-overshooting constraints presented in Section 4.4.1, C4 is adopted to achieve the control objective while avoiding any undesired oscillations.

The control input is a sequence of F_{y-AFS}, where only the first element is applied at each sampling instant.

4.4.4. Simulation Results and Discussions

In this section, the proposed non-overshooting MPC design for the region-based vehicle stability control is evaluated through a high-speed cornering maneuver in the co-simulation of CarSim® and Matlab/Simulink. The stability region is estimated using the parameters of a 2012 C-class hatchback from the CarSim® database. Some vehicle and MPC parameters are listed in Table 6.

Table 6. Parameters of Vehicle and MPC

Symbol	Parameter	Value
m_v	Vehicle mass	1270 kg
I_z	Yaw inertia	1536.7 $kg{\cdot}m^2$
L	Wheelbase	2.91 m
l_f	Front wheelbase	1.11 m
l_r	Rear wheelbase	1.8 m
l_s	Half of the vehicle track	0.835 m
N	Prediction horizon	10
P	Control horizon	10
T_s	Sampling instant	0.05s

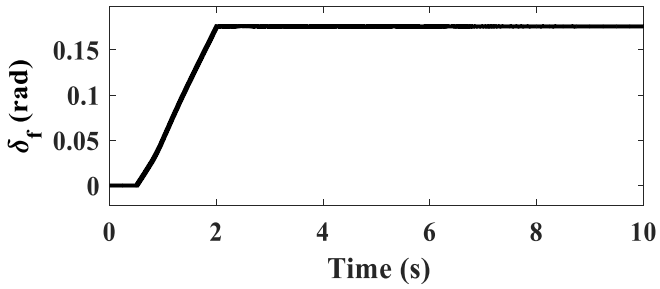

Fig. 45. Steering Angle Input.

The vehicle speed is fixed at 90 km/h. The steering angle is shown in Fig. 45, in which the front wheel steering angle starts at zero and ramps up to 0.18 rad in 1.5 seconds and then keeps constant.

The effectiveness of the proposed method is evaluated through the comparisons among three cases: 1) without MPC control; 2) a normal MPC without using the proposed non-overshooting constraints; 3) the non-overshooting MPC using the proposed constraints. Case 1 and 3 are first compared. In Fig. 46, although the stability region shifts as δ_f changes, a portion of the state trajectory of case 1 (the right end blue dash-dot lines) is still observed out of the stability region. However, the state trajectory of case 3 (green dot) is kept in the moving stability region. Note that although only the initial and end stability regions are plotted in Fig. 46, the continuous variations were monitored and verified in the simulation. This observation can be further verified by comparing the actual vehicle state with the closest point on the boundary for case 3.

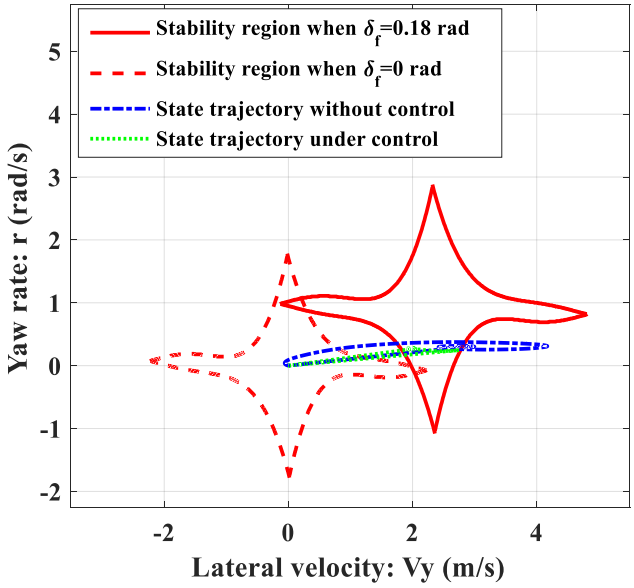

Fig. 46. Comparisons of State Trajectories Between Case 1 and Case 3.

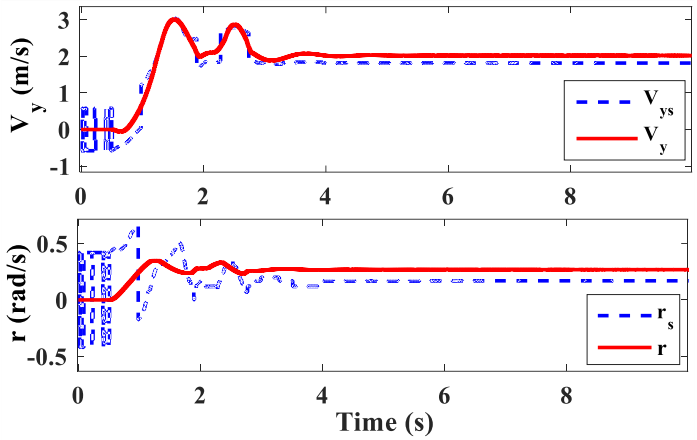

Fig. 47. Vehicle States and the Closest Point on the Boundary for Case 3.

In Fig. 47, both V_y and r are larger than V_{ys} and r_s at the steady-state. The stability analysis shows that the 4th boundary is the closest one to the vehicle state point. Therefore, the *No*.seg = 4 constraint in (79) is satisfied. Note that during the period when the steering angle (0-2s) and the vehicle states (0-2.7s) change, due to the simultaneous changes of the vehicle states and the stability region, the *No*.seg may change frequently and is not always 4. This causes the fluctuation of V_{ys} and r_s in Fig. 47. However, this observation does not mean the vehicle states are out of the stability region.

To further demonstrate the effectiveness of the proposed non-overshooting MPC design, case 2 and 3 are compared. As shown in Fig. 48, in case 2, the vehicle state trajectory without using the non-overshooting constraints (blue) are partially controlled within the region. However, in case 3, the whole vehicle state trajectory (green) are controlled within the stability region. This observation can be verified by checking the vehicle status of case 2. As shown in Fig. 49, from 1.5 to 4.2 seconds, the vehicle stability status is *Out* (of the stability region) for three times, which infers that the vehicle state

trajectory penetrated the stability region boundary and caused the overshooting trajectory (blue) as observed in Fig. 48.

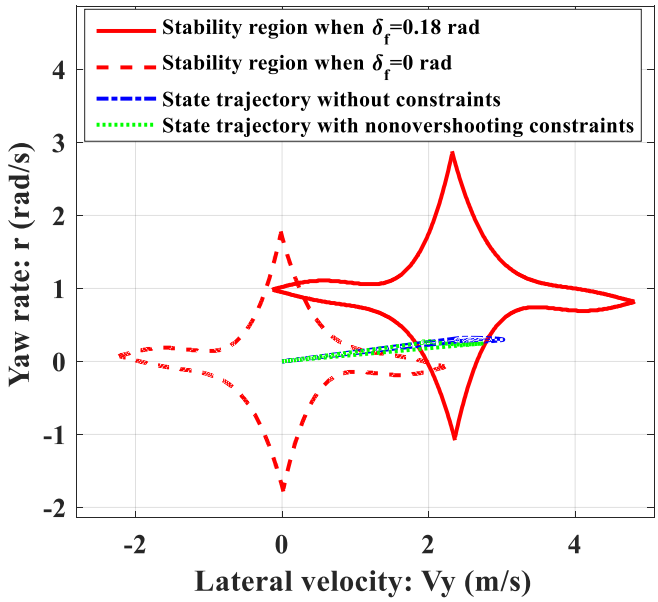

Fig. 48. Comparisons of State Trajectories Between Case 2 and Case 3.

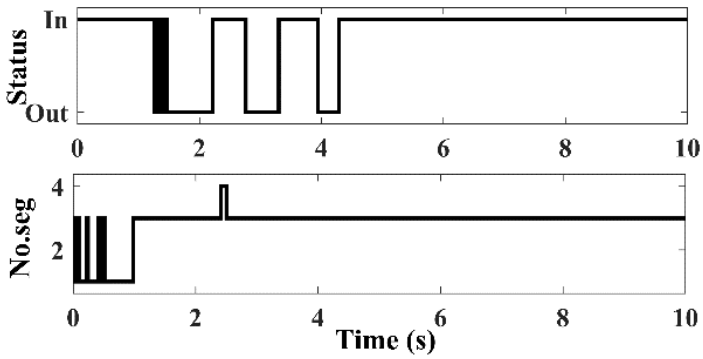

Fig. 49. Vehicle Status and the Closest Boundary Segment Number for Case 2.

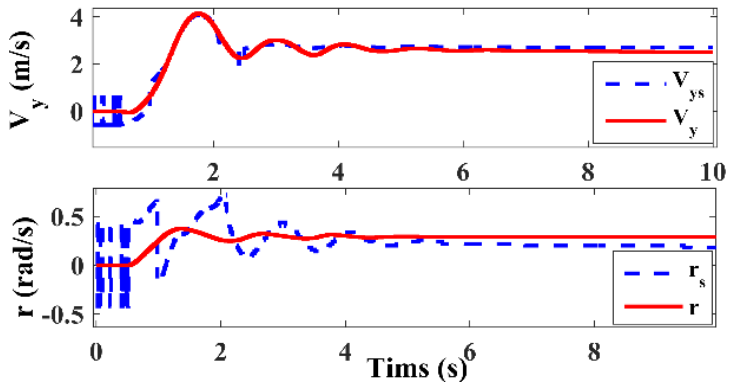

Fig. 50. Vehicle States and the Closest Point on the Boundary for Case 2.

Specifically, the vehicle states and the closest point on the boundary are compared for case 2 in Fig. 50. Corresponding to the unstable vehicle status shown in Fig. 49, V_y is larger than V_{ys} and r is smaller than r_s for some time periods between 1.5 and 4.2 seconds. Since boundary No.3 is the closest one to the vehicle state point for most of the time (Fig. 49), the vehicle states in case 2 are partially located out of the stability region according to the 3rd constraint in (79). On the contrary, as shown in Fig. 47, the vehicle states in case 3 well satisfied the 4^{th} constraints in (79). Similar explanations for Fig. 47 about the fluctuation also apply for Fig. 50.

4.5. Conclusions

In this chapter, based on the shiftable vehicle lateral stability region, a novel vehicle lateral stability control method is proposed. First, to accurately analyze the vehicle stability status based on an irregular and shiftable stability region, a projection method, the shifting vector, and the dynamic margin are proposed and integrated as one complete stability analysis method. The proposed analysis method is real-time applicable for vehicle lateral stability control. Second, based on the stability analysis results, a dynamic sliding mode

control based on the integrated AFS + DYC and AFS + ARS are designed separately. By selecting the boundaries of the stability region with the proposed dynamic margin as the sliding surfaces, the proposed vehicle lateral stability control guarantees that the vehicle trajectory is always controlled in the adopted stability region. When applying the proposed method to practical automotive applications, the tire model needs to be accurately calibrated to ensure control robustness. In addition to the dynamic SMC, the non-overshooting MPC based on four different constraints is also introduced. The characteristics of each constraint are presented and analyzed based on the simulation results of step responses for a linear and a nonlinear system. A region-based vehicle lateral stability control is designed using the proposed non-overshooting MPC. Based on the CarSim®/Simulink co-simulation results, the proposed non-overshooting MPC design is verified to successfully keep vehicle states within the stability region.

CHAPTER 5

STABILITY-GUARANTEED VEHICLE CONTROL METHODS

In this chapter, to design a more efficient stability-guaranteed vehicle controller without the chattering issues (in SMCs) and high computational demands (in MPC), the time-varying control-dependent barrier functions (CDBFs) are proposed and applied. First, some basic definitions related to CDBF and their applications to a stability-guaranteed vehicle control problem are introduced in sections 5.2 and 5.3. Then, in section 5.4, to address the discontinuous issues when the controlled invariant sets switch, the switched control barrier functions are studied and introduced. The main contents in sections 5.2 and 5.3 were published in [91], while the main contents in section 5.4 were published in [93] [5].

5.1. Overview

Vehicle stability region, or in general, the safety sets of a dynamical system, can often be described by one or multiple stability constraints. Thus, the goal of the stability-guaranteed vehicle control is to ensure all the stability constraints are satisfied at all times under any conditions [6]. To achieve such a control goal, various methods, such as model predictive control [56] and dynamic window approach [57] were proposed and evaluated. Inspired by the barrier certificate [60][61] and invariant set [58], the control barrier function (CBF) [62], is another effective method to guarantee system stability in a simpler

[5] The cited contents in section 5.2 and 5.3 are with permission of Copyright © 2021 IEEE, to be reprinted from [Huang, Yong, and Chen, *IEEE Transactions on Intelligent Vehicles*, 2021]. The cited contents in section 5.4 are with permission of Copyright © 2020 ASME, to be reprinted from [Huang and Chen, in *Proceedings of* Dynamic Systems and Control Conference, 2020].

[6] Rigorously, vehicle stability does not equal to vehicle safety. As this dissertation studies a specific stability region-based vehicle control problem, if not specified, the descriptions of "stability-guaranteed" in this dissertation can be generally understood as or extended to the meaning of "safety-guaranteed" in other related papers, e.g., [63].

and more computationally-efficient manner. Generally, the conventional CBF can be divided into two categories, namely the reciprocal CBF (RCBF) [63]-[68] and the zeroing CBF (ZCBF) [63],[74],[75]. The RCBF has an infinite value when the system states are on the set boundary, which may cause unbounded control efforts. On the other hand, the ZCBF becomes zero when the states are on the set boundary. Using CBF (either RCBF or ZCBF), control laws can be designed to ensure the system states always stay within a defined stability/safety set. Thus, the invariance of the stability/safety set, more precisely, a controlled invariant set, can be guaranteed. CBF has been utilized to solve safety control problems for autonomous ground vehicles (AGVs) and other mobile systems, such as lane-keeping [63][71], adaptive cruise control [63][71], obstacle avoidance [72], and collision-free multi-robot systems [73]. To simultaneously achieve tracking (or stabilizing) and safety control, CBF can also be integrated with control Lyapunov functions (CLF) as well as other tracking control methods [69]-[71].

To the author's best knowledge, CBF has never been used to guarantee the controlled invariance of a stability region. More importantly, since the stability region in vehicle control problems is defined by constraints that are control-dependent, the existing conventional controlled invariant set concept is not directly suitable to describe such a stability region/set, and the corresponding CBFs cannot properly resolve the associated control problems. For example, in a region-based stability control problem for AGVs, the vehicle stability set is typically defined with respect to both time-varying variables (e.g., a desired longitudinal speed and/or a reference path) and control inputs (e.g., a feedback steering angle). Based on the authors' previous study [86] and a similar observation in [10],

as the vehicle longitudinal speed and steering angle (front and/or rear) change, the size and location of the vehicle lateral stability region also change. Namely, the vehicle lateral stability region, which is selected as a controlled invariant set, is actually both time-varying and control-dependent. In this chapter, to handle the region-based stability control problem for AGVs, where the vehicle states are required to be always inside a stability region (see an example of vehicle dynamics in [94]), a novel *time-varying control-dependent* (TVCD) invariant set and the corresponding time-varying *control-dependent barrier function* (CDBF) are proposed and studied.

Notation: A continuous function $\alpha:[0,a)\to[0,\infty)$ is said to belong to class *K* if it is strictly increasing and $\alpha(0)=0$. A continuous function $\alpha:(-a,b)\to(-\infty,\infty)$ is said to belong to extended class *K* for positive *a* and *b* if it is strictly increasing and $\alpha(0)=0$ [77]. A continuous function $\sigma:[0,a)\times[0,\infty)\to[0,\infty)$ is said to belong to class *KL* if, for each fixed *s*, the mapping $\sigma(r,s)$ belongs to class *K* with respect to *r* and, for each fixed *r*, the mapping $\sigma(r,s)$ is decreasing with respect to *s* and $\sigma(r,s)\to 0$ as $s\to\infty$ [77].

In this paper, the first-order Lie derivative of a scalar function $h(x):R^n\to R$ in the direction of $f(x)=\left[f_1(x),\cdots,f_n(x)\right]^T$ is, as in [78], given by

$$L_f h(x)=\sum_{k=1}^{n} f_k(x)\frac{\partial h(x)}{\partial x_k}. \tag{80}$$

5.2. Control Barrier Functions

In this section, the concepts of invariant set and controlled invariant set are first reviewed in Definition 1 and Definition 2, respectively. Then, the definition of barrier function and control barrier function are reviewed in Definition 3 and Definition 4.

Definition 1. [58] A set $\psi \subset R^n$ is said to be *positively invariant* with respect to a nonlinear system

$$\dot{x} = f(x), \tag{81}$$

where $x \in R^n$ is the system state vector, if for any $t_0 \geq 0$ and all $x(t_0) \in \psi$, the solution $x(t) \in \psi$ for $t > t_0$.

Remark 8: The positive invariance of a set implies that the system states always remain in the set for all times. A positively invariant set is also commonly called a forward invariant set. Unless otherwise specified, we will simply refer to positively/forward invariant sets as invariant sets in the remainder of this paper as a shorthand.

Definition 2. [58] Consider a nonlinear control system of the form

$$\dot{x} = f(x,u), \tag{82}$$

where $x \in R^n$ and $u \in R^m$ are the system state and control input, respectively. The set $\psi \subset R^n$ is said to be *controlled invariant* with respect to (82), if, for any $t_0 \geq 0$ and all $x(t_0) \in \psi$, there exists a feedback control law $u = \phi(x)$, which assures the existence and uniqueness of the solution $x(t) \in \psi$ for $t > t_0$.

Remark 9: In Definition 2, although the set, ψ , is controlled to be invariant with a properly designed control u , the set itself is independent of u .

Based on the definitions of the invariant set and controlled invariant set, the corresponding BF and CBF were proposed to describe the conditions of an invariant set and a controlled invariant set, respectively [58][63]. Generally, the BF corresponding to an invariant set is defined as follows.

Definition 3. [63] Considering a nonlinear system in (81), a set ψ is defined by a continuously differentiable function $h(x): R^n \to R$ as,

$$h(x) \geq 0, x \in \psi , \tag{83}$$

$$h(x) = 0, x \in \partial\psi , \tag{84}$$

$$h(x) > 0, x \in Int(\psi), \tag{85}$$

where $\partial\psi$ and $Int(\psi)$ denote the boundary and the interior of ψ , respectively. If exists an extended class *K* function α [77], such that for all $x \in \psi$,

$$L_f h(x) \geq -\alpha(h(x)), \tag{86}$$

then the set ψ is an invariant set. $h(x)$ is called a zeroing barrier function (ZBF) [63]. The existence of ZBF is a sufficient and necessary condition for the invariance of ψ [63].

Inspired by the definition of the CBF for an affine control system in [63], the CBF for a general nonlinear control system is defined as follows.

Definition 4. (Extended from Definition 4 in [63]) Consider a nonlinear control system in (82) and a set ψ defined by (83)-(85) in Definition 3, if there exist a control u and an extended class *K* function α such that for all $x \in \psi$,

$$L_f h(x) + \alpha(h(x)) \geq 0, \tag{87}$$

then the ψ is a controlled invariant set and $h(x)$ is a ZCBF.

Note that although (86) have the same form as (87), the system function f in (87) is depicted by (82), which contains control input and thus makes (87) different from (86) when Lie derivatives are calculated.

If $h(x)$ is a CBF, any Lipschitz continuous control u that satisfies (87) will make the set ψ controlled invariant. Hence, the existence of CBF is sufficient for a set to be controlled invariant. Similar to the relationship between a BF and an invariant set, the existence of a control u and a ZCBF is both sufficient and necessary for ψ to be controlled invariant [63].

5.3. Control-Dependent Barrier Functions

5.3.1. Problem Statement and Definitions

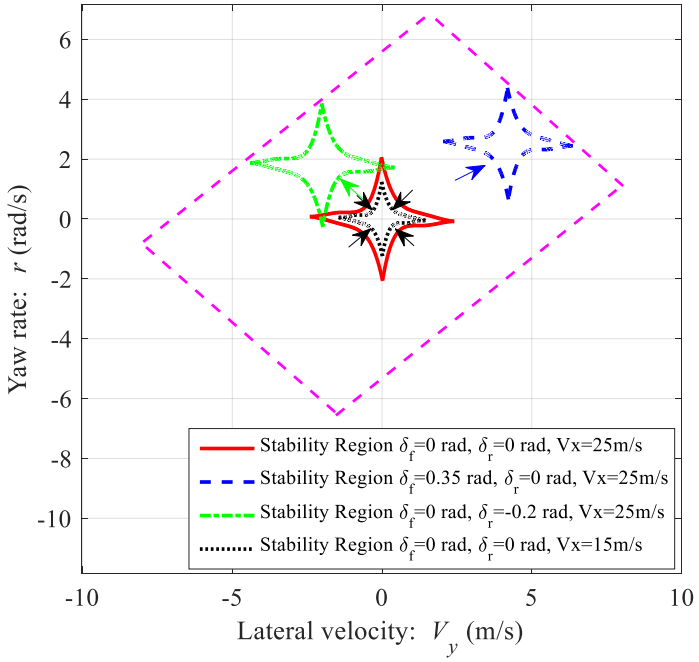

Fig. 51. Variations of the Vehicle Lateral Stability Region with Respect to Control Inputs (δ_f and/or δ_r) and Time-varying Parameters (V_x).

The (controlled) invariant set concept was usually applied to guarantee the safety of dynamic systems [63][74][76]. For control problems with safety sets defined only by system states, the controlled invariant set in Definition 2 is useful for control design. However, for control problems with safety sets defined by time-varying and control-dependent variables, the above definitions may not be applicable.

For example, in the vehicle lateral stability control problem, the control objective is to always keep vehicle states (e.g., yaw rate and lateral velocity) within an estimated or a defined stability region [17][35]. Such a stability region depicts the vehicle directional stability (e.g., neither oversteering nor too understeering) by analyzing both vehicle and tire stability [94]. In the authors' previous study [86], as shown in Fig. 51, the vehicle lateral stability region was found to shift with respect to the front (δ_f) and/or rear (δ_r)

wheel steering angles. In addition, when the longitudinal velocity (V_x) changes, the size of the stability region also changes although the shape almost remains the same. For lateral dynamics control of AGVs, the vehicle longitudinal velocity and/or the front wheel steering angle are often given by a high-level path planner as reference or feedforward signals (but not system states) that are time-varying. Meanwhile, additional front and/or rear wheel steering angles, actuated by active steering systems, are typically added as feedback control inputs. Therefore, the vehicle lateral stability region in Fig. 51, if defined or selected as an invariant set, is both time-varying and control dependent.

Remark 10: Although the specific shapes and areas of vehicle lateral stability regions in Fig. 51 were originally estimated in the author's previous work by considering both vehicle and tire stabilities [86][94], the general shrinking/expanding and shifting features of lateral stability regions with respect to steering angles and the vehicle longitudinal speed were also observed and well-documented.

Moreover, the (ground) front and rear wheel steering angles are assumed, without loss of generality, to have limits $\delta_f \in [-0.35 \text{ rad}, 0.35 \text{ rad}]$ and $\delta_r \in [-0.2 \text{ rad}, 0.2 \text{ rad}]$, respectively, and the maximum vehicle longitudinal speed is $V_x = 25$ m/s (these parameters can be easily changed to get different stability regions). Thus, an extended envelope of stability regions can be defined by the area outlined by pink dashed lines in Fig. 51 based on the stability region shifting and shrinking/expanding feature, no matter how the steering angles and longitudinal speed change within the limits. This enveloped area, as a set consisting of all the possible stability regions, is a time-invariant and control-independent set, which could be described by the existing concept of the controlled invariant set in

Definition 2. However, the invariance of the whole enveloped area does not necessarily imply the invariance of the shifted and shrunk/expanded stability regions as the subsets, which are discussed more in Remark 4. Therefore, to describe such an invariance set that is time-varying and control-dependent, a new concept is introduced as follows.

Definition 5. Consider a nonlinear control system in (82), a set $\psi(u,t) \subset R^n$ is said to be time-varying and control-dependent (TVCD) invariant if there exist a control $u \in U$ and a $u_0 \in U$ such that for any $t_0 \geq 0$ and all $x(t_0) \in \psi(u_0,t_0)$, $x(t) \in \psi(u,t)$ for all $t \in T = [t_0, t_{end})$, where $U \subset R^m$ is the vector space of all the feasible set of u.

Remark 11: In Definition 5, $T = [t_0, t_{end})$ is the maximum time interval that the set can be guaranteed to be TVCD invariant. Note that for any time intervals in T, if the controlled invariant set does not change with time, a TVCD invariant set becomes a control-dependent invariant set. For the set $\psi(u,t)$ in Definition 5, a set $\psi = \bigcup_{u \in U,\, t \in T} \psi(u,t)$, which is a union of all the possible $\psi(u,t)$ for any $u \in U$ and $t \in T$, could be a controlled invariant set with a properly designed control u [74][76]. However, since the $\psi(u,t)$ is a subset of ψ, a control u, which makes ψ controlled invariant, does not necessarily make the subset $\psi(u,t)$ TVCD invariant. On the contrary, a control u, which makes each subset $\psi(u,t)$ TVCD invariant, can sufficiently make the set ψ controlled invariant since $\psi(u,t) \subseteq \psi$. Therefore, the determination of the control u that makes the set $\psi(u,t)$ TVCD invariant is different from the determination of u in Definition 2.

Following the definition of BF and CBF, the corresponding definition of a time-varying CDBF for the newly defined TVCD invariant set in Definition 5 is presented as follows.

Definition 6. Consider a nonlinear control system in (82), where u is differentiable with a Lipschitz continuous $\dot{u}$, e.g. $\dot{u} = \omega$ and $\omega \in \Omega(u)$, $\Omega \subset R^m$. Let u be a new system state, then the system is augmented as

$$\dot{x} \triangleq \begin{bmatrix} \dot{x} \\ \dot{u} \end{bmatrix} = \begin{bmatrix} f(x,u) \\ \omega \end{bmatrix} = f(x,\omega), \tag{88}$$

where $x = \begin{bmatrix} x^T & u^T \end{bmatrix}^T$. For a TVCD set $\psi(u,t)$, $u \in U, t \in T$ (in Definition 5) defined by a continuous and differentiable function $h(x,t)$ as

$$h(x,t) \geq 0, \forall x \in \psi(u,t), \tag{89}$$

$$h(x,t) = 0, \forall x \in \partial\psi(u,t), \tag{90}$$

$$h(x,t) > 0, \forall x \in Int(\psi(u,t)), \tag{91}$$

if there exist a control $u \in U$, where $\dot{u} \in \Omega$, and an extended class *K* function α such that for all $x \in \psi(u,t)$,

$$L_f h(x,t) + \alpha(h(x,t)) \geq 0, \tag{92}$$

where

$$L_f h(x,t) = \sum f(x) \frac{\partial h(x,t)}{\partial x,t} = \frac{\partial h(x,t)}{\partial x}^T \dot{x} + \frac{\partial h(x,t)}{\partial u}^T \dot{u} + \frac{\partial h(x,t)}{\partial t}, \tag{93}$$

then the set $\psi(u,t)$ is a TVCD invariant set. $h(x,t)$ is a time-varying zeroing control-dependent barrier function (ZCDBF). Moreover, the solution $x(t)$, $u(t)$ exists and is unique by Peano's Theorem [111].

Remark 12: When the invariance conditions in (93) are applied in the optimization problem, $\dot{u}$ is suggested to be the auxiliary control variable and u can be obtained by integrating $\dot{u}$, i.e., we are introducing integral control action. The reasons are two-fold. First, by selecting $\dot{u}$ as the control variable, the continuity and differentiability of the formal control u can be guaranteed. Second, if u is selected as the control variable in optimization, $\dot{u}$ should be determined in advance or bounded to avoid extreme values, which may violate the invariance conditions in (92). In addition, by comparing with the author's previous study [91] that selects u as the control variable, it was found that its control performance is limited and conservative because the variable $\dot{u}$ in (93) was simply replaced by their upper and lower limits in [91]. Therefore, $\dot{u}$ is suggested to be the control variable in CDBF. $\Omega(u)$ is defined as control-dependent to ensure $u \in U$. Equations (127) and (128) are illustrative examples to further clarify the selection of $\Omega(u)$.

Proposition 1. Given a nonlinear control system in (88) and a TVCD set defined by (89)-(91), if there exists a time-varying ZCDBF $h(x,t)$ defined on the set $\psi(u,t)$ in Definition 6, then $\psi(u,t)$ is a TVCD invariant set.

Proof. Based on the definition of the tangent cone [126] and Nagumo's theorem [58], the invariance condition in (92) indicates that when $x \in \partial\psi$, the derivative $\dot{x}$ points inside or is tangent to ψ [58], then the trajectory $x(t)$ remains in ψ. Thus, if the system state is initially in the set, it then follows that the system state is always kept inside the set and $h(x,t) > 0$. According to (89), if $h(x,t) \geq 0$, $x \in \psi(x,t)$ for all $u \in U$ and $t \in T$ is proved, which indicates that the $\psi(x,t)$ is a TVCD invariant set. ■

Remark 13: The condition in (92) to make $\psi(u,t)$ TVCD invariant is more general than the condition in (87), which only makes ψ controlled invariant. The definition of the time-varying CDBF is different from the concept of time-varying CBF (TCBF) in the literature since the control input determined by the time-varying CDBF also has impacts on the safety constraints. Differently, in TCBF, the safety constraints could be time-varying but remain unchanged with respect to different control inputs. One can easily verify that if $h(x,t)$ is independent of u and time-invariant, the term $\frac{\partial h(x,t)}{\partial u}^T$ and $\frac{\partial h(x,t)}{\partial t}$ in (93) are eliminated. Thus, (92) are reduced to the same forms as those in (87). To make the control-dependent feature valid, $\frac{\partial h(x,t)}{\partial u}^T$ in Definition 6 is assumed to be non-zero.

For a TVCD set described by (89)-(91), any control that satisfies the constraints (92) in Definition 6 will make the TVCD set invariant. Thus, a quadratic programming (QP) problem can be formulated to find a control derivative $\dot{u}$ (and the corresponding control u by integration) that satisfy one or multiple invariance constraints [74]. Since the QP is linear with respect to $\dot{u}$, the algorithm is real-time implementable without additional computational effort.

Note that although the proposed new concepts on the TVCD invariant set and time-varying CDBF are inspired from AGVs, these new concepts and theoretical work, including Proposition 1, are generally applicable to any other dynamic systems ((82) or (88)), whose safety or stability regions (constraints) are varying with respect to control and time. On that note, the vehicle dynamics and application are introduced in the next section.

5.3.2. Vehicle Stability Control using CDBF

For a four-wheel steering (4WS) vehicle equipped with two steer-by-wire systems, the steering angles of the front and rear wheels can be separately controlled by two steering motors. In this study, an AGV with a 4WS system is considered, in which both the front and rear wheel steering systems are adopted as the actuators (control inputs) to guarantee vehicle lateral stability (analogous to a safety specification). Selecting the lateral velocity and yaw rate as two system states, the single-track model of vehicle lateral dynamics, as shown in (94), is written as

$$\begin{aligned} \dot{V}_y + V_x r &= \left(F_{yf} \cos\left(\delta_f + \delta_{AFS} \right) + F_{yr} \cos \delta_r \right) \Big/ m_v \\ \dot{r} &= \left(l_f F_{yf} \cos\left(\delta_f + \delta_{AFS} \right) - l_r F_{yr} \cos \delta_r \right) \Big/ I_z \end{aligned}, \tag{94}$$

where m_v, I_z, δ_f, δ_{AFS}, and δ_r are the vehicle mass, yaw moment inertia, feedforward front steering angle, and feedback front and rear steering angle, respectively. V_x, V_y, and r are the vehicle longitudinal velocity, lateral velocity, and yaw rate, respectively. l_f and l_r are the front and rear wheelbase, respectively. F_{yf} and F_{yr} are the lateral forces of front and rear tires, which are calculated based on a nonlinear LuGre tire model in section 2.2. To calculate the lateral tire forces by the tire model, the tire slip angles are calculated in (95) and (96):

$$\alpha_f = \left[\delta_f(t) + \delta_{AFS} \right] - \tan^{-1}\left(\left(V_y + l_f \cdot r \right) \Big/ V_x(t) \right), \tag{95}$$

$$\alpha_r = \delta_r - \tan^{-1}\left(\left(V_y - l_r \cdot r \right) \Big/ V_x(t) \right), \tag{96}$$

where $\delta_f(t)$ and $V_x(t)$ are time-varying, given by either a driver or an upper-level feedforward control. The two feedback control inputs are selected as $u_1 = \delta_{AFS}$ and $u_2 = \delta_r$.

To describe the region-based vehicle lateral stability control problem using the proposed time-varying CDBF, the boundaries of the stability region are first formulated. In Fig. 51, taking the region depicted by the solid red curves as the stability set, which is estimated at a zero steering angle and a constant longitudinal velocity, the corresponding four boundaries are described by four independent functions as

$$h_1(x) = b_1(V_y) - r, \tag{97}$$

$$h_2(x) = b_2(V_y) - r, \tag{98}$$

$$h_3(x) = r - b_3(V_y), \tag{99}$$

$$h_4(x) = r - b_4(V_y), \tag{100}$$

where b_1, b_2, b_3, b_4 are the polynomial functions to describe the boundaries as $r = b_j(V_y), j = 1,2,3,4$. However, the safety set defined by (97)-(100) is not enough to describe dynamic characteristics of the vehicle lateral stability region. Based on the authors' previous work [86], the region-based vehicle lateral stability control problem involves time-varying and control-dependent features, which are from the following two sources. First, when the front and rear steering angles are applied, the vehicle lateral stability region shifts along with specific directions [86], which is formulated in a shifting vector as

$$\vec{S} = \left[s_1(\delta_f(t), V_x(t), u_1, u_2) \quad s_2(\delta_f(t), V_x(t), u_1, u_2) \right]^T, \tag{101}$$

where

$$s_1\left(\delta_f(t), V_x(t), u_1, u_2\right) = \frac{V_x(t)\left[l_r\left(\delta_f(t)+u_1\right)+l_f u_2\right]}{l_f+l_r}, \tag{102}$$

$$s_2\left(\delta_f(t), V_x(t), u_1, u_2\right) = \frac{V_x(t)\left[\left(\delta_f(t)+u_1\right)-u_2\right]}{l_f+l_r}. \tag{103}$$

Second, when the vehicle longitudinal velocity decreases or increases, the size of the stability region shrinks or expands correspondingly. Using the stability region estimated at $V_x = 25$ m/s as a reference, a scaling function is derived to describe the size variation when V_x changes. Based on the characteristics of the stability region boundaries, the scaling functions are formulated separately for the different boundary pairs as shown in (104).

$$a_i\left(V_x(t)\right) = \begin{cases} k_1\left(V_x(t)-25\right) & i=1,3 \\ k_2\left(V_x(t)-25\right) & i=2,4 \end{cases}, \tag{104}$$

where k_1 and k_2 are the scaling factors. If $V_x < 25$ m/s, the stability region shrinks to be smaller (e.g. the region depicted by the black dot curves in Fig. 51) than the reference region, and if $V_x > 25$ m/s, the stability region expands to be larger than the reference region. Note that the above time-varying feature is realized by setting the system parameters as time-varying variables. In more general cases, the stability/safety set can be explicitly dependent on time-varying variables.

Based on both the shifting vector and the scaling function, the four boundaries in (97)-(100) are reformulated as four time-varying and control-dependent functions in (105)-(108).

$$h_1(x,u,t) = b_1\left(\left(V_y - s_1\right)\right) - \left(r - s_2\right) + a_1\left(V_x(t)\right), \tag{105}$$

$$h_2(x,u,t) = b_2\left(\left(V_y - s_1\right)\right) - \left(r - s_2\right) + a_2\left(V_x(t)\right), \tag{106}$$

$$h_3(x,u,t) = (r - s_2) - b_3\left(\left(V_y - s_1\right)\right) + a_3\left(V_x(t)\right), \tag{107}$$

$$h_4(x,u,t) = (r - s_2) - b_4\left(\left(V_y - s_1\right)\right) + a_4\left(V_x(t)\right). \tag{108}$$

To sum up the problem description, since the shifting vector in (101) consists of two time-varying variables (δ_f and V_x) and two control inputs (u_1 and u_2), and the scaling function in (104) contains one time-varying variable (V_x), the guaranteed vehicle stability control problem using the stability region depicted in (105)-(108) is based on a typical TVCD invariant set as described in Definition 5. To resolve this control problem, the vehicle dynamic model in (94) is first augmented with the state vector as $x = \begin{bmatrix} V_y & r & u_1 & u_2 \end{bmatrix}^T$,

$$\dot{x} = \begin{bmatrix} \dot{V}_y & \dot{r} & \dot{u}_1 & \dot{u}_2 \end{bmatrix}^T = \begin{bmatrix} f_1(x) & f_2(x) & \omega_1 & \omega_2 \end{bmatrix}^T, \tag{109}$$

where f_1 and f_2 are the vehicle dynamics in (94), ω_1 and ω_2 are the control input dynamics that will be determined and discussed later.

Based on Definition 6, the vehicle stability region is defined as a TVCD invariant set C as follows

$$C = \left\{ x \in R^2 \,\middle|\, h_j(x,t) \geq 0,\ j = 1,2,3,4 \right\}, \tag{110}$$

$$\partial C = \left\{ x \in R^2 \,\middle|\, h_j(x,t) = 0,\ j = 1,2,3,4 \right\}, \tag{111}$$

$$Int(C) = \left\{ x \in R^2 \,\middle|\, h_j(x,t) > 0,\ j = 1,2,3,4 \right\}. \tag{112}$$

Then, the set invariance conditions using the time-varying ZCDBF in (92) with respect to the stability region boundary functions in (105)-(108) are given by the following four constraints:

$$L_f h_j(x,t) + \alpha_j\left(h_j(x,t)\right) \geq 0,\ j = 1,2,3,4, \tag{113}$$

where

$$L_f h_j(x,t) = \frac{\partial h_j(x,t)}{\partial V_y}\dot{V}_y + \frac{\partial h_j(x,t)}{\partial r}\dot{r} + \frac{\partial h_j(x,t)}{\partial u_1}\omega_1 + \frac{\partial h_j(x,t)}{\partial u_2}\omega_2 + \frac{\partial h_j(x,t)}{\partial t} \tag{114}$$
$$j = 1,2,3,4.$$

Without loss of generality, assume the boundary functions $r = b_j\left(V_y\right), j = 1,2,3,4$ are depicted by four linear functions as $r = b_j V_y + c_j, j = 1,2,3,4$, where c_j are constants. Then, by substituting the shifting function in (101) and the scaling function in (104) into (105)-(108), the complete forms of the four time-varying and control-dependent boundary functions are rewritten as

$$\begin{aligned} h_1(x,t) = b_1 V_y - r + \left[\frac{\left(1-b_1 l_r\right)}{l_f + l_r}V_x(t)\right]u_1 + \left[\frac{\left(-1-b_1 l_f\right)}{l_f + l_r}V_x(t)\right]u_2 \\ + \frac{\left(1-b_1 l_r\right)}{l_f + l_r}\delta_f(t)V_x(t) + a_1\left(V_x(t)\right) \end{aligned}, \tag{115}$$

$$\begin{aligned} h_2(x,t) = b_2 V_y - r + \left[\frac{\left(1-b_2 l_r\right)}{l_f + l_r}V_x(t)\right]u_1 + \left[\frac{\left(-1-b_2 l_f\right)}{l_f + l_r}V_x(t)\right]u_2 \\ + \frac{\left(1-b_2 l_r\right)}{l_f + l_r}\delta_f(t)V_x(t) + a_2\left(V_x(t)\right) \end{aligned}, \tag{116}$$

$$h_3(x,t) = -b_3 V_y + r + \left[\frac{(1-b_3 l_r)}{l_f + l_r} V_x(t)\right] u_1 + \left[\frac{(-1-b_3 l_f)}{l_f + l_r} V_x(t)\right] u_2 + \frac{(b_3 l_r - 1)}{l_f + l_r} \delta_f(t) V_x(t) + a_3(V_x(t)) \quad (117)$$

$$h_4(x,t) = -b_4 V_y + r + \left[\frac{(1-b_4 l_r)}{l_f + l_r} V_x(t)\right] u_1 + \left[\frac{(-1-b_4 l_f)}{l_f + l_r} V_x(t)\right] u_2 + \frac{(b_4 l_r - 1)}{l_f + l_r} \delta_f(t) V_x(t) + a_4(V_x(t)) \quad (118)$$

Taking the first boundary function $h_1(x,t)$ in (115) as an example, the partial derivatives of $h_1(x,t)$ in (114) are

$$\frac{\partial h_1(x,t)}{\partial V_y} = b_1, \quad (119)$$

$$\frac{\partial h_1(x,t)}{\partial r} = -1, \quad (120)$$

$$\frac{\partial h_1(x,t)}{\partial u_1} = \frac{(1-b_1 l_r)}{l_f + l_r} V_x(t), \quad (121)$$

$$\frac{\partial h_1(x,t)}{\partial u_2} = \frac{(-1-b_1 l_f)}{l_f + l_r} V_x(t), \quad (122)$$

$$\frac{\partial h_1(x)}{\partial t} = \frac{(1-b_1 l_r) u_1}{l_f + l_r} \dot{V}_x(t) + \frac{(-1-b_1 l_f) u_2}{l_f + l_r} \dot{V}_x(t) + \frac{(1-b_1 l_r)}{l_f + l_r} \left(\dot{V}_x(t) \delta_f(t) + V_x(t) \dot{\delta}_f(t)\right) + \dot{a}_1(V_x(t)) \quad (123)$$

Substituting (119)-(123) into (114) gives,

$$
\begin{aligned}
L_f h_1(x,t) = \; & b_1 f_1(x) + (-1) f_2(x) + \left(\frac{V_x(t)(1-b_1 l_r)}{l_f + l_r} \right) \omega_1 \\
& + \left(\frac{V_x(t)(-1-b_1 l_f)}{l_f + l_r} \right) \omega_2 + \dot{a}_1 \left(V_x(t) \right) \\
& + \frac{(1-b_1 l_r)}{l_f + l_r} \left(\dot{V}_x(t) \delta_f(t) + V_x(t) \dot{\delta}_f(t) \right) \quad . \\
& + \frac{(1-b_1 l_r) u_1}{l_f + l_r} \dot{V}_x(t) + \frac{(-1-b_1 l_f) u_2}{l_f + l_r} \dot{V}_x(t)
\end{aligned}
\tag{124}
$$

The final constraint for $h_1(x,t)$ is obtained by substituting (124) into (113). For the other three boundary functions $h_j(x,t), j = 2,3,4$, the same procedure can be applied.

As described in Proposition 1, the control design, which ensures that the inequalities in (113) are always satisfied, can guarantee system stability/safety. The key issue of solving this guaranteed stability control problem is the determination ω_1 and ω_2 in (124). Instead of directly applying u_1 and u_2 as the control inputs, we consider ω_1 and ω_2 as the virtual control inputs, which, by integration, will give u_1 and u_2 as the real control inputs of the vehicle lateral dynamics in (94). Note that in addition to the constraint derived for the first boundary function as an example, the determination of ω_1 and ω_2 should also satisfy the constraints derived with respect to the other three boundary functions in (116)-(118).

Based on the complete constraints that guarantee the vehicle lateral stability, a QP problem is formulated to calculate the optimal virtual control inputs. Specifically, for a given stability region as a TVCD set, the four time-varying CDBFs and the corresponding constraints can be integrated with a QP problem as follows.

$$\dot{u}(x,t) = \underset{\dot{u}\in R^2}{\operatorname{argmin}} \frac{1}{2}\dot{u}^T H\dot{u} + F^T\dot{u}\,, \tag{125}$$

s.t.

$$\frac{\partial h_j(x,t)}{\partial x} f(x) + \sum_{j=1}^{4} \frac{\partial h_j(x,t)}{\partial u}\dot{u} + \frac{\partial h_j(x,t)}{\partial t} + \alpha_j\left(h_j(x,t)\right) \geq 0,\ j = 1,2,3,4\,, \tag{126}$$

$$\dot{u}_1 \in \Omega_1(u_1) = [\dot{u}_{1,\min}, \dot{u}_{1,\max}],\ \dot{u}_2 \in \Omega_2(u_2) = [\dot{u}_{2,\min}, \dot{u}_{2,\max}], \tag{127}$$

$$\begin{aligned} &\dot{u}_{1,\max} = 0,\ if\ u_1 = u_{1,\max}, \\ &\dot{u}_{1,\min} = 0,\ if\ u_1 = u_{1,\min}, \\ &\dot{u}_{2,\max} = 0,\ if\ u_2 = u_{2,\max}, \\ &\dot{u}_{2,\min} = 0,\ if\ u_2 = u_{2,\min}, \end{aligned} \tag{128}$$

where $\dot{u} = \begin{bmatrix}\dot{u}_1 & \dot{u}_2\end{bmatrix}^T = \begin{bmatrix}\omega_1 & \omega_2\end{bmatrix}^T$ denotes the virtual control inputs, $\dot{u}_{1,\max} = \dot{u}_{2,\max} = \frac{T_{\max}}{I_S}$ and $\dot{u}_{1,\min} = \dot{u}_{2,\min} = -\dot{u}_{1,\max}$ in (127), $H \in R^{2\times 2}$ is positive definite, and $F \in R^2$. Note that in (126), the constraints are written with respect to the virtual control inputs, where the real control u_1 and u_2 are treated as the state variables. α_j are appropriately selected class *K* functions based on the sharing property among multiple CBFs [74]. The sharing property ensures the feasibility of the QP problem when multiple invariance conditions are applied. Note that, the constraints in (127) and (128) are not considered in the sharing property but simply considered as the upper and lower bounds of the control input. Specifically, the constraints in (127) denote the upper and lower limits of $\dot{u}$, which, in practice, are the steering rate bounds determined by the maximum torque of the steering motor $T_{\max}$ and the moment of inertia of the steering system I_S. The constraints in (128) ensure $u_1 \in U_1$ and $u_2 \in U_2$, where $U_1 = \left[u_{1,\min}, u_{1,\max}\right]$ and $U_2 = \left[u_{2,\min}, u_{2,\max}\right]$ denote the feasible control

input sets. For vehicle systems, such feasible sets can be determined by the mechanical structures of steering systems.

Remark 14. (Proof of feasibility): Following the feasibility discussions in [75], the optimization in (125)-(128) is feasible if the vector field of system dynamics in (94) and the TVCDBF in (115)-(118) are locally Lipschitz with the assumption of non-zero V_x. The feasibility can also be guaranteed based on the sharing property among multiple invariant constraints [74]. As shown in Table 7, the Class *K* functions for h_1 and h_3 are selected as the same and the Class *K* functions for h_2 and h_4 are selected as the same. For the boundaries that have an intersection (e.g., h_2 and h_3), different class *K* functions are selected. The system dynamics, barrier functions, and Class *K* functions adopted in this paper satisfy the required conditions. Therefore, the feasibility of QP in (125)-(128) can be guaranteed.

After the optimal virtual control $\dot{u}$ are obtained, the real control inputs u are then determined by integration. It is also worth noting that by integrating $\dot{u}_1$ and $\dot{u}_2$, we have u_1 and u_2 at the current time, which gives us a priori information to decide whether or not to include any of the constraints in (128). Hence, the problem is still a QP at run-time. Finally, for vehicle systems, u_1 is typically combined with δ_f as the total front wheel steering angle. A framework of the proposed guaranteed vehicle lateral stability control using time-varying CDBF is shown in Fig. 52.

Table 7. Parameters of Quadratic Programming Controller

Symbol	Parameters	Values
m_v	Vehicle mass	1270 kg
I_z	Yaw inertia	1500 kg·m^2
l_f	Front wheelbase	1.11 m
l_r	Rear wheelbase	1.8 m
$\alpha_1(x)$ & $\alpha_3(x)$	Class K function	$20x$
$\alpha_2(x)$ & $\alpha_4(x)$	Class K function	$100x$
k_1	Scaling factor	0.024
k_2	Scaling factor	0.028
H	Weighting matrix	$\begin{bmatrix} 50 & 0 \\ 0 & 50 \end{bmatrix}$
F	Weighting matrix	$\begin{bmatrix} 0 & 0 \end{bmatrix}$
T_{max}	Maximum steering torque	24 Nm
$u_{1,min/max}$	Min/Max front wheel steering angle	±0.6rad(34°)
$u_{2,min/max}$	Min/Max rear wheel steering angle	±0.1rad(5.7°)
I_s	Moment of inertia of the steering system	3 kgm^2
ε	Slack number	0.01
k	Bounds on disturbances	0.1

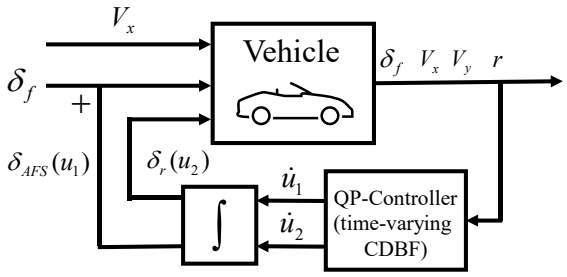

Fig. 52. Framework of Vehicle Lateral Stability Control.

Note that during the QP implementation for the sampled system, signal delays due to the sampling may occur. Such delays could cause a short period of CDBF violation, especially when the system states are controlled close to the boundaries of the stability set. To solve this issue, in (92), a small positive slack number ε could be added to the time-varying CDBF in the extended class K function as $\alpha\left(h\left(x,t\right)-\varepsilon\right)$. The slack number ε can

be also applied to overcome possible robustness issues in practical applications. In [75], it was found that if the disturbance is vanishing or sufficiently small, the control barrier function can still guarantee the set invariance. For any bounded disturbance (e.g., $\|g\|_\infty \le k$), by adding k to the slack number ε, set invariance can be robustly guaranteed. Although the value of k could be difficult to find *a priori* for a general disturbance, it can be estimated for specific systems and operation conditions, such as vehicle systems [112].

5.3.3. Simulation and Discussions

In this section, the proposed new definitions and the corresponding vehicle stability control design are verified through simulation results of high-speed J-turn and double lane change (DLC) maneuvers. The vehicle parameters shown in Table 7 are selected based on the database of a C-class hatchback vehicle model in CarSim. To ensure the feasibility of the QP problem (125)-(128), the selected Class *K* functions in Table 7 were verified by the sharing property in [15]. Specifically, as shown in Table 7, the Class *K* functions for h_1 and h_3 are selected as the same and the Class *K* functions for h_2 and h_4 are selected as the same. The reason for this selection is, for h_1 and h_3, the corresponding stability region boundaries do not have intersections (the upper left and lower right boundaries of any of the three regions in Fig. 51), which reduces the possibility of conflicts. For the boundaries that have an intersection (e.g., h_2 and h_3), different Class *K* functions are selected. The real-time feasibility of the proposed control method for both scenarios below was verified by implementing the proposed control algorithm on a real vehicle test platform equipped with a dSPACE MicroAutobox II, where we observed that the computations can be

completed in real-time without delays when the main processor runs at a 900MHz clock frequency.

5.3.3.1.High-speed J-turn maneuver

Two simulation cases are conducted and compared to demonstrate the effectiveness of the control design based on the proposed time-varying CDBF. Given the same steering and longitudinal velocity profile, the first case simulates the vehicle driving behavior based on the feedforward steering angle δ_f. The second case simulates the feedback vehicle control with the guaranteed vehicle stability control design. The feedforward front wheel steering angle δ_f and the longitudinal velocity V_x are given in Fig. 53 as the time-varying variables. Specifically, the time-varying functions of $\delta_f(t)$ and $V_x(t)$ are given as

$$\delta_f(t)=\begin{cases}0.2t-0.1\ rad & \\ 0.2\ rad & , \\ -0.2t+1.9\ rad & \end{cases} \quad V_x(t)=\begin{cases}-10t+30\ m/s & 0.5<t\le 1.5\\ 15\ m/s & 1.5<t\le 8.5\\ 10t-70\ m/s & 8.5<t<9.5\end{cases}. \tag{129}$$

Note that when the vehicle inputs are zeros, the proposed control design will not be applied since there will be no vehicle movements, e.g., $V_x(t)=0$. In this simulation, the tire-road friction coefficient is set to 0.85 for road conditions to ensure sufficient friction forces.

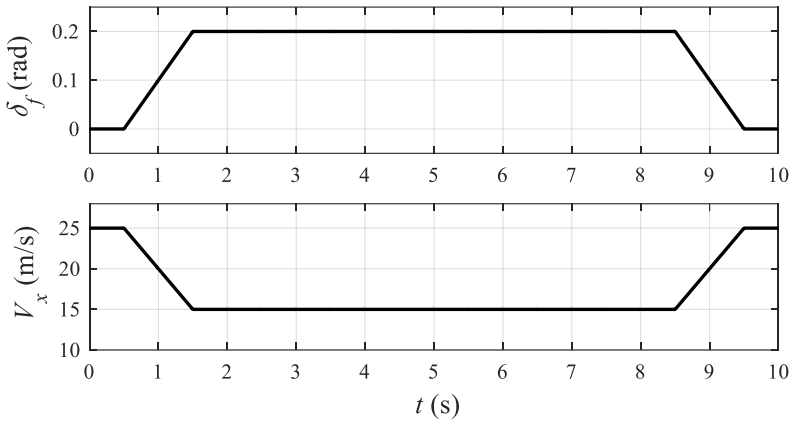

Fig. 53. Time-varying Profiles (the Front Wheel Steering Angle and the Longitudinal Velocity) in the J-turn Maneuver.

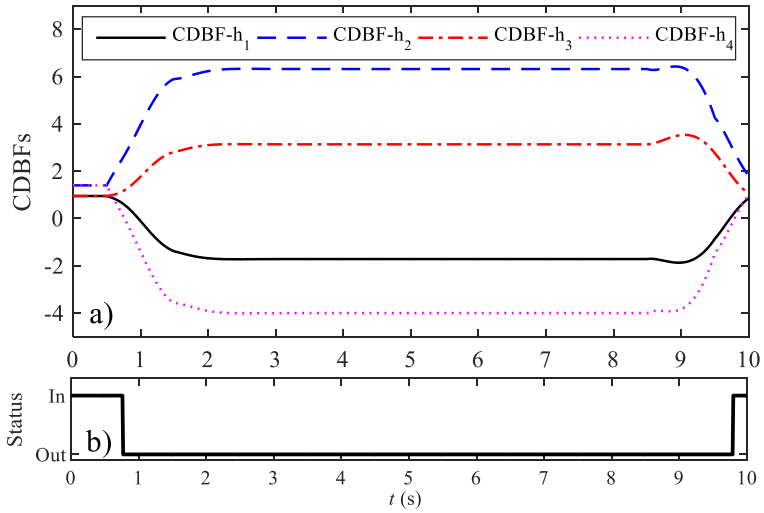

Fig. 54. Feedforward Case Simulation Results in the J-turn Maneuver, a) CDBFs Values, b) Vehicle Stability Status.

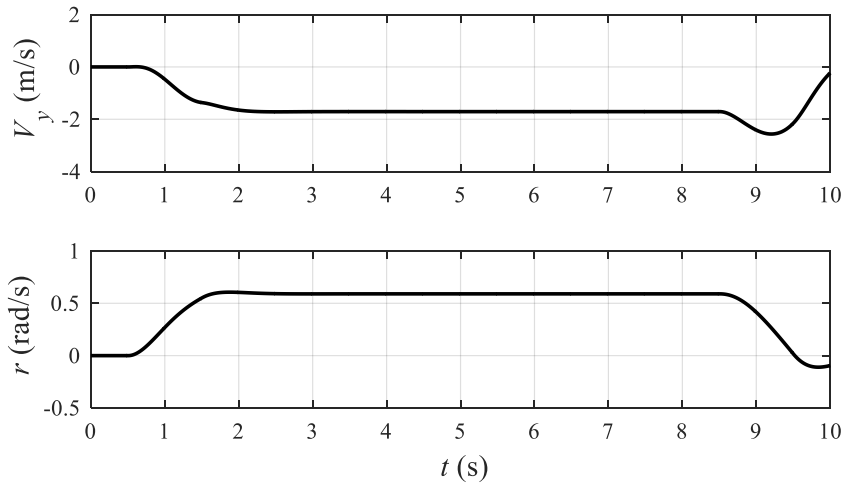

Fig. 55. Vehicle States in the J-turn Maneuver: Feedforward Control.

In the first case, the feedback control inputs are all zeros, namely, $u_1 = u_2 = 0$. Thus, the stability region is time-varying with respect to the feedforward steering angle and vehicle longitudinal speed. As shown in Fig. 54 a), the negative time-varying CDBF values are clearly observed for h_1 and h_4, which indicate that the system states are not kept in the defined TVCD invariant (stability) set, as described in Definition 6. The corresponding unstable statuses are also verified by the vehicle status check results, shown in Fig. 54 b). The vehicle status "in" or "out" the TVCD stability set in Fig. 54 b) is checked by whether the instantaneous vehicle states are located in the TVCD stability region, which is an independent evaluation process based on the instantaneous check of state and region locations in the phase plane [86]. Moreover, the vehicle states (V_y and r) are shown in Fig. 55 for the J-turn maneuver, with relatively large values.

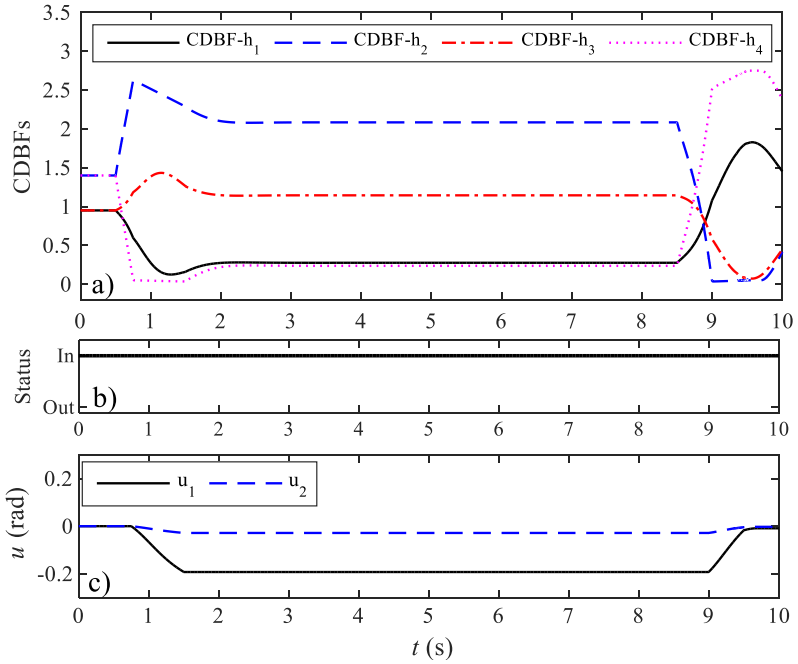

Fig. 56. Feedback Case Simulation Results in the J-turn Maneuver, a) CDBFs Values, b) Vehicle Stability Status, c) Control Inputs.

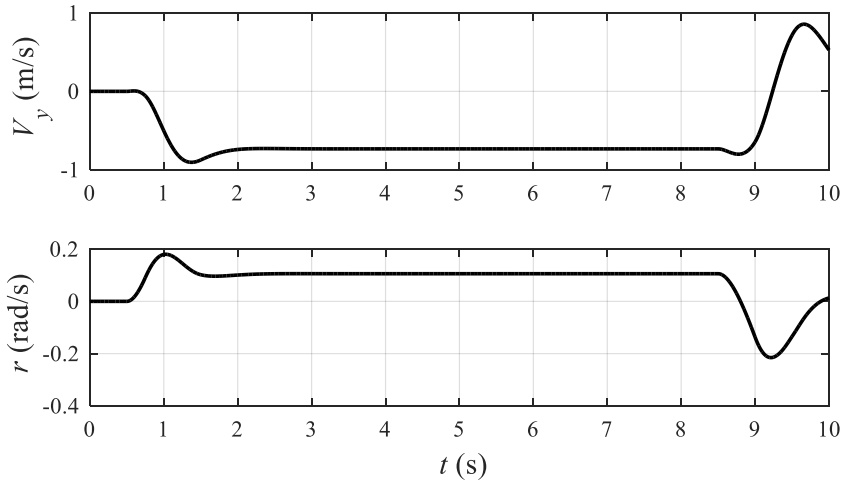

Fig. 57. Vehicle States in the J-turn Maneuver: Feedback Control.

In the second case, the feedback front and rear wheel steering angles are calculated in the QP problem with respect to the constraints derived from the proposed time-varying CDBFs. As shown in Fig. 56 a), all the four time-varying CDBFs are well controlled to be positive during the whole maneuver, which indicates that the vehicle states are always in

the TVCD stability region. Since the vehicle stability region is both time-varying and control-dependent, the control design based on the proposed time-varying CDBF is verified. In Fig. 56 b), the vehicle status check always shows 'in' status for the whole maneuver, which is consistent with the meaning of positive time-varying CDBF values. In Fig. 56 c), the rear wheels are slightly steered to the same direction of the front wheels to keep the vehicle stable, which demonstrates the same idea that the rear wheels should turn to the same direction of the front wheels to keep a 4WS vehicle stable at high speeds [113]. In addition, by comparing the vehicle states in Fig. 57 with those in Fig. 55, V_y and r for the feedback control case are both smaller than those in the feedforward case, which indicates a more stable and safer vehicle status. Such a stability improvement can also be demonstrated by comparing the vehicle planar trajectories between these two cases. As shown in Fig. 58, the vehicle trajectory in the feedback case is much less extreme than that of the feedforward case, which could easily cause the vehicle to spin or collide with other vehicles. In Fig. 58, the desired trajectory is the path of a vehicle with an ideal tire model when the same feedforward traces in Fig. 58 are given. The tire cornering stiffness coefficients in a linear tire model are calibrated based on the nonlinear tire model in section 2.2. From the comparison shown in Fig. 58, the vehicle trajectory of feedback case with CDBF is much closer to the desired trajectory, also indicating a better vehicle driving performance.

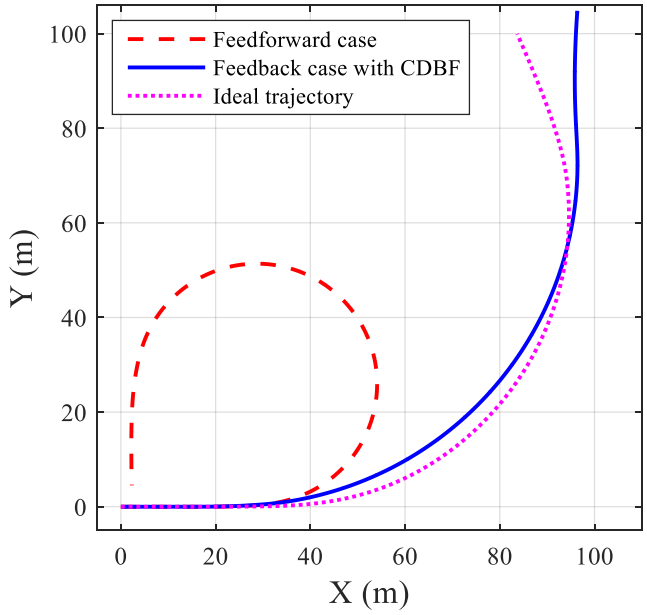

Fig. 58. Vehicle Trajectories Comparison in the J-turn Maneuver.

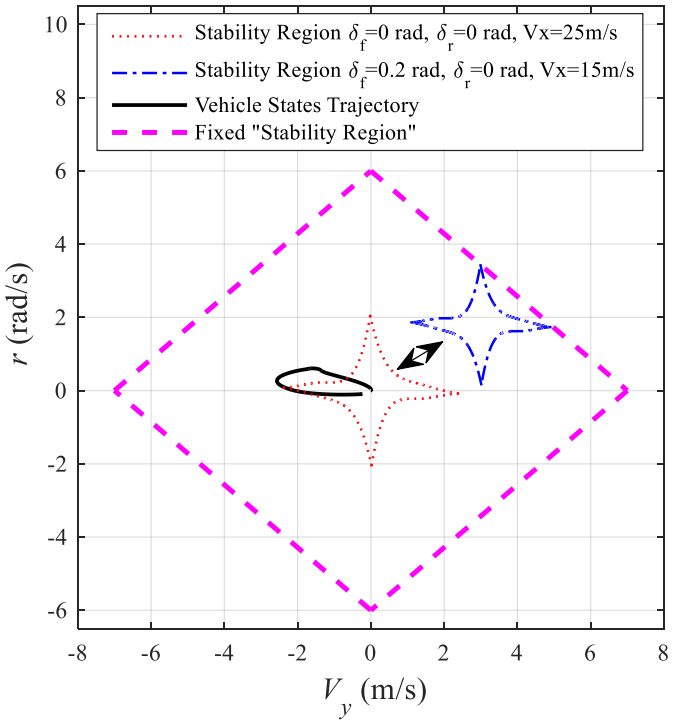

Fig. 59. Vehicle State Trajectory with Regard to the Fixed “Stability Region” in the J-turn Maneuver.

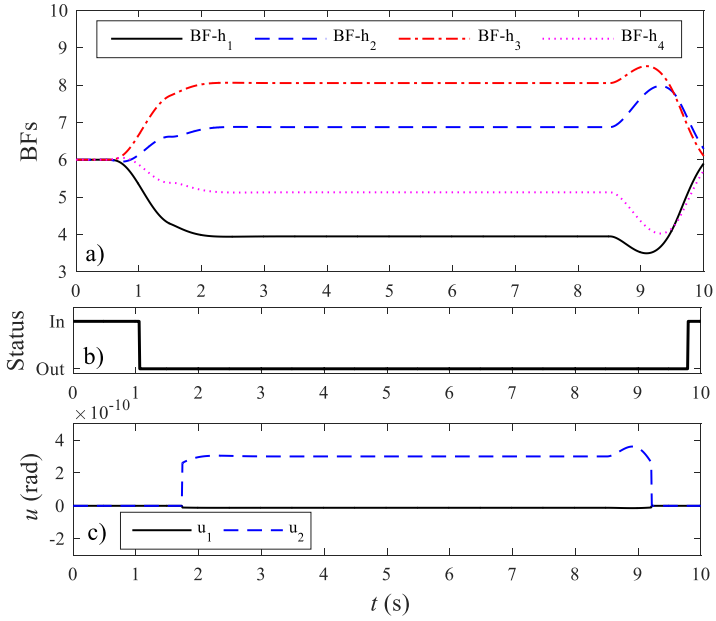

Fig. 60. Feedback Case Simulation Results in the J-turn Maneuver Based on the Fixed Stability Region, a) BFs Values, b) Vehicle Stability Status, c) Control Inputs.

To further verify the proposed time-varying CDBF method, another simulation is conducted by using a fixed stability region (common in literature) as the invariant set, bounded by the pink dotted lines in Fig. 59 (similar to that in Fig. 51). The four straight lines are represented by four time-invariant and control-independent barrier functions in linear forms. As observed in Fig. 59, the vehicle state trajectory is well covered by the fixed region. The four BFs, as shown in Fig. 60 a), are also positive during the whole maneuver since the trajectory is always in the fixed region. Moreover, since the vehicle state trajectory is far away from the boundaries, the feedback control inputs, as shown in Fig. 60 c), are pretty small and negligible. Such small feedback control inputs barely influence the vehicle dynamics, and thus the vehicle states are very similar to those shown in Fig. 55 in the feedforward simulation. However, as mentioned in Remark 11, the fixed region is too

large to precisely describe the vehicle stability. By checking the vehicle status with respect to the TVCD stability region, as shown in Fig. 60 b), it is revealed that the vehicle is not always "in" the stability region. This observation demonstrates that using the fixed stability region as the invariant set cannot guarantee vehicle stability.

Note that since the fixed stability region is not control-dependent, the stability constraints do not contain $\dot{u}$. In such a case, the control input u is selected as the control variable in the QP, where the constraints in (127) and (128) are not applied.

5.3.3.2.Double lane change maneuver

A double lane change maneuver is a commonly adopted scenario for the test of vehicle stability in extreme conditions. From a practical point of view, to verify the robustness of the proposed control method, measurement and estimation noises on vehicle states are added in the simulation. The parameters of the added noise signals (listed in Table 8) are determined based on experiment data[114][115]. All noise signals are assumed to follow a Gaussian probability distribution with a frequency of 200 Hz. In this simulation, the tire-road friction coefficient is set to 0.5 to simulate wet road conditions. Similar to the J-turn maneuver, two simulation cases (feedforward and feedback cases) are conducted and compared. As shown in Fig. 61, the profiles of the front wheel steering angle and the longitudinal velocity are given as two time-varying variables. Note that the longitudinal velocity is intentionally selected larger than 25 m/s to illustrate the generality of the proposed method.

In the feedforward case, the stability region is varying with respect to the feedforward steering angle and vehicle longitudinal speed. As shown in Fig. 62 a), negative CDBF

values are clearly observed, indicating that the system states are out of the TVCD stability region. Such unstable statuses are also verified by the vehicle status check shown in Fig. 62 b).

Table 8. Parameters of Noise in Simulations

Noise	Noise level (in percent of nominal values)	Frequency
V_y	5%	200 Hz
r	5%	200 Hz
V_x	3%	200 Hz
δ_f	3%	200 Hz

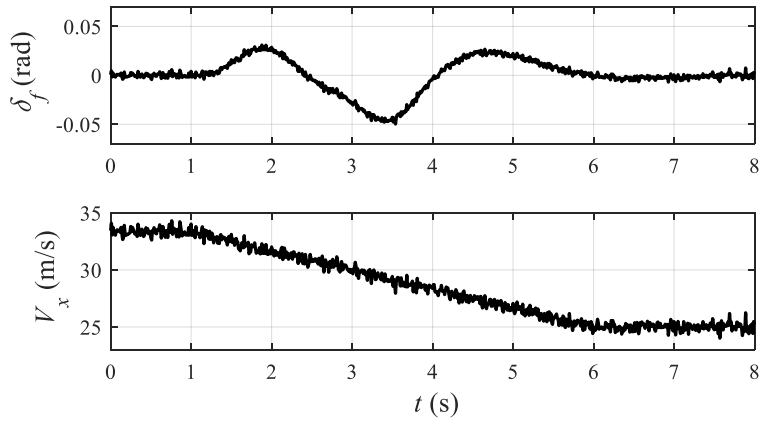

Fig. 61. Time-varying Profiles (the Front Wheel Steering Angle and the Longitudinal Velocity) in the DLC Maneuver.

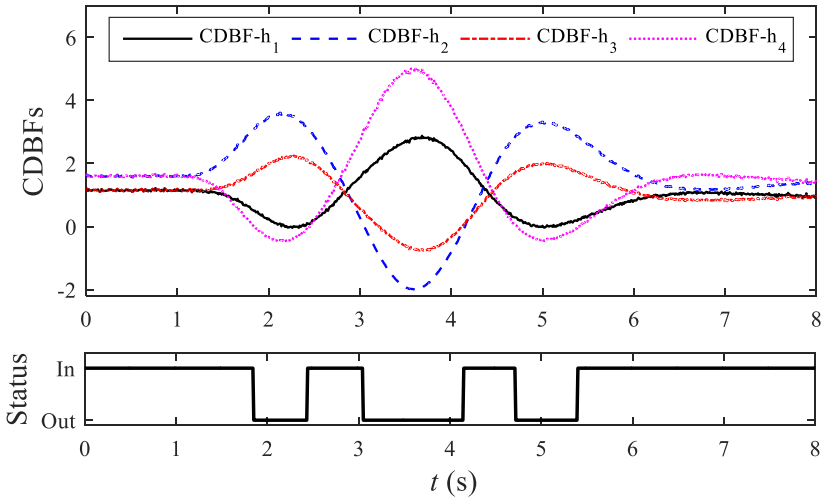

Fig. 62. Feedforward Case Simulation Results in the DLC Maneuver, a) CDBFs Values, b) Vehicle Stability Status.

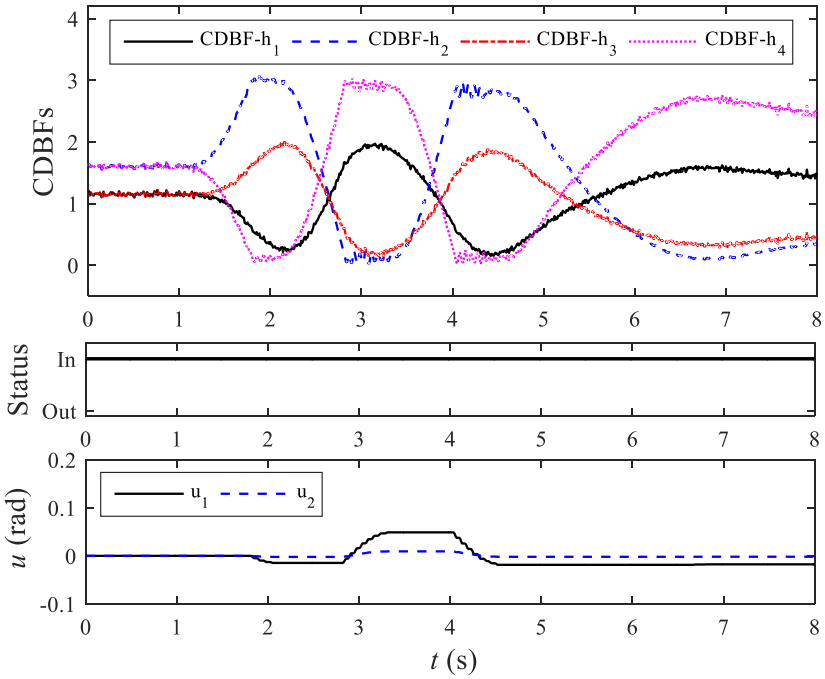

Fig. 63. Feedback Case Simulation Results in the DLC Maneuver, a) CDBFs Values, b) Vehicle Stability Status, c) Control Inputs.

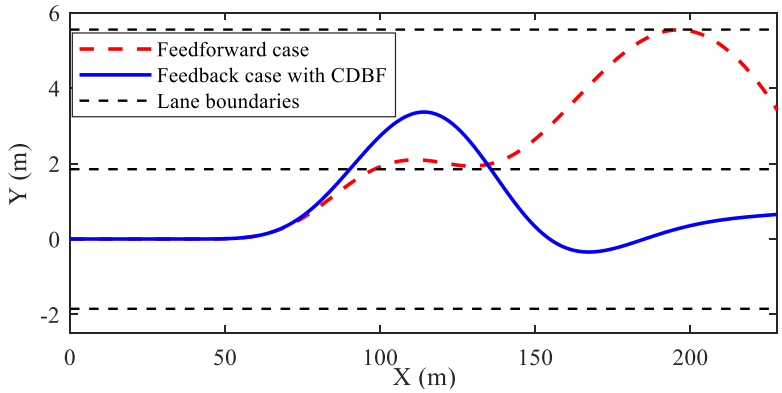

Fig. 64. Vehicle Trajectories Comparison in the DLC Maneuver.

In the feedback case, the vehicle is controlled by the proposed stability controller. All four time-varying CDBFs, as shown in Fig. 63 a), are positive, indicating that the vehicle states are always controlled to stay within the TVCD stability region. Since the vehicle stability region is both time-varying and control-dependent, the control design based on the proposed time-varying CDBF is verified. In Fig. 63 b), the vehicle statuses are always 'in' the stability region during the whole maneuver, which is consistent with the meaning of all four positive CDBF values. In Fig. 63 c), the real control inputs u after the integration of the virtual control $\dot{u}$ are presented. The stability improvement is also demonstrated by comparing the vehicle planar trajectories. As shown in Fig. 64, with only feedforward control, the vehicle cannot complete a DLC maneuver due to the loss of stability on a slippery road. However, with the proposed stability control design, the vehicle is able to successfully realize the DLC maneuver.

5.4. Switched Control Barrier Functions

Although the proposed time-varying CDBFs successfully ensure region-based vehicle driving stability, many vehicle safety-related challenges still need to be further investigated.

One of the challenges is that the safety constraints are not always fixed or activated due to the system's dynamic characteristics or uncertain environment. To ensure system safety in such challenging situations, control methods that can handle multiple switched constraints, especially the discontinuous ones, become necessary. The major difficulty in designing such a controller lies in how to define a switching problem between multiple safety sets and multiple control algorithms. To describe and solve these problems, various methods have been proposed, mainly including invariant multi-set [116][117], switch-robust control invariant (switch-RCI) sets [118], (spatial) temporal-logic specification [119]-[120], and non-smooth barrier function (NBF) [122]-[125].

First, the invariant multi-set was proposed in [116][117], where the definition of the invariant sets was extended with constrained switching signals. Namely, an invariant multi-set is defined as a collection of sets that follows a constrained switching signal. If the system states started in the first set in sequence, the system states would stay in the sets that follow the switching signal [116][117]. The second method is the switch-RCI sets [118], in which the constraints are mode-dependent and a switching sequence is also involved in the problem statement. The control objective is to find a robust controller that guarantees the invariance of each switched set in the switching sequence. Especially, if the initial state, mode, and remaining dwell time were contained in an initial condition set, there existed a control law that guaranteed the invariance of the switched sets for all future time and all admissible switching sequences [118]. However, in [116]-[118], any instructions to find such a safety-guaranteed control law were not introduced. The third method was called (spatial) temporal-logic specification [119][120], in which the

switching signals are mainly in spatial or temporal logic. Such a characteristic requires the switching sets to be connected, which makes it not suitable to resolve the problem when the switched sets are not connected.

Different from the above three methods, to compose multiple invariant sets that do not follow specific switching sequences, compositional barrier functions [121] was proposed with the usage of AND or OR logic operator. However, adding logic operators causes robustness issues to the composed barrier functions. To retain robustness, Boolean logic (MAX and MIN operator) was used in [122]. Nevertheless, the MAX and MIN operator introduces undifferentiability issue to barrier functions. To solve this issue, a non-smooth barrier function (NBF) was proposed in [122]. Inspired by the concept of non-smooth Lyapunov function (due to the discontinuous right-hand side of the differential equation) in [123], NBF is not necessarily required to be differentiable. The NBF was then further extended for controller design as a non-smooth control barrier function (NCBF) [124]. By considering the time-varying NCBF with jumps, the hybrid NBFs (HNBFs) and controlled HNBFs were proposed in [125]. However, NBFs do not explicitly address the undifferentiability issue of different invariant sets. Besides, NBFs are also not suitable to solve the problems where no intersections or unions exist between invariant sets.

Based on the aforementioned review on switching invariant sets and barrier functions, two potential issues can be revealed. First, when the switching signal or mode is not restricted by certain mappings, especially when they are determined by the system states or external inputs, how to describe the invariance between multiple sets becomes challenging. For example, in the vehicle lane-keeping problem, the lane boundaries are

normally regarded as safety constraints. If a lane changing signal is demanded (e.g. by the driver's command or an automated driving decision), the original lane boundaries need to switch to new lane boundaries. Different from the existing pre-defined switching mode, such a lane changing signal is normally determined based on the factors that cannot be pre-defined, such as vehicle states or surrounding environment. Therefore, in this example or other similar scenarios, how to ensure system safety without predefined switching signals is worthy to be studied.

Second, although the switched invariant sets and related concepts were studied and defined [116]-[120], the corresponding control problems have not been particularly discussed. Since CBFs are determined for the specific controlled invariant set (CIS), the switching between CISs could also affect the corresponding formulation and design of CBFs. Normally, CBFs are defined as continuously differentiable functions to depict the boundaries of CIS. Due to the discontinuity in switching action, the CBF may lose differentiability.

In this section, to address the aforementioned two issues, a novel concept of switched CIS (SCIS) and the corresponding switched CBF (SCBF) are first proposed. Then, regarding the undifferentiability issue in SCBF, the switched safety sets are relaxed by the proposed relaxation functions, where the switching is eliminated since the relaxed boundary functions are continuous and differentiable. Sufficient conditions for selecting a relaxation function are proposed. It is shown that the selection of such a function could be, but not limited to, time-dependent, state-dependent, or control-dependent. Moreover, the

proposed method is applied to a vehicle lane-keeping problem and verified by simulation results.

5.4.1. Problem Statement and Definitions

In this section, the problem statement and definitions of SCIS and SCBF are first introduced. Then, to solve the problems in SCIS and SCBF, the relaxation functions are defined, where the corresponding selection algorithms are also introduced. To deal with the switching problem among multiple CIS, the relaxation function chain is proposed.

5.4.1.1.Switched Controlled Invariant Set

The CIS in Definition 2 is not suitable to describe the invariance control problem for switched safety sets. To address this issue, the CIS in Definition 2 is extended to the SCIS as follows.

Definition 7. Consider a nonlinear control system in (82), a collection of the sets $\psi_{p_i} \in R^n$, where $p_i \in \nu \; i \in N^0 = \{0,1,2,...\}$ denotes the switching mode, is said to be *switched controlled invariant* with respect to (82), if for all $x(0) \in \psi_{p_0}$ and $p_0 \in \nu$, there exists a feedback control law $u = \phi(x, p_i)$, which assures the existence and uniqueness of the solution $x(t) \in \psi_{p_i}$ for all $t > 0$. ν denotes the set of all feasible switching modes.

Remark 15: Every single set in the collection of $\psi_{p_i} \in R^n$ should be controlled invariant within the mode p_i. The switching modes in Definition 7 are connected by the switching signals $s_{p_i \to p_j, i \neq j, i, j \in N^0}$ that can depend on, but are not limited to, system states, time

variables, and control inputs. The switching signals are discrete functions that depend on continuous variables.

5.4.1.2.Switched Control Barrier Function

Based on the defined SCIS, a problem statement to define SCBF is given as follows.

Definition 8. Consider a nonlinear control system in (82) and a SCIS in Definition 7, for every single set in SCIS, ψ_{p_i} is defined by a continuous and differentiable function $h_{p_i}(x): R^n \to R$,

$$h_{p_i}(x) \geq 0, x \in \psi_{p_i}, \tag{130}$$

$$h_{p_i}(x) = 0, x \in \partial\psi_{p_i}, \tag{131}$$

$$h_{p_i}(x) > 0, x \in Int(\psi_{p_i}), \tag{132}$$

where $\partial\psi_{p_i}$ and $Int(\psi_{p_i})$ denote the boundary and the interior of ψ_{p_i}, respectively. If there exist a control u and class K functions α_1, α_2, α_3, such that for all $x \in Int(\psi_{p_i})$,

$$1/\alpha_1(h_{p_i}(x)) \leq B_{p_i}(x) \leq 1/\alpha_2(h_{p_i}(x)), \tag{133}$$

$$L_f B_{p_i}(x) - \alpha_3(h_{p_i}(x)) \leq 0, \tag{134}$$

or if there exist a control u and an extended class K function α such that for all $x \in \psi_{p_i}$,

$$L_f h_{p_i}(x) + \alpha(h_{p_i}(x)) \geq 0, \tag{135}$$

$B_{p_i}(x)$ is a reciprocal switched control barrier function (RSCBF) and $h_{p_i}(x)$ is a zeroing switched control barrier function (ZSCBF) at the switching mode p_i.

Remark 16: In a general definition of a switching action, the switching modes p_i are discrete, which could introduce discontinuity and differentiability to $h_{p_i}(x)$ and $B_{p_i}(x)$ in Definition 8. Therefore, to retain the invariance of SCIS, the switching signals $s_{p_i \to p_j, i \neq j}$ need to be continuous and differentiable.

The issues mentioned in Remark 16 can be addressed by replacing the switching signal by a continuous and differentiable relaxation function. With relaxation, the switching signal becomes continuous and differentiable while still having the switching property. To avoid any unsafe system states in the switching transient, a proper selection of the relaxation function needs to be studied. The related definition and selection of a relaxation function are described in detail in the following two subsections.

5.4.1.3.Relaxation Function

To address the discontinuity and undifferentiability issue of SCBF during the switching action $s_{p_i \to p_j}$, an effective method is to connect the switched invariant sets by a relaxation function, which smooths the switching action and thus eliminates the discontinuous switching signal. With a smoothed switching signal, two CISs can be merged as one, of which the boundaries are smooth and still change with respect to the original switching signal. By combining the boundary functions, the original CISs are "relaxed". Such a relaxation function connects two switched sets and forms one connected set where continuous and differentiable boundary functions can be formulated. In particular, if the two CISs do not have an intersection or their intersection only contains one element, it is impossible to always cover the system states within the CISs (safety sets) during the switch.

The proposed relaxation function becomes particularly effective in avoiding the unsafe system states by connecting "the blank" between the two disconnected switched sets. With the above basic ideas of the relaxation function, how to properly select a relaxation function without losing the switching property and invariance conditions becomes a problem. To address these issues, some requirements for the selection of relaxation functions are identified as follows.

Requirement 1. The selected relaxation functions are required to properly fit the behavior of the switching signal while still connect the boundary functions before and after the switch. Namely, the formulation of the relaxation function should be determined based on the properties of the events that trigger the switch.

To better illustrate this idea, a switching problem in a vehicle lane changing scenario is taken as an example. From the safety control perspective, the lane-changing commands (switch signals) in autonomous ground vehicles (AGVs) are normally made based on the distance (d) to the preceding vehicle. By comparing the actual distance (d) with a safe distance (d_{safe}), which is determined by the speeds of the front vehicle and the controlled vehicle, the lane-changing (switching) signal can be determined.

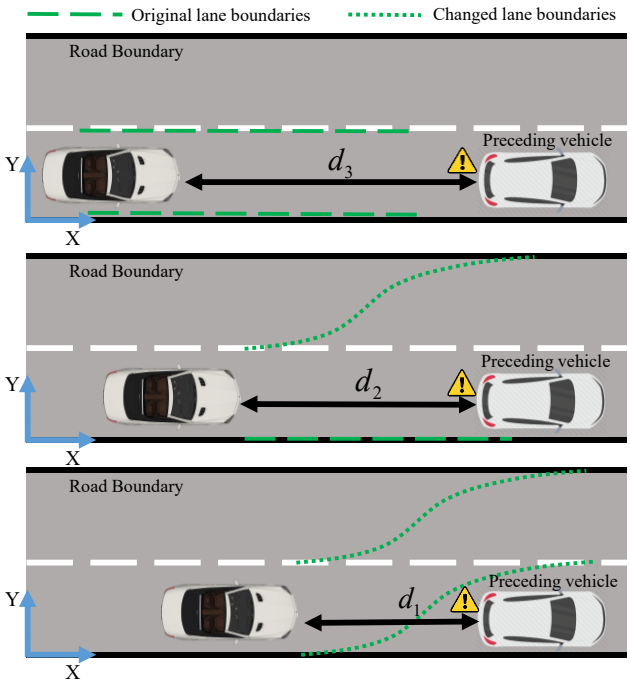

Fig. 65. Safety Distances in a Lane-changing Scenario.

Taking the lane changing scenario in Fig. 65 as an example, three safe distances (d_{safe}) are designed to deliver a smooth lane changing motion. First, d_1 in Fig. 65 is the minimum safety distance that a collision can only be avoided by changing lane or changing lane + braking. d_2 is the distance that a collision can be avoided by either changing lane or braking. d_3 is the distance that no additional steering or braking action is needed to keep the vehicle safe. As shown in Fig. 65, when $d \geq d_3$, the vehicle safety constraints are defined as the current lane boundaries for lane keeping. When $d_3 > d \geq d_2$, the left lane constraint is changed to a curvy lane boundary (the green dot line) that crosses the actual lane boundary while the right lane constraint keeps the same. When $d_2 > d \geq d_1$, both lane boundary constraints are relaxed and changed as curvy lane boundaries. Since the changes of left and right lane boundary constraints do not occur simultaneously, the lane-changing

control effort could be smoothened with gradually changing boundaries. As observed, the constraints switch depends on the varying distances, where an aforementioned relaxation function (with respect to the safety distance d_{safe}) between invariant sets will be utilized.

Based on the required properties of the relaxation function, the selection of a relaxation function is not unique. Depending on various vehicle driving scenarios or other working conditions of autonomous systems, a relaxation function may be state-dependent, time-varying, control-dependent, and/or (multiple) parameter-dependent. The problem statement to define a relaxation function and an example of one relaxation function formulation are introduced as follows.

Definition 9. Consider a nonlinear control system in (82) and two CISs linked by a switching signal from mode $p_1 \to p_2$ as

$$\psi_{p_1} = \left\{ x \middle| h_{p_1}(x) \geq 0 \right\}, \tag{136}$$

$$\psi_{p_2} = \left\{ x \middle| h_{p_2}(x) \geq 0 \right\}, \tag{137}$$

where $h_{p_1}(x)$ and $h_{p_2}(x)$ are two CBFs. Without losing the switching property from $p_1 \to p_2$, if ψ_{p_1} and ψ_{p_2} can be integrated by a bounded continuous and differentiable function $R(x,t,u,\ldots) \in [0,k]$ to a new CIS ψ as

$$\psi = \left\{ \begin{array}{l} x \middle| h_3(x,t,u,\ldots) = R(x,t,u,\ldots) h_{p_1}(x) + \\ \qquad\qquad \left(k - R(x,t,u,\ldots)\right) h_{p_2}(x) \geq 0 \end{array} \right\}, \tag{138}$$

$R(x,t,u,\ldots)$ is called a relaxation function of the switching from ψ_{p_1} to ψ_{p_2}.

Remark 3: As mentioned in Requirement 1, the relaxation function should properly describe the switching properties in $p_1 \to p_2$, so that the new set ψ can ensure the

switching action between the original CISs. The relaxation function can be independent of the corresponding switching signal, and the variables therein can be system states, time variable, and/or control inputs.

The purpose of defining a relaxation function and a new CIS is to ensure the system states can be safely transferred during the switch. To achieve this purpose, the connecting set ψ should also be a CIS, where the system states are controlled inside the set while being guided with the switching signal simultaneously. Although the safety constraints of the original sets are relaxed and can be violated during the switching, as long as the invariance of ψ can be guaranteed, the aforementioned control objective can be achieved. Namely, in the control of retaining the invariance from one CIS to another, how to guarantee the invariance of the connected set ψ is critical. The second requirement for relaxation function is given as follows.

Requirement 2. For the safety sets in Definition 9, no matter $\psi_{p_1} \cap \psi_{p_2} = \varnothing$ or not, the selected relaxation function should guarantee the invariance conditions of the new connect set ψ are satisfied.

To address this requirement, the following lemma is proposed to provide a sufficient condition for selecting such a relaxation function. Specifically, the relaxation function and the connected control barrier function in (138) are assumed only state-dependent. Thus, the first order Lie derivative of the combined CBF $h_3(x)$ is

$$\begin{aligned} L_f h_3(x) = {} & L_f R(x) h_{p_1}(x) + R(x) L_f h_{p_1}(x) \\ & - L_f R(x) h_{p_2}(x) + \left(k - R(x)\right) L_f h_{p_2}(x) \end{aligned}. \tag{139}$$

Depending on the variables that R is composed of (e.g., time variable), $L_f R(x)$ is calculated by the partial derivative of the corresponding variables.

Lemma 1. Assume there exist a common control *u* and two class *K* functions that make the sets in (136) and (137) two independent CISs. If R and $L_f R(x)/R$ are both positive and there exists a linear class *K* function α_3, such that for all $x \in Int(\psi)$

$$L_f h_3(x) + \alpha_3(h_3(x)) \geq 0. \tag{140}$$

the set connected by a positive relaxation function R in (138) is also a CIS.

Proof: Since the sets in (136) and (137) are two CISs, then the following conditions hold.

$$L_f h_{p_1}(x) + \alpha_1(h_{p_1}(x)) \geq 0, \tag{141}$$

$$L_f h_{p_2}(x) + \alpha_2(h_{p_2}(x)) \geq 0. \tag{142}$$

If the common control *u* that satisfies both the invariance conditions in (141) and (142) also satisfies the invariance condition in (140), the invariance of the connected set, which transfers the invariance of ψ_{p_1} to that of ψ_{p_2}, can be guaranteed. Assume the invariance condition in (140) can be satisfied by the common control *u.* Substitute (139) into (140)

$$\begin{aligned} &L_f R(x) h_{p_1}(x) + R(x) L_f h_{p_1}(x) - \\ &L_f R(x) h_{p_2}(x) + (k - R(x)) L_f h_{p_2}(x) \\ &+\alpha_3(R(x) h_{p_1}(x) + (k - R(x)) h_{p_2}(x)) \geq 0 \end{aligned} \quad . \tag{143}$$

Since α_3 is a class *K* function in linear form, reorganize (143), we have

$$\begin{aligned}&\left[L_f R(x)+\alpha_3\left(R(x)\right)\right]\left[h_{p_1}(x)-h_{p_2}(x)\right]\\&+R(x)\left(L_f h_{p_1}(x)-L_f h_{p_2}(x)\right)\\&+k\left(\dot{h}_{p_2}(x)\dot{x}+\alpha_3\left(h_{p_2}(x)\right)\right)\geq 0\end{aligned}. \tag{144}$$

In (144), $k\left(\dot{h}_{p_2}(x)\dot{x}+\alpha_3\left(h_{p_2}(x)\right)\right)$ is positive if α_2 in (142) is selected as the same as α_3. Thus, if (145) holds, (144) holds.

$$\begin{aligned}&\left[L_f R(x)+\alpha_3\left(R(x)\right)\right]\left[h_{p_1}(x)-h_{p_2}(x)\right]\\&+R(x)\left(L_f h_{p_1}(x)-L_f h_{p_2}(x)\right)\geq 0\end{aligned}. \tag{145}$$

Divide both sides of (145) by R (positive), we have

$$\begin{aligned}&\left(L_f h_{p_1}(x)-L_f h_{p_2}(x)\right)\\&+\left[L_f R(x)/R(x)+\alpha_3(1)\right]\left(h_{p_1}(x)-h_{p_2}(x)\right)\geq 0\end{aligned}. \tag{146}$$

Note that for a linear α_3, $\alpha_3(R)/R=\alpha_3(1)$ is always positive. In (146), take $h_{p_1}(x)-h_{p_2}(x)$ as a variable, if $h_{p_1}(x)-h_{p_2}(x)$ is positive and $L_f R(x)/R(x)$ is also positive, then $L_f R(x)/R(x)+\alpha_3(1)$ is positive and can be treated as the linear coefficient of a new linear class *K* function. Therefore, the same control *u* that makes (141) and (142) hold, ensures the invariance of the two original CISs and the connected set can be guaranteed. If $h_{p_1}(x)-h_{p_2}(x)$ is negative, one can multiply both sides of (146) by -1 and $h_{p_1}(x)-h_{p_2}(x)$ can be guaranteed as negative with the same control *u*, which infers (146) still holds. In both cases, if $L_f R(x)/R(x)$ is positive, (146) holds and (140) can be satisfied. The proof is complete. ■

Based on the aforementioned two requirements, one selection of a relaxation function (as an example) is a hyperbolic tangent function. Assuming the relaxation function is only dependent on system states, the hyperbolic tangent relaxation function is formulated as

$$R(x) = a + b\tanh\left((x-c)/d\right). \tag{147}$$

The hyperbolic tangent function in (147) returns values between a-b and a+b. The parameters c and d can be used to define the switching point and the smoothing level, respectively. The first time derivative of $R(x)$ is $\dot{R}(x) = b\,\mathrm{sech}^2\left((x-c)/d\right)/d$, where $\mathrm{sech}(z) = 1/\cosh(z) = 2/\left(e^z + e^{-z}\right)$. With $a = 0.5$, $b = 0.5$, $c = 0$ and $d = 1$, $R(x)$ is plotted as the blue dot-dash curve in Fig. 66. With a larger d=3, $R(x)$ (the red solid curve in Fig. 66) becomes smoother. With a smaller d=0.1, $R(x)$ (the green dash curve in Fig. 66) looks more like a step function. Thus, to describe a rapid switch action with repect to related system states, a small d is preferred.

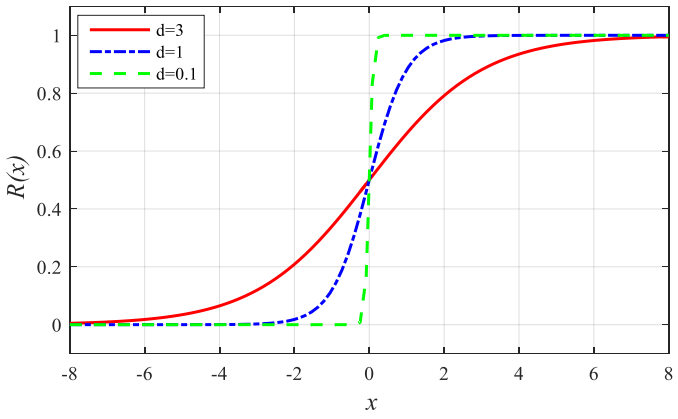

Fig. 66. Hyperbolic Tangent Functions with Different Parameters.

To determine a suitable parameter set of the relaxation function, the physical constraints need to be considered. For example, in the lane changing scenario, the switch

point and smoothing level should be properly selected to make sure the lane boundary constraints change at the right time (e.g. for safety purposes) and are smooth enough (e.g. for riding comfort purposes).

5.4.1.4.Relaxation Function Chain

When multiple (more than two) CISs are switched in a sequence, a scheme that describes consecutive switching actions becomes necessary. In this subsection, to solve the consecutive switching problem between multiple CISs, a relaxation function chain is introduced.

Lemma 2. For two independent CISs in (136) and (137) (in the general forms as ψ_{p_i} and ψ_{p_j}, $i \neq j$), if the system states finish the switching from ψ_{p_i} to ψ_{p_j} and keep staying within the switched set ψ_{p_j}, the relaxation function R_i can be released. Based on a newly observed switching signal, a new relaxation function R_j between the current set ψ_{p_j} and the next CIS $\psi_{p_k, k\neq j}$ can be determined following the structure shown in (138). For all the future set $\psi_{p_l, l\neq k}$, a relaxation function chain $R_{l, l\neq k}$ can be constructed until the switches among CISs stop.

Proof: If the system states are within the switched set ψ_{p_j}, then a control u and a class K function α, which make (140) satisfied, guarantee the invariance of ψ_{p_j}. For ψ_{p_j}, a new relaxation function R_j in Lemma 2, which connects ψ_{p_j} to a new switched set $\psi_{p_k, k\neq j}$, can be constructed. If the new relaxation function R_j satisfies the sufficient conditions in

Lemma 1, the invariance of ψ_{p_k} can also be guaranteed. Similarly, a chain of relaxation functions $R_{l,\, l\neq k}$ can be constructed and is able to guarantee the invariance of the switched sets until the switching signal stops. ■

The principle of relaxation function chain in SCIS is summarized in Algorithm 2.

Algorithm 2. Principle of Relaxation Function Chain in SCIS

Specify the original (current, *ith*) CIS and CBF.

for the starting switching signal $s_{p_i \to p_j}$ from the safety sets ψ_{p_i} to ψ_{p_j}, do

select a relaxation function R_i that properly describes the switching function and satisfies the condition in Lemma 1.

if the system states $x \in \psi_{p_j}$ then

update R_i to R_j based on the switching from ψ_{p_j} to ψ_{p_k};

end if s stops

end for

return.

5.4.2. Simulations and Discussions

In this section, a numerical example is first presented to demonstrate the effectiveness of the proposed relaxation function when connecting two CISs. Then, multiple CISs and a relaxation function chain are applied to a vehicle safety control problem, which aims at ensuring vehicle safety in a continuous obstacle avoidance (lane changing) scenario.

5.4.2.1.A Numerical Example

Consider a typical control affine system

$$\dot{Y} = f(Y) + g(Y)u\,, \tag{148}$$

where Y is the state variable and u is the system input. $f(Y) = -0.02Y$ and $g(Y) = 0.2$. A safety set with respect to Y is defined as

$$Y_{safe} = \left[Y_1(t), Y_2(t)\right], \tag{149}$$

where $Y_1(t) = \begin{cases} -2.5 & t \le 5 \\ 2.5 & t > 5 \end{cases}$ and $\mathrm{Y}_2(t) = \begin{cases} 2.5 & t \le 5 \\ 7.5 & t > 5 \end{cases}$ are the upper and lower bounds of the safety set. The switching action is assumed to be detectable as a time-varying function, where at 5 s, the safety set switches to a new set by positively shifting 5 units. The safety sets before and after the switch only have one intersection set or point as $\{Y = 2.5\}$.

Since the system safety constraints are time-varying, the relaxation function is also designed as a time-varying function in a hyperbolic tangent form as

$$R(t) = a + b\tanh\left((t-c)/d\right), \tag{150}$$

where $a = 0.5$, $b = 0.5$, $c = 5$, $d = 1$ are the parameters selected to properly fit the switch of safety sets in (149). Using the relaxation function in (150), two new connected CISs, which correspondingly depict the upper and lower bounds of the CIS in (149), are constructed as

$$\psi_1 = \left\{x \middle| h_1(x) = R(t)h_{11}(x) + \left(K - R(t)\right)h_{12}(x) \ge 0\right\}, \tag{151}$$

$$\psi_2 = \left\{x \middle| h_2(x) = R(t)h_{21}(x) + \left(K - R(t)\right)h_{22}(x) \ge 0\right\} \tag{152}$$

where $h_{11}(x) = Y - (-2.5)$, $h_{12}(x) = Y - 2.5$, $h_{21}(x) = 2.5 - Y$, $h_{22}(x) = 7.5 - Y$ are the four original barrier functions (positive), and $K = 1$.

Substituting $h_1(x)$ in (151) and $h_2(x)$ in (152) into (86), the invariance conditions of set ψ_1 and ψ_2 are

$$L_f h_1(x) + \alpha_1\left(h_1(x)\right) \geq 0, \tag{153}$$

$$L_f h_2(x) + \alpha_2\left(h_2(x)\right) \geq 0, \tag{154}$$

where

$$\begin{aligned} L_f h_1(x) = {} & \dot{R}(t) h_{11}(x) + R(x)\dot{h}_{11}(x) \\ & - \dot{R}(t) h_{12}(x) + \left(k - R(x)\right)\dot{h}_{12}(x) \end{aligned}, \tag{155}$$

$$\begin{aligned} L_f h_2(x) = {} & \dot{R}(x) h_{21}(x) + R(x)\dot{h}_{21}(x) \\ & - \dot{R}(x) h_{22}(x) + \left(k - R(x)\right)\dot{h}_{22}(x) \end{aligned}. \tag{156}$$

With the derived two invariant constraints in (153) and (154), the control input can be determined by a quadratic programming (QP) problem described as follows.

$$u = \underset{u\in}{\operatorname{argmin}} \quad 0.5uHu + Fu, \tag{157}$$

s.t.

$$A_{CBF} u \leq b_{CBF}, \tag{158}$$

where $H = [1]$, $F = 1$, $A_{CBF} = \begin{bmatrix} -k & k \end{bmatrix}^T$ and $b_{CBF} = \begin{bmatrix} 5\dot{R}(t) - aY - \dot{Y}_1 + \alpha_1\left(h_1(x)\right) \\ -5\dot{R}(t) + \dot{Y}_2 + aY + \alpha_2\left(h_2(x)\right) \end{bmatrix}$. α_1 and α_2 are class *K* functions, which are properly selected based on the sharing property among multiple CBFs [74] as $\alpha_1(x) = \alpha_2(x) = 100x$. Specifically, the parameters in α_1 and α_2 are selected as large values to keep the state as close to the center of the safety set as possible.

To illustrate the effectiveness of the proposed relaxation function between two CISs, a quantitative comparison between a case using a typical CBF (without relaxation function) and a case using the proposed SCBF (with proposed relaxation function) is presented. In the typical CBF case, the relaxation function is not involved and two CISs are switched by

a signal at 5 s. For each CIS, the set invariance is controlled by a ZCBF in (86). Since the two CIS only have one intersection point at 5 s, the system states are very likely to be outside of the second CIS right after 5 s. Therefore, a ZCBF is applied because a RCBF does not allow the system states to penetrate the set boundaries.

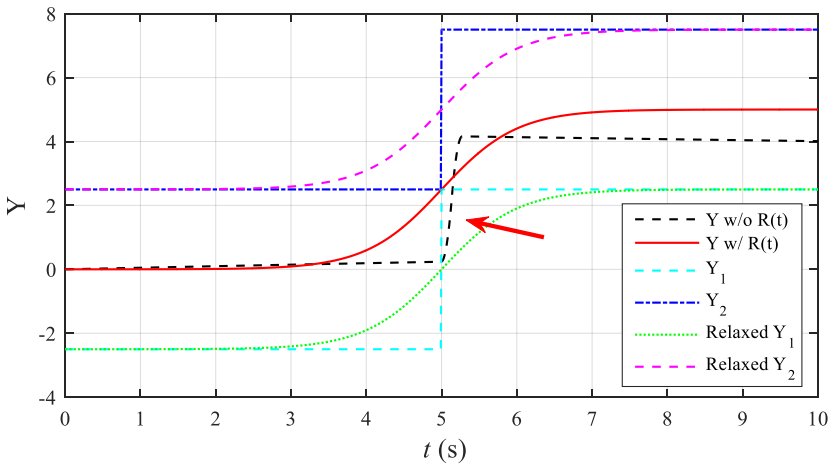

Fig. 67. State Variable (Y) in the Cases with (w/) and without (w/o) the Relaxation Function.

In Fig. 67, the system state, namely Y, in both cases (with and without the relaxation function) are presented and compared. The original safety set boundaries and the relaxed safety set boundaries are both plotted in Fig. 67 for comparison. As shown, in the case without the relaxation function, after the safety constraints switch at 5 s, the system state Y violates the constraints ($Y < Y_1$ as pointed by the red arrow) for a short period. On the other hand, in the case with the relaxation function $R(t)$, the safety set boundaries before and after the switch are relaxed and connected (relaxed Y_1 and Y_2), which form a new safety set with smooth boundaries. With the control input determined by (157), Y starts to change in advance before the switching signal, which makes it possible for Y to be strictly

controlled in the safety set. To verify this point, as shown in Fig. 68, the relaxed CBF values (h_1 and h_2 in (151) and (152)) keep steadily positive at 2.5. Meanwhile, the CBF values in the case without the relaxation function have obvious undesired negative values as pointed by the red arrow. Note that, during the switch, the system state is not necessarily required to always stay in the original safety sets.

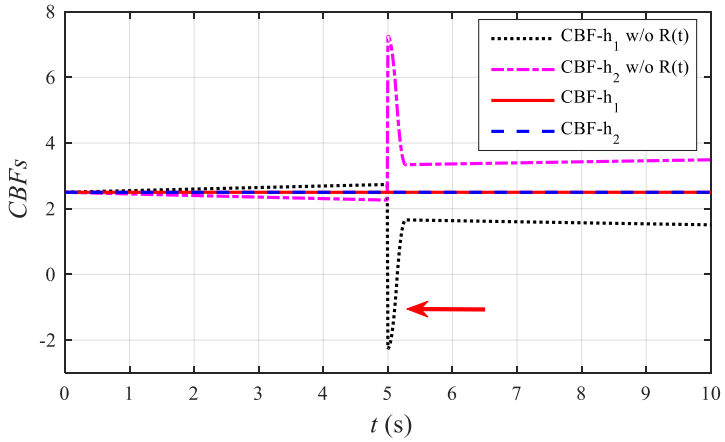

Fig. 68. Comparison of SCBF Values in the Cases with (w/) and without (w/o) the Relaxation Function.

5.4.2.2.Vehicle Safety Control using SCBF

One of the most common driving scenarios for AGVs is highway cruising. A safety highway cruising can be simply achieved by two main functions, namely the lane-keeping and lane-changing at the cruise speed. In this subsection, a vehicle safety control problem in continuous lane-changing and lane-keeping scenario is solved by the proposed SCIS and relaxation function chain. With the small-angle and constant longitudinal velocity approximation, a single-track vehicle lateral dynamic model is written in a state-space form as

$$\begin{bmatrix} \dot{V}_y \\ \dot{r} \end{bmatrix} = A \begin{bmatrix} V_y \\ r \end{bmatrix} + B\delta_f \,, \tag{159}$$

where $A = \begin{bmatrix} -\dfrac{\left(C_f + C_r\right)}{mV_x} & \dfrac{\left(l_r C_f - l_f C_r\right)}{mV_x} - V_x \\ \dfrac{\left(l_r C_f - l_f C_r\right)}{I_z V_x} & -\dfrac{\left(l_f{}^2 C_f - l_r{}^2 C_r\right)}{I_z V_x} \end{bmatrix}$, $B = \begin{bmatrix} \dfrac{C_f}{m} \\ \dfrac{l_f C_f}{I_z} \end{bmatrix}$. V_y and r are the vehicle lateral velocity and yaw rate, respectively. The front wheel steering angle δ_f is the only control input. A linear tire model is adopted since the lane changing maneuvers in this application are moderate without rapid longitudinal acceleration and deceleration. The vehicle kinematic model is formulated as

$$\begin{aligned} \dot{X} &= V_x \cos(\theta + \beta) \\ \dot{Y} &= V_x \sin(\theta + \beta) \end{aligned} \,, \tag{160}$$

where X and Y are the vehicle longitudinal and lateral displacement. $\theta = \int r$ is the vehicle heading angle (assuming zero initial heading), $\beta = V_y / V_x$ is the vehicle slip angle. The vehicle and tire parameters in (94) are listed in Table 9.

Table 9. Cornering Stiffness of Tires

Symbol	Parameters	Values
C_f	Front tire cornering stiffness	25000 *N/rad*
C_r	Rear tire cornering stiffness	25000 *N/rad*

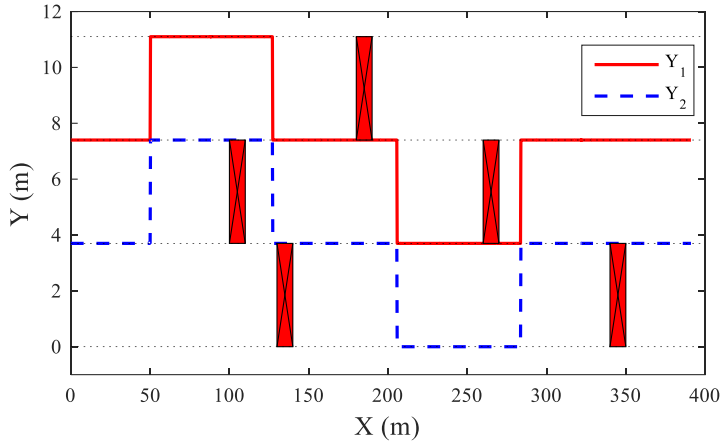

Fig. 69. Continuous Lane-changing and Lane-keeping Scenario and the Continuously Switched Lane Boundary Constraints.

As shown in Fig. 69, three standard-wide (3.7 meters) lanes are depicted by four dotted horizontal lines (Y=0, 3.7, 7.4, 11.1 *m*). In addition, five obstacles, depicted by the red boxes, are set in the middle of the lanes. To avoid the obstacles, the vehicle should first detect them and then change lane correspondingly. In this paper, a 50 meters (25 m/s$\times$2 s) forward detection range is selected based on the constant vehicle cruise speed (25 m/s) and a 2 seconds preview time window. If the real-time distance from the vehicle to the obstacle is less than 50 meters, a lane changing (switching) signal is generated. As shown in Fig. 69, the active left and right lane boundary constraints, which are depicted by the red solid and blue dash lines (Y_1 and Y_2), switches at the position where the vehicle detects the obstacle is within 50 meters. In Fig. 69, driving from the left to the right, the active lane boundaries switch four times during the whole procedure. To handle such a continuous SCIS problem, the proposed relaxation function chain is effective.

To solve this vehicle safety control problem, the safety sets composed by the switched lane boundaries are first formulated in a consequent manner as

$$\begin{aligned}
&\psi_1 = \{Y \,|\, 3.7 \le Y \le 7.4\}; \quad \psi_2 = \{Y \,|\, 7.4 \le Y \le 11.1\}; \\
&\psi_3 = \{Y \,|\, 3.7 \le Y \le 7.4\}; \quad \psi_4 = \{Y \,|\, 0 \le Y \le 3.7\}; \quad . \\
&\psi_5 = \{Y \,|\, 3.7 \le Y \le 7.4\}
\end{aligned} \tag{161}$$

The safety sets switch from ψ_1 to ψ_5 as the vehicle changes lanes to avoid the obstacles. The relaxation function chain is applied as follows. Starting at the switch from ψ_1 to ψ_2, a relaxation function is selected similar to that in (150) by replacing the time variable with the state variable Y. Correspondingly, the safety sets before and after the switching are connected in similar forms as those shown in (151) and (152). Then, following the procedure in (153)-(158) with the vehicle dynamics in (94) and (160), the steering angle, as the control input, is obtained. After the switch from ψ_1 to ψ_2 is finished, the vehicle is already in the safety set ψ_2. Next, to avoid the approaching obstacle, the safety set needs to switch from ψ_2 to ψ_3. Following the same control design procedure of the switching from ψ_1 to ψ_2, the vehicle safety can also be guaranteed when switching from ψ_2 to ψ_3. To finish the whole process, the procedure in Algorithm 2 should be followed until the safety set ψ_5 stops lane changing.

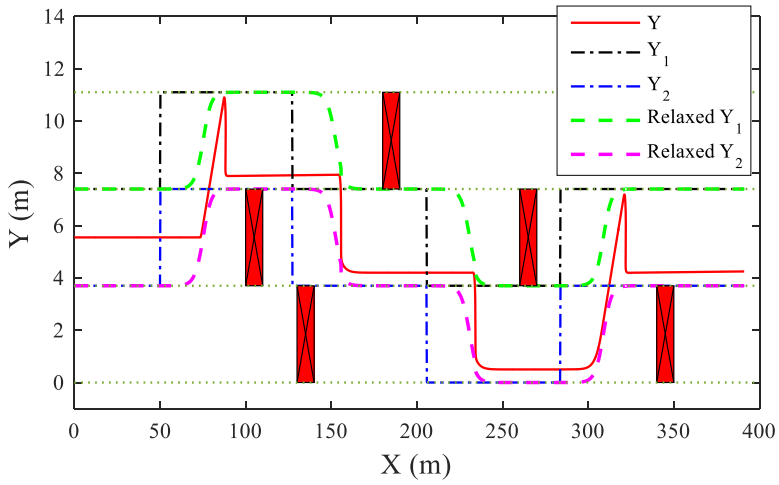

Fig. 70. X-Y Displacement of the Vehicle and the Switched Boundaries of Safety Set in Case 1.

In Fig. 70, the lane boundary constraints, which contains the relaxation functions for all four switches, are depicted by the dashed green and pink curves. As shown, the vehicle trajectory, depicted by the red solid curve, is well-controlled between the switched lane boundaries with the proposed relaxation function chain, which verifies the effectiveness of the proposed SCBF and relaxation function. Note that the "sharp" lane-changing of Y in Fig. 70 is caused by the compressed scale of X-axis. The actual turns of the vehicle path in Fig. 70 are smooth enough for normal vehicle driving.

5.5. Conclusions

A new concept of a TVCD invariant set and a novel control algorithm to guarantee the invariance of a TVCD set. By involving the TVCD properties, the proposed time-varying CDBF is more general than the (time-varying) CBFs studied in the literature. The newly developed theory and control methods are applied to solve a guaranteed region-based vehicle lateral stability control problem, where the vehicle lateral stability region, as the

controlled invariant set, is both time-varying and control-dependent. By showing the simulation results of high-speed J-turn and DLC maneuvers, the proposed new concepts and control design are verified. To deal with the undifferentiability issue of SCBFs during the switch, a relaxation function is proposed. Sufficient conditions for the selection of a relaxation function are provided. The concept of the relaxation function chain is introduced to handle the problem with multiple switches. The simulation results of a numerical problem and a vehicle safety control problem are presented to verify the proposed SCIS, SCBF, and relaxation function.

CHAPTER 6

CONCLUSIONS

6.1. Conclusions

The guaranteed vehicle stability control algorithms greatly enhance the safety of autonomous ground vehicles. In this dissertation, targeting at keeping the vehicle in the estimated lateral stability regions, a series of region-based vehicle lateral stability analyses and control algorithms are presented.

As the most fundamental step in the control algorithm, a new vehicle lateral stability region estimation method, which utilizes a local linearization method based on a four-wheel vehicle model and a nonlinear 2D LuGre tire model, is first proposed. The estimated vehicle lateral stability regions are more conservative compared with the regions estimated by the phase portrait and Lyapunov method in the previous studies. The conservation is mainly featured from the stricter and simultaneously applied vehicle and tire stability criteria, which are mathematically derived by using the applied local linearization method. Moreover, simulation results show that the lateral load transfer, vehicle longitudinal velocity, tire-road friction coefficient, and steering angle all have impacts on the estimated vehicle lateral stability regions. Serving as the basis for automated driving control systems, the vehicle lateral stability region has the potential for numerous vehicle control applications.

Based on the shiftable vehicle lateral stability region, novel vehicle lateral stability control methods are proposed. To accurately analyze the vehicle stability status based on an irregular and shiftable stability region, a projection method, the shifting vector, and the

dynamic margin are proposed and integrated as one complete stability analysis method. The proposed analysis method is real-time applicable for vehicle lateral stability control. Then, based on the stability analysis results, dynamic sliding mode controllers are designed. By selecting the boundaries of the stability region with the proposed dynamic margin as the sliding surfaces, the proposed vehicle lateral stability control guarantees that the vehicle trajectory is always controlled in the adopted stability region. With higher computational demand and less chattering, the proposed non-overshooting model predictive control also ensures the same control performance.

To achieve the guaranteed stability control with higher efficiency and less computational demands, a new concept of time-varying control-dependent (TVCD) invariant set and a novel control algorithm to guarantee the invariance of a TVCD set are proposed. By involving the TVCD properties, the proposed time-varying control-dependent barrier function is more general than the time-varying control barrier function studied in the literature. The newly developed theory and control methods are applied to a guaranteed region-based vehicle lateral stability control problem, where the vehicle lateral stability region, as the controlled invariant set, is both time-varying and control-dependent. The vehicle is successfully kept within the stability region, verifying the vehicle's lateral stability is guaranteed.

6.2. Future Work

The effectiveness of the region-based stability control algorithm enables itself for an extended and variety of applications. Additional suggestions for further development and studies are explained as follows.

6.2.1. Multi-Dimensional Stability Regions

The vehicle stability region can be extended in multiple directions, which makes itself practical and applicable to more applications. Considering the coupling effect between the tire longitudinal and lateral forces, the vehicle's longitudinal and lateral stability can be integrated, where a 3-dimensional stability region would be estimated. Moreover, other vehicle indexes, such as the rollover index, can also be integrated with the lateral stability region to solve the vehicle motion control problems with multi-dimensional evaluations.

6.2.2. Integrating CDBF with CLF and Actuator Dynamics

As an extension of the integrated CLF-CBF studies, when CDBF and CLFs need to be integrated, how to address the compatibility problem of different forms of constraints must be resolved. Moreover, when applying CBF and CDBF, the dynamics and control of actuators or subsystems are often ignored. Although the low-level actuation errors could be modeled as uncertainties and resolved by robust CBF methods, the commonly adopted solutions of adding a slack number to barrier functions can conservatively degrade control performance. Therefore, how to effectively integrate the actuator dynamics with the CDBF becomes an interesting and worth-studying topic.

6.2.3. Switched CDBF in General Form

In autonomous vehicle safety control problems, the switched CDBF can be applied to various scenarios. Therefore, the definition of switched CDBF, especially the selection of relaxation functions, needs to be extended to a more general form. The practical issues in

the selection of relaxation function should also be studied to better describe the switching between different scenarios.

BIBLIOGRAPHY

[1] A. Taeihagh and H. S. M. Lim, "Governing autonomous vehicles emerging responses for safety liability privacy cybersecurity and industry risks," *Transport Reviews*, Vol. 39, No. 1, pp. 103-128, 2019.

[2] D. Milakis, B. van Arem, and B. van Wee, "Policy and society related implications of automated driving A review of literature and directions for future research," *Journal of Intelligent Transportation Systems: Technology, Planning, and Operations*, Vol. 21, No. 4, pp. 324-348, 2017.

[3] J. M. Anderson, N. Kalra, K. D. Stanley, P. Sorensen, C. Samaras, and O. A. Oluwatola, "Autonomous vehicle technology: a guide for policymakers," RAND Corporation, Santa Monica, CA, USA, 2014.

[4] U.S. Department of Transportation, "Preparing for the future of transportation: automated vehicles 3.0 (AV 3.0)," Oct. 2018.

[5] On-Road Automated Driving (ORAD) committee, Taxonomy and definitions for terms related to driving automation systems for on-road motor vehicles, *SAE International,* Jun. 2018.

[6] M. Maurer, J. C. Gerdes, B. Lenz, and H. Winner, "Autonomous driving technical, legal and social aspects," *Daimler und Benz-Stiftung*, Ladenburg, 2015.

[7] MIT Technology Review Insights, "Autonomous driving: Safety first," Mar, 2019.

[8] M. M. Díaz, F. Soriguera, "Autonomous vehicles: theoretical and practical challenges," *XIII Conference on Transport Engineering*, pp. 275-282, 2018.

[9] S. Inagaki, I. Kushiro, M. Yamamoto, "Analysis on vehicle stability in critical cornering using phase-plane method," *JSAE Review*, Vol. 16, No. 2, pp. 287-292, 1995.

[10] E. Ono, S. Hosoe, H. D. Tuan, and S. Doi, "Bifurcation in vehicle dynamics and robust front wheel steering control," *IEEE Transactions on Control Systems Technology*, Vol. 6, No. 3, pp. 412-420, 1998.

[11] S. Shen, J. Wang, P. Shi, and G. Premier, "Nonlinear dynamics and stability analysis of vehicle plane motions," *Vehicle System Dynamics*, Vol. 45, No. 1, pp. 15-35, 2007.

[12] Y. E. Ko, and J. M. Lee, "Estimation of the stability region of a vehicle in plane motion using a topological approach," *International Journal of Vehicle Design*, Vol. 30, No. 3, pp. 181-192, 2002.

[13] F. D. Rossa, M. Gobbi, G. Mastinu, C. Piccardi, and G. Previati, "Bifurcation analysis of a car and driver model," *Vehicle System Dynamics*, Vol. 52, No.1, pp. 142-156, 2014.

[14] C. G. Bobier, C. E. Beal, J. C. Kegelman, R. Y. Hindiyeh, and J. Christian Gerdes, "Vehicle control synthesis using phase portraits of planar dynamics," *Vehicle System Dynamics*, pp. 1318-1337, 2018.

[15] F. Farroni, M. Russo, R. Russo, M. Terzo, and F. Timpone, "A combined use of phase plane and handling diagram method to study the influence of tyre and vehicle characteristics on stability," *Vehicle System Dynamics*, Vol. 51, No. 8, pp. 1265-1285, 2013.

[16] J. Ni, J. Hu, and C. Le, "Envelope control for four-wheel independently actuated autonomous ground vehicle through AFS/DYC integrated control," *IEEE Transactions on Vehicular Technology*, Vol. 66, No. 11, pp. 9712-9726, 2017.

[17] C. G. Bobier and J. Christian Gerdes, "Staying within the nullcline boundary for vehicle envelope control using a sliding surface", *Vehicle System Dynamics*, Vol. 51, No.2, pp. 199-217, 2013.

[18] D. B. Johnson and J. C. Huston, "Nonlinear lateral stability analysis of road vehicles using Lyapunov second method," *SAE Technical Paper* 841057, pp. 798-805, 1984.

[19] J. Samsundar and J. Huston, "Estimating lateral stability region of a nonlinear 2 degree-of-freedom vehicles," *SAE paper*, 1998.

[20] G. Yin, Z. Qing, and J. Wang, "Estimating lateral stability region for four wheel independently-actuated electric vehicle considering steering," *SAE paper*, 13CV-0097, 2013.

[21] S. Sadri and C. Wu, "Stability analysis of a nonlinear vehicle model in plane motion using the concept of Lyapunov exponents," *Vehicle System Dynamics*, Vol. 51, No. 6, pp. 906-924, 2013.

[22] P. Currier, "A method for modeling and prediction of ground vehicle dynamics and stability in autonomous systems," Ph.D. Thesis, 2011.

[23] E. Hashemi, M. Pirani, A. Khajepour, and A. Kasaiezadeh, "A comprehensive study on the stability analysis of vehicle dynamics with pure combined slip tyre models," *Vehicle System Dynamics*, Vol. 54, No. 12, pp.1736-1761, 2016.

[24] J. Yi, J. Li, J. Lu, and Z. Liu, "On the stability and agility of aggressive vehicle maneuvers: A pendulum-turn maneuver example," *IEEE Transactions on Control Systems Technology,* Vol. 20, No. 3, pp. 663-676, 2012.

[25] R. C. Hoffman, J. L. Stein, L. S. Louca, and K. Huh, "Using the Milliken Moment Method and dynamic simulation to evaluate vehicle stability and controllability," *International Journal of Vehicle Design*, Vol. 48, No. 1, pp.132-148, 2008.

[26] D. L. Milliken, E. M. Kasprzak, L. D. Metz, and W. F. Milliken, Race car vehicle dynamics-problem, answers, and experiments, *SAE International*, R-280, 2003.

[27] A. Daher, C. Bardawil, and N. Daher, "Vehicle stability based on G-G diagram through braking and driveline," in *Proceedings of American Control Conference*, pp. 309-314, 2017.

[28] C. Diels and J. E. Bos, "Self-driving carsickness," *Applied Ergonomics*, Vol. 53, pp. 374-382, 2016.

[29] S. Salter, D. Thake, S. Kanarachos, and C. Diels, "Motion sickness prediction device for automated vehicles," *International Journal of Mechanical and Production Engineering*, Vol.7. No. 2, pp. 68-74, 2019.

[30] E. Mousavinejad, Q. Han, F. Yang, Y. Zhu and L. Vlacic "Integrated control of ground vehicles dynamics via advanced terminal sliding mode control," *Vehicle System Dynamics*, Vol. 55, No. 2, pp. 268-294, 2017.

[31] J. He, D. Crolla, M. Levesley, W. Manning, "Coordination of active steering, driveline, and braking for integrated vehicle dynamics control," in *Proceedings of the Institution of Mechanical Engineers, Part D: Journal of Automobile,* Vol. 220, No. 10, pp. 1401-1420, 2006.

[32] X. Jin, G. Yin, C. Bian, J. Chen, P. Li, and N. Chen, "Gain-scheduled vehicle handling stability control via integration of active front steering and suspension systems," *Journal of Dynamic Systems, Measurement, and Control*, Vol. 138, 2016.

[33] J. Ni, J. Hu, and C. Le, "Envelope control for four-wheel independently actuated autonomous ground vehicle through AFS/DYC integrated control," *IEEE Transactions on Vehicular Technology,* Vol. 66, No. 11, pp. 9712-9726, 2017.

[34] T. Chung and K. Yi, "Design and evaluation of side slip angle based vehicle stability control scheme on a virtual test track", *IEEE Transactions on Control Systems Technology*, Vol. 14, No.2, 2006.

[35] E. Mousavinejad, Q. Han, F. Yang, Y. Zhu, and L. Vlacic, "Integrated control of ground vehicles dynamics via advanced terminal sliding mode control," *Vehicle System Dynamics*, Vol. 55, No. 2, pp. 268-294, 2017.

[36] S. M. Erlien, S. Fujita, and J. C. Gerdes, "Shared steering control using safe envelopes for obstacles avoidance and vehicle stability," *IEEE Transactions on Intelligent Transportation Systems*, Vol. 17, No. 2, 2016.

[37] P. Yih and J. C. Gerdes, "Modification of vehicle handling characteristics via steer-by-wire," *IEEE Transactions on Control Systems Technology*, Vol. 13, No. 6, pp. 965-976, 2005.

[38] J. Ackermann, "Robust decoupling, ideal steering dynamics and yaw stabilization of 4WS cars," *Automatica*, Vol. 30, No. 11, pp. 1761-1768, 1994.

[39] Y. Hirano and K. Fukatani, "Development of Robust Active Rear Steering Control for Automobile," *JSME International Journal Series C*, Vol. 40, No. 2, pp. 231-238, 1997.

[40] S. Horiuchi, N. Yuhara, and A. Takei, "Two degree of freedom/H∞ controller synthesis for active four wheel steering vehicles," *Vehicle System Dynamics*, Vol. 25, No. 1, pp. 275-292, 1996.

[41] T. Hiraoka, O. Nishihara, and H, Kumamoto, "Automatic path-tracking controller of a four-wheel steering vehicle," *Vehicle System Dynamics*, Vol. 47, No. 10, pp. 1205-1227, 2009.

[42] Y. Yoon, J. Shin, H. Kim, Y. Park, and S. Sastry, "Model-predictive active steering and obstacle avoidance for autonomous ground vehicle," *Control Engineering Practice*, Vol. 17, pp. 741-750, 2009.

[43] S. Mammar and D. Koenig, "Vehicle handling improvement by active steering," *Vehicle System Dynamics*, Vol. 38, No. 3, pp. 211-242, 2002.

[44] S. H. Yu and J. J. Moskwa, "A global approach to vehicle control: Coordination of four wheel steering and wheel torques," *Journal of Dynamic Systems, Measurement, and Control*, Vol. 116, No. 4, pp. 659-667, 1994.

[45] M. Abe, "Vehicle dynamic and control for improving and active safety: from 4WS to DYC," *in Proceedings of IMechE Conference on Multi-body Dynamics: News Techniques and Applications*, pp. 229-248, 1998.

[46] M. Nagai, S. Yamanaka, and Y. Hirano, "Integrated control of active rear wheel steering and yaw moment control using braking forces," *JSME International Journal*, Vol. 42, No. 2, 1999.

[47] B. Zhang, A. Khajepour, and A. Goodarzi, "Vehicle yaw stability control using active rear steering: Development and experimental validation," *Journal of Multi-body Dynamics*, Vol. 231, No. 2, pp. 333-345, 2017.

[48] S. F. Phillips and D. E. Seborg, "Conditions that guarantee no overshoot for linear systems," *International Journal of Control*, Vol. 47, No. 4, pp. 1043-1059, 1988.

[49] K. L. Moore and S. P. Bhattacharyya, "A technique for choosing zero locations for minimal overshoot," *IEEE Transactions on Automatic Control*, Vol. 35, No. 5, pp. 577-580, 1990.

[50] S. K. Lin and C. J. Fang, "Non-overshooting and monotone non-decreasing step responses of a third-order SISO linear system," *IEEE Transactions on Automatic Control*, Vol. 42, No. 9, pp. 1299- 1303, 1997.

[51] M. Bement and S. Jayasuriya, "Construction of a set of non-overshooting tracking controllers," *Journal of Dynamic Systems, Measurement, and Control,* Vol. 126, No. 3, pp. 558-567, 2004.

[52] R. Schmid and L. Ntogramatzidis, "A unified method for the design of non-overshooting linear multivariable state-feedback tracking controllers," *Automatica*, Vol. 46, pp. 312-321, 2010.

[53] M. Krstic and M. Bement, "Non-overshooting control of strict-feedback nonlinear systems," in *Proceedings of the American Control Conference*, 2007.

[54] B. Zhu and C. Zhao, "Non-overshooting output tracking of feedback linearizable nonlinear systems," *International Journal of Control*, Vol. 86, No. 5, pp. 821-832, 2013.

[55] J. A. Gonzalez, A. Barreiro, S. Dormido, and A. Banos, "Nonlinear adaptive sliding mode control with fast non-overshooting responses and chattering avoidance," *Journal of the Franklin Institute*, Vol. 354, pp. 2788-2815, 2017.

[56] K. D. Kim and P. R. Kumar, "An MPC-based approach to provable system-wide safety and liveness of autonomous ground traffic," *IEEE Transactions on Automatic Control*, Vol. 59, No. 12, pp. 3341-3356, 2014.

[57] P. Ogren and N.E. Leonard, "A convergent dynamic window approach to obstacle avoidance," *IEEE Transactions on Robotics*, Vol. 21, No. 2, pp. 188-195, 2005.

[58] F. Blanchini, "Set invariance in control," *Automatica*, Vol. 35, pp. 1747-1767, 1999.

[59] Z. Artstein, "Stabilization with relaxed controls," *Nonlinear Analysis*, Vol. 7, No. 11, pp.1163-1173, 1983.

[60] S. Prajna, "Optimization-based methods for nonlinear and hybrid systems verification," PhD thesis, California Institute of Technology, 2005.

[61] S. Prajna and A. Jadbabaie, "Safety verification of hybrid systems using Barrier certificates," *Hybrid systems: computation and control*, Springer-Verlag, pp. 477-492. 2004.

[62] P. Wieland and F. Allgöwer, "Constructive safety using control barrier functions," in *Proceedings of IFAC Nonlinear Control System*, pp. 473-478, 2007.

[63] A. D. Ames, X. Xu, J. W. Grizzle, and P. Tabuada, "Control barrier function based quadratic programs for safety critical systems," *IEEE Transactions on Automatic Control*, Vol. 62, No. 8, pp.3861-3876, 2017.

[64] K. B. Ngo, R. Mahony, and Z. Jiang, "Integrator backstepping using barrier functions for systems with multiple state constraints," in *Proceedings of IEEE Conference of Decision and Control*, pp. 8306-8312, 2005.

[65] K. P. Tee, S. S. Ge, and E. H. Tay, "Barrier Lyapunov functions for the control of output-constrained nonlinear systems," *Automatica*, Vol. 45, No. 4, pp. 918-927, 2009.

[66] K. P. Tee, B. Ren, and S. S. Ge, "Control of nonlinear systems with time-varying output constraints," *Automatica*, Vol. 47, pp. 2511-2516, 2011.

[67] W. He, C. Sun, and S. S. Ge, "Top tension control of a flexible marine riser by using integral-barrier Lyapunov function," *IEEE Transactions on Mechatronics*, Vol. 20, No. 2, pp. 497-505, 2015.

[68] Y. Liu and S. Tong, "Barrier Lyapunov functions-based adaptive control for a class of nonlinear pure-feedback systems with full state constraints," *Automatica*, Vol. 64. pp. 70-75, 2016.

[69] M. Z. Romdlony and B. Jayawardhana, "Stabilization with guaranteed safety using Control Lyapunov-Barrier Function," *Automatica*, Vol. 66, pp. 39-47, 2016.

[70] G. Fan and K. Sreenath, "Safety-critical and constrained geometric control synthesis using control Lyapunov and control Barrier functions for systems evolving on manifolds," in *Proceedings of American Control Conference*, pp.2038-2044, 2015.

[71] X. Xu, J. W. Grizzle, P. Tabuada, and A. D. Ames, "Correctness guarantees for the composition of lane keeping and adaptive cruise control," *IEEE Transactions on Automation Science and Engineering*, Vol. 15, No. 3, pp.1216-1229, 2018.

[72] Y. Chen, H. Peng, and J. Grizzle, "Obstacle avoidance for low-speed autonomous vehicles with barrier function," *IEEE Transactions on Control Systems Technology*, Vol. 26. No. 1, pp. 194-206, 2018.

[73] L. Wang, A. D. Ames, and M. Egerstedt, "Safety barrier certificates for collision multirobot system," *IEEE Transactions on Robotics*, Vol. 33, No. 3. pp. 661-674, 2017.

[74] X. Xu, "Constrained control of input-output linearizable system using control sharing barrier functions," *Automatica*, Vol. 87, pp. 195-201, 2018.

[75] X. Xu, P. Tabuada, J. W. Grizzle, and A.D. Ames, "Robustness of control barrier functions for safety critical control," in *Proceedings of IFAC Conference of Analysis and Design of Hybrid Systems*, pp. 54-61, 2015.

[76] L. Lindemann and D. V. Dimarogonas, "Control barrier functions for signal temporal logic tasks," *IEEE Control System Letters*, Vol. 3, No. 1, pp. 96-101. 2019.

[77] H. K. Kahlil, Nonlinear systems, Upper Saddle River, NJ: Prentice Hall, 2002.

[78] L. Kocarev, U. Parlitz, and B. Hu, "Lie derivatives and dynamical systems," *Chaos, Solitons & Frantals*, Vol. 9, No. 8, pp. 1359-1366, 1998.

[79] W. Liang, J. Medanic, and R. Ruhl, "Analytical dynamic tire model," *Vehicle System Dynamics*, Vol. 46, No. 3, pp. 197-227, 2008.

[80] H. B. Pacejka, and E. Bakker, "Magic formula tyre model," *Vehicle System Dynamics*, Vol. 21, pp. 1-18, 1993.

[81] J. Y. Wong, Theory of ground vehicles, 4th ed. NY, John Wiley & Sons, 2008.

[82] R. Wang, and J. Wang, "Tire-road friction coefficient and tire cornering stiffness estimation based on longitudinal tire force difference generation," *Control Engineering Practice*, Vol. 21, No. 1, pp. 65-75, 2013.

[83] A. A. Anagnost, and C. A. Desoer, "An elementary proof of the Routh-Hurwitz stability criterion," *Circuits, Systems and Signal Processing*, Vol. 10, No. 1, pp. 101-114, 1991.

[84] H. B. Pacejka, "Simplified Analysis of Steady-State Turning Behaviour of Motor Vehicles Part 2: Stability of the Steady-State Turn," *Vehicle System Dynamics*, Vol.2, No.4, pp. 173-183, 1973.

[85] Y. Huang, W. Liang, and Y. Chen, "Estimation and analysis of vehicle lateral stability region," in *Proceedings of American Control Conference* (Invited Paper), pp. 4303-4308, 2017.

[86] Y. Huang and Y. Chen, "Estimation and analysis of vehicle lateral stability region with both front and rear wheel steering," in *Proceedings of the ASME Dynamic Systems and Control Conference* (Invited Paper), 2017.

[87] Y. Huang and Y. Chen, "Vehicle lateral motion control based on estimated stability regions," in *Proceedings of ASME Dynamic Systems and Control Conference*, (Invited Paper), 2017.

[88] Y. Huang and Y. Chen, "Integrated AFS and ARS control based on estimated vehicle lateral stability regions," in *Proceedings of American Control Conference*, pp. 5516-5521, 2018.

[89] Y. Huang and Y. Chen, "Lateral stability control of autonomous ground vehicles considering stability margins and state estimation errors," in *Proceedings of American Control Conference* (Invited Paper), pp. 3245-3250, 2018.

[90] Y. Huang and Y. Chen, "Stability region based vehicle lateral control using non-overshooting MPC," in *Proceedings of American Control Conference*, pp. 5526-5530, 2019.

[91] Y. Huang, S. Z. Yong, and Y. Chen, "Guaranteed vehicle safety control using control-dependent barrier functions," in *Proceedings of American Control Conference* (Invited Paper), pp. 983-988, 2019.

[92] Y. Huang, T. Chidambareswaran, C. Chang, and Y. Chen, "Two segments (plus) path planning of automatic parking assist system for 4WS vehicles," *ASME Dynamic Systems and Control Conference*, (Invited Paper), DSCC2019-9005, Oct. 2019.

[93] Yiwen Huang and Yan Chen, "Switched control barrier functions with applications to vehicle safety control," in *Proceedings of 2020 ASME Dynamic Systems and Control Conference*, DSCC2020-3293 (Invited Paper), 2020.

[94] Y. Huang, W. Liang, and Y. Chen, "Stability Regions of Vehicle Lateral Dynamics: Estimation and Analysis," *ASME Journal of Dynamic System, Measurement, and control*, Vol. 143, No.5, DS-20-1048, 2021.

[95] Y. Huang, F. Wang, A. Li, Y. Shi, and Y. Chen, "Development and Experimental Evaluations of An Over-Actuated Autonomous Ground Vehicle," *IEEE/ASME Transactions on Mechatronics*, Vol. 26, Iss. 1, pp. 33-44, 2021.

[96] Y. Huang and Y. Chen, "Vehicle lateral stability control based on shiftable stability regions and dynamic margins," *IEEE Transactions on Vehicular Technology*, Vol. 69, No. 12, pp. 14727-14738, 2020.

[97] Y. Shi, Y. Huang, and Y. Chen, "Trajectory Planning of Autonomous Trucks for Collision Avoidance with Rollover Prevention," *IEEE Transactions on Intelligent Transportation Systems*, under review, 2019.

[98] Y. Huang, S. Z. Yong, and Y. Chen, "Safety Control of Autonomous Ground Vehicles Using Control-Dependent Barrier Functions," *IEEE Transactions on Intelligent Vehicles*, in press, 2021.

[99] H. Ohara and T. Murakami, "A stability control by active angle control of front-wheel in a vehicle system," *IEEE Transactions on Industrial Electronics*, Vol. 55, No. 3, pp. 1277-1285, 2008.

[100] M. K. Aripin, Y. M. Sam, K. A. Danapalasingam, K. Peng, N. Hamzah, and M. F. Ismail, "A review of active yaw control system for vehicle handling and stability enhancement," *International Journal of Vehicular Technology*, Vol. 2014, pp. 1-15, 2014.

[101] M. Jalali, E. Hashemi, A. Khajepour, S. Chen, and B. Litkouhi, "A combine-slip predictive control of vehicle stability with experimental verification," *Vehicle System Dynamics*, Vol. 56, No. 2, pp. 319-340, 2018.

[102] J. H. Park and C. Y. Kim, "Wheel Slip Control in Traction Control System for Vehicle Stability," *Vehicle System Dynamics*, Vol. 31, No. 4, pp. 263-278, 1999.

[103] S. A. Ferguson, "The Effectiveness of Electronic Stability Control in Reducing Real-World Crashes: A Literature Review," *Traffic Injury Prevention*, Vol. 8, No. 4, pp. 329-338, 2007.

[104] J. Funke, M. Brown, S. M. Erlien, and J. C. Gerdes, "Collision avoidance and stabilization for autonomous vehicles in emergency scenarios," *IEEE Transactions of Control System Technology*, Vol. 25, No. 4, pp. 1204-1216, 2017.

[105] V. Utkin, J. Guldner, and J. Shi, *Sliding Mode Control in Electro-Mechanical Systems*, 2nd ed. Cleveland, OH, USA: CRC Press, 2009.

[106] A. Damiano, G. L. Gatto, I. Marongiu, and A. Pisano, "Second-order sliding-mode control of DC drives," *IEEE Transactions on Industrial Electronics*, Vol. 51, No. 2, pp. 364-373, 2004.

[107] A. Rezaeian, A. Khajepour, W. Melek, S. K. Chen and N. Moshchuk, "Simultaneous Vehicle Real-Time Longitudinal and Lateral Velocity Estimation," *IEEE Transactions on Vehicular Technology*, Vol. 66, No. 3, pp. 1950-1962, 2017.

[108] Z. Gao, J. Wang, and D. Wang, "Dynamic Modeling and Steering Performance Analysis of Active Front Steering System," *Procedia Engineering*, Vol. 15, pp. 1030-1035, 2011.

[109] L. D. Novellis, A. Sorniotti, P. Gruber, J. Orus, J. R. Fortun, J. Theunissen, and J. D. Smet, "Direct yaw moment control actuated through electric drivetrains and friction brakes: Theoretical design and experimental assessment," *Mechatronics*, Vol. 26, pp. 1-15, 2015.

[110] F. Franklin, J. D. Powell, and A. E. Naeini, *Feedback Control of Dynamic Systems*. 7th ed. Prentice Hall, 2014.

[111] R. P. Agarwal, R. P. Agarwal, and V. Lakshmikantham. Uniqueness and nonuniqueness criteria for ordinary differential equations. Vol. 6, World Scientific, 1993.

[112] C. Funfschilling and G. Perrin, "Uncertainty quantification in vehicle dynamics," *Vehicle System Dynamics,* Vol. 57, No. 7, pp. 1062-1086, 2019.

[113] Y. Furukawa, N. Yuhara, S. Sano, H. Takeda, and Y. Matsushita, "A review of four-wheel steering studies from the viewpoint of vehicle dynamics and control," *Vehicle System Dynamics*, Vol. 18, pp. 151-186, 1989.

[114] A. Rezaeian, A. Khajepour, W. Melek, S.-Ken Chen, and N. Moshchuk, "Simultaneous vehicle real-time longitudinal and lateral velocity estimation," *IEEE Transactions on Vehicular Technology*, Vol. 66, No. 3, 2017.

[115] X. Wang, Vehicle Noise and Vibration Refinement, Woodhead Publishing Limited, Abington Hall, Cambridge, UK, 2010.

[116] N. Athanasopoulos and R. M. Jungers, "Combinatorial methods for invariance and safety of hybrid systems," *Automatica*, Vol. 98, pp. 130-140, 2018.

[117] N. Athanasopoulos, K. Smpoukis, and R. M. Jungers, "Invariant sets analysis for constrained switching systems," *IEEE Control Systems Letters*, Vol. 1, No. 2, pp. 256-261, 2017.

[118] C. Danielson, L. J. Bridgeman, and S. Di Cairano, "Necessary and sufficient conditions for constraint satisfaction in switched systems using switch-robust control invariant sets," *International Journal of Robust and Nonlinear Control*, Vol. 29, pp. 2589-2602, 2019.

[119] L. Lindemann and D. V. Dimarogonas, "Control barrier functions for signal temporal logic tasks," *IEEE Control Systems Letters*, Vol. 3, No. 1, pp. 96-101, 2019.

[120] L. Lindemann, C. K. Verginis, and D. V. Dimarogonas, "Prescribed performance control for signal temporal logic specifications," in *IEEE 56th Conference on Decision and Control*, pp. 2997-3002, 2017.

[121] L. Wang, A. D. Ames, and M. Egerstedt, "Multi-objective compositions for collision-free connectivity maintenance in teams of mobile robots," in *Proceedings of IEEE 55th Conference on Decision and Control*, pp. 2659-2664, 2016.

[122] P. Glotfelter, J. Corts, and M. Egerstedt, "Nonsmooth barrier functions with applications to multi-robot systems," *IEEE Control Systems Letters*, Vol. 1, No. 2, pp. 310-315, 2017.

[123] F. Clarke, Optimization and Nonsmooth Analysis. Philadelphia, PA, USA: Soc. for Ind. and Appl. Math., 1990.

[124] P. Glotfelter, J. Corts, and M. Egerstedt, "Boolean composability of constraints and control synthesis for multi-robot systems via nonsmooth control barrier functions," in *Proceedings of IEEE Conference on Control Technology and Applications*, pp. 897-902, 2018.

[125] P. Glotfelter, I. Buckley, and M. Egerstedt, "Hybrid nonsmooth barrier functions with applications to provably safe and composable collision avoidance for robotic systems," *IEEE Robotics and Automation Letters*, Vol. 4, No. 2, pp. 1303-1310, 2019.

[126] J. P. Aubin, H. Frankowska, Set-valued analysis, Birkhauser, Boston, 1990.

APPENDIX A

STATEMENT OF COPYRIGHT PERMISSIONS

This statement is written to declare that all the reprinted contents (e.g., figure, graph, table, or textual material) in this dissertation have obtained the full granted copyright permissions from the first author, Yiwen Huang, the corresponding author, Yan Chen, and all other co-authors. In reference to IEEE and ASME copyrighted material, which is used with permission in this thesis dissertation, the IEEE and ASME do not endorse any of Arizona State University's products or services. Internal or personal use of this material is permitted.